Radiation Environment Simulations at the Tevatron, Studies of the Beam Profile, and Measurement of the B_c Meson Mass

Ludovic Yannick Nicolas

UNIVERSITY
of
GLASGOW

Department of Physics and Astronomy

September 2005

A thesis submitted to the Physical Science Graduate School

for the degree of Doctor of Philosophy.

Declaration

No portion of the author's work described in this thesis has been submitted in support of an application for another degree or qualification in this, or any other, institute of learning.

Abstract

The description of a computer simulation of the CDF detector at Fermilab and the adjacent accelerator parts is detailed, with MARS calculations of the radiation background in various elements of the model due to the collision of beams and machine-related losses. Three components of beam halo formation are simulated for the determination of the principal source of radiation background in CDF due to beam losses. The effect of a collimator as a protection for the detector is studied. The simulation results are compared with data taken by a CDF group.

Studies of a 150 GeV Tevatron proton beam are performed to investigate the transverse diffusion growth and distribution. A technique of collimator scan is used to scrape the beam under various experimental conditions, and computer programs are written for the beam reconstruction. An average beam halo growth speed is given and the potential of beam tail reconstruction using the collimator scan is evaluated.

A particle physics analysis is conducted in order to detect the $B_c \to J/\psi\pi$ decay signal with the CDF Run II detector in 360 pb^{-1} of data. The cut variables and an optimisation method to determine their values are presented along with a criterion for the detection threshold of the signal. The mass of the B_c meson is measured with an evaluation of the significance of the signal.

Acknowledgments

I would like to thank my two supervisors Peter Bussey (University of Glasgow) and Nikolai Mokhov (Fermilab), who made the realisation of this project possible and provided great help.

I am very grateful to Saverio D'Auria. He was essential to the work on B_c.

I would also like to particularly thank the following persons for their important contribution at various levels:

Mike Albrow, Nick Barov, Catherine Biscarat, Alexi Burov, Jean-Paul Carneiro, François Clapier, Alexandr Drozhdin, Arnaud Duperrin, Lorenzo Feligioni, Andreas Jansson, Mikhail Kostin, Valeri Lebedev, Caroline Milstene, Ron Moore, Sergei Nagaitsev, Armelle & Yannick Nicolas, Philippe Piot, Stephen Pordes, Giovanni Punzi, Igor Rakhno, Roy Rubinstein, Paul Russo, David H. Saxon, Vladimir Shiltsev, Michel Sorel, Mario Spezziga, Dean Still, Sergei Striganov, Michael Syphers, Richard Tesarek, Alvin Tollestrup, Igor Tropin, and Antoine Valance.

This work has been funded by Fermilab. The first six months were funded by the University of Glasgow.

Contents

Chapter 1

Introduction

Several topics are being discussed in this dissertation, covering different aspects of a High Energy Physics (HEP) environment. The research presented here was conducted at the Fermi National Accelerator Laboratory (Fermilab) near Chicago, USA. At the time of the writing, the laboratory is the home of a chain of accelerating elements that ultimately injects two beams - one of protons p, the other of anti-protons $\bar{p}$ - into the Tevatron, a circular superconducting collider (see Fig. 1.1). Some characteristics of the Tevatron are given in Table 1.1. The two beams circulating in the same pipe collide head-on at the location of two detector experiments - CDF and DØ - where the resulting interaction products are analysed. The interface of the accelerator with the CDF detector (cf. chapter 4 for a presentation of the detector) provides the context of part of the work presented here, with the computer simulation of beam interactions with matter and the effect on the detector. A further important area comprises the characteristics of the beam itself, since the understanding of the beam behaviour in the Tevatron is of great importance at the experiment level. The collisions in the detectors should take place with minimal background, partly due to the collisions themselves, but also due to that induced in the machine components and coming to the detector from the Tevatron tunnel.

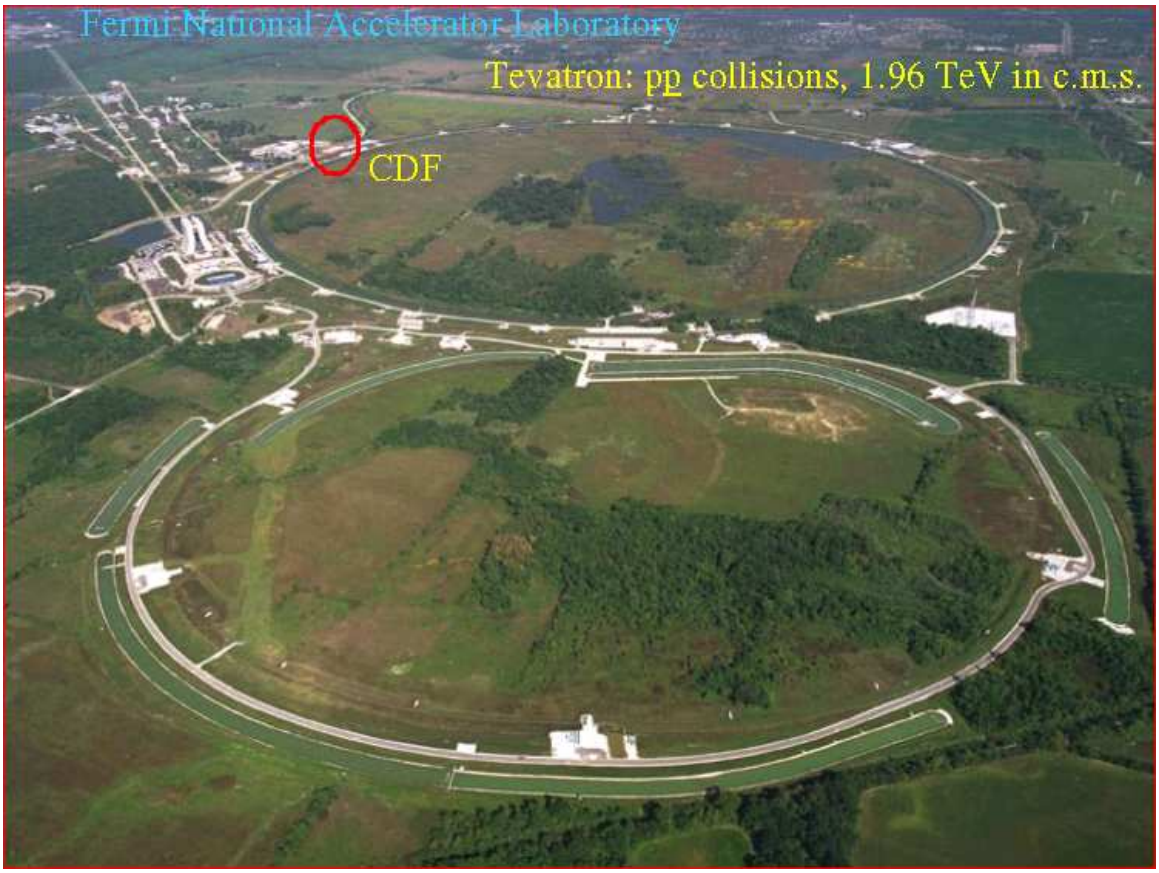

Figure 1.1: Aerial view of Fermilab. The ring at the bottom of the picture is the Main Injector which feeds the Tevatron (ring on the top) with beams for collisions at DØ and CDF (circled). The two rings are indicated by roads since the accelerators are buried underground. Also, the perspective is confusing, the Tevatron is in fact about twice as large as the Main Injector.

One particular problem of importance is the formation of the beam halo, i.e. the development of a neighbouring beam population around the beam core caused by various effects, that can be a source of background.

The final product of an accelerator is the particle physics studied in the detector experiments. The collision of protons with anti-protons at an energy of 980×980 GeV results in multiparticle events that can easily represent an overwhelming amount of

Injection energy	150 GeV
Flattop energy	980 GeV
Number of bunches	36 p, 36 $\bar{p}$
Particles per bunch	220-260$\times 10^9$ p, 30-50$\times 10^9$ $\bar{p}$
Shot setup (Fill time)	2 hours
Store lengths	$\sim$30 hours
Revolution frequency	47.77 kHz
Fill structure	3 trains of 12 bunches, 396 ns of bunch spacing
Abort gap length	2.617 μs
Bunch size @ IP	σ_z $\sim$50 cm
Luminosity	$\sim 80\times 10^{30}$ cm^{-2}.s^{-1}
Collected data for Run II	1.4 fb^{-1}

Table 1.1: Some properties of the Tevatron collider beams.

information. One aspect of experimental particle physics is to identify among all this information a specific signature for particles of interest. Via the output from the various components of the detector surrounding the interaction point (IP), one may seek to reconstruct the formation of a system created during the $\bar{p}p$ collision and its subsequent decay. Eventually, if this task is successful (which is most easily achieved if the background in the detector is well understood and kept minimal), it is then possible to learn some characteristics of this particle such as its ability to decay in a certain channel, its lifetime or its mass.

This dissertation concerns itself with all these different aspects, from the transverse growth of the proton beam at 150 GeV due to residual gas present in the Tevatron beam pipe, to an attempt to determine the mass of the B_c meson by searching for the decay $B_c \longrightarrow J\psi\pi$ in the data acquired by the CDF detector.

The first topic developed in the dissertation presents radiation physics studies at the machine/detector interface. Such studies are necessary in accelerator facilities because of the energies involved and the secondary particles produced. At 980 GeV, the radiation field in the Tevatron due to beam encounters with matter, which could be a limiting aperture or the residual gas, can potentially be a nuisance for the machine elements, for instance the cold magnets and their quench stability, and a careful investigation of the impact of radiation on the machine elements and/or the detector components is needed. Bearing in mind both the dimensions of the equipment and the costs involved in operating accelerator facilities (the Tevatron has a circumference of 6283 m), investigations imply the use of computer codes to simulate the production of particles and their subsequent effects. Among the programs designed to simulate the passage of particles through matter, MARS [1] by N. Mokhov has been successfully used to study energy deposition and radiation environments in various laboratories worldwide [2]. The MARS program, according to its official website, is "a Monte Carlo code for inclusive and exclusive simulation of three-dimensional hadronic and electromagnetic cascades, muon, heavy-ion and low-energy neutron transport in accelerator, detector, spacecraft and shielding components in the energy range from a fraction of an electron-volt up to 100 TeV". Realistic modeling of detector and accelerator geometries can be included in MARS with the specification of a radiation source. The code handles the propagation of the particles with all the daughter products created, and returns values of energy deposition, particle spectra and fluxes, induced radioactivity, at desired locations. While the production of secondaries is treated with MARS, another computer code, STRUCT [3], performs particle tracking and interactions with material of collimators in synchrotrons and beam lines allowing the simulation of beam loss distributions along the accelerator. The use of these two codes is presented in Chapter 2 with various investigations of radiation loads in the Tevatron environment, from the modest size Roman Pots detectors to radiation maps in the CDF tracking volume. The contributions of three distinct beam halo

channels are evaluated, and compared with experimental radiation measurements for the general understanding of the main background source and the radiation field in a collider detector. This ultimately contributes to the design of a Tevatron collimator in order to reduce beam-related backgrounds at CDF.

Chapter 3 describes some of the causes of the machine-related backgrounds, with the experimental study of the beam halo formation in Tevatron. A collimation technique is used to reconstruct the transverse spatial profile of the beam which, under specific experimental conditions, can allow the determination of the beam transverse growth and tail distribution.

Chapter 4 presents a search for the decay $B_c \longrightarrow J/\psi\pi$. The CDF detector is described, and the strategy used for the analysis is discussed, with the investigations of the best selection cuts to identify a signal. Since all the decay products of this channel can be detected, the reconstruction of the decay allows a precise mass measurement of the B_c meson for the first time.

Chapter 2

Radiation Background Modeling

2.1 The CDF MARS Model

The study of the radiation background in the CDF detector requires the accurate modeling of all the relevant beamline elements for the particle tracking and for the production of secondaries. An adjacent part of the accelerator must be specified, with a detailed description of the CDF detector. This constitutes the CDF MARS Model. The MARS manual [4] explains how to build a generic study system. The following section presents an elaboration of the CDF/Tevatron interface.

2.1.1 Simulation Set-Up

As for all the MARS applications, a number of files are needed to use the code. MARS.INP, GEOM.INP, XYZHIS.INP are sets of input cards where the user specifies, respectively, the general control of the simulation, the geometry description in the *Extended* mode option, and the location of the output histograms. The FORTRAN files marsmain.f and m1505.f are also required, the latter being the one where complex user definitions such as magnetic field are included. The remaining objects

required are the GNUmakefile for building the executable and xsdir to provide cross sections when one uses the MCNP [5] option. For the CDF MARS model, the control input card MARS.INP is as follows:

```
CDF B0
/home/mokhov/restricted/mars15/dat
INDX 1=F 3=T 4=T 13=T
CTRL 2
C TAPE 18
NEVT 1
ENRG 999.06217
IPIB 1
SMIN 0.001 3.
ZMIN -15500.
NLNG 2
ZSEC 0. 3000.
NLTR 1
RSEC 1500.
   101=5
NMAT 44
MATR 'STST' 'FE'   'CU'   'W'    'AIR'
     'CH'   'SCON' 'MYAL' 'YOKE' 'BE'
     'SOIL' 'AIR'  'CONC' 'MIX1' 'MIX4'
     'MIX2' 'MIX3' 'PB'   'AL' 'AR'
     'SI'   'STST' 'AIR'  'CH'   'N'
     'SI'   'N'    'STST' 'CH'   'C'
     'AL'   'MIX9' 'CU'   'FE'   'CH4'
     'PB'   'MIX5' 'MIX6' 'MIX7' 'G10'
     'MIX8' 'MIXA' 'CH'   'AIR'
```

```
MTSM 10=0.005 22=0.005 0.005 0.005 26=0.002 0.002 0.005 30=0.01 0.01 40=0.01
MTSH 10=0.05 22=0.5 0.5 0.5 26=0.02 0.02 0.4 30=0.2 0.3 40=0.1
MTDN 14=0.035 5.0 0.2 5.44 32=0.9525 37=3.80 5.196 0.0024 41=8.745 0.01
MTNE 11=0.05
NOBL 1
RZOB 0. 200. -200. 200.
SEED 25134512
STOP
```

The "INDX" line lists general options for the simulation and their status, whether they will be true (T) or false (F). For instance, 13=T indicates that the MARS 13^{st} option - enabling the MMBLB package [6] (cf. page 12) - is true. Consequently, the routines allowing to describe curved accelerator elements are read.

The "CTRL" line controls if the MARS code runs on Monte Carlo mode (option 0), or on visualisation mode (option 1 or 2).

"C TAPE 18" is a commented line ("C" starts the line), that controls the registration of tracks for visualization. Uncommenting it will write an output file "TRACK.PLOT" with all the necessary informations to display tracks on visualization mode.

"NEVT" is where the number of particles for the simulation run is specified by the user.

"ENRG" is the energy in GeV of the initially launched particle.

"IPIB" allows the user to code the launched particle, following a MARS nomenclature. Here, 1 stands for proton.

"SMIN" is a global step (cm) for the particle during its transport. As specified here, the proton travels steps of 3 cm in the model, and if a change of zone is detected, goes back and forth around the zone separation limit with decreasing step size down to 0.001 cm.

"ZMIN" is the (negative) $z-$coordinate (cm) of the MARS description for the problem. The present model extends 155 meters before the interaction point of CDF.

"NLNG" declares how many global longitudinal parts will divide the model. Here 2 parts are distinguished : -155 m before the IP (0), and 30 m after the IP.
"ZSEC" specifies the boundary of the second part as declared in "NLNG". Here 30 m.
"NLTR" allows the user to declare the number of radial parts. Here only one is used.
"RSEC" defines how far outwards this radial part extends. It implicitly starts at R=0 cm, and goes up to 15 m. In addition, "101=5" tells the code that this defined radial space will be filled with material number 5, in the list specified in "MATR".
"NMAT" declares how many materials are used. For the CDF MARS model, 44 different materials are present. It can be the same ("STST" is listed twice), but with different transport properties.
"MATR" lists the 44 material used. Some of these identifiers call pre-built materials e.g. "CONC", which has been coded in MARS as a type of concrete; some call elements e.g. "FE" for iron, and some call user defined materials e.g. "MIX5" where the chemical properties are described in a user subroutine MIXTUR in the m1505.f file.
"MTSM" overwrites transport conditions for the minimum boundary step entered in "SMIN" for the material listed. e.g. "10=0.005" means that for "BE" (number 10 in the "MATR" list), the minimum step for particles in this material will be 0.005 cm instead of 0.001 as indicated in "SMIN".
"MTSH" overwrites the global step (cm) for the materials listed.
"MTDN" allows the user to define the densities for the materials.
"NOBL" enables the $R-Z$ histogram function.
"RZOB" defines the boundary limits for the $R-Z$ histogram scoring.
"SEED" is a random number identifier. By using different seed identifiers, the same "MARS.INP" input card can be used, with the same number of events but simulating a different physics case.

The interaction region of the CDF detector is coded with the *Extended* geometry description method via the input file GEOM.INP. This provides the user with an

immediate description of objects specifying their dimension and orientation without compilation of the code. It is a powerful tool essential for the modeling of the numerous detectors inside the tracking volume as well as external parts such as the CMX muon detectors.

The input card for the histogram scoring XYZHIS.INP uses the same immediate approach where the user specifies the location and size of the space where the histogram will be placed. One can choose the particular type of particles to be recorded, e.g. the collection of neutron flux, and particle energy spectra can also be obtained in a very convenient way. The output results are such that they can be analysed with PAW.

Among the subroutines available to the user in the FORTRAN file m1504.f, REG1 was extensively used for the creation of the geometry. It is based on a logical scan of the (x, y, z) space and allows the user to assign a region number with a specific material. The accelerator parts of the CDF MARS model were created with this routine. For the model, REG1 was specifically configured so that it can include the description of the central detector with the *Extended* geometry option, the accelerator elements with MMBLB, and the CDF hall description.

2.1.2 Model Geometry

The investigation of machine-related background requires the entire description of the Tevatron lattice for multi-turn beam halo tracking, a task performed by the STRUCT code. This does not require the complete description within MARS of the accelerator structure, and it is in fact highly desirable to restrict this as much as possible, because full treatments of all the particles created during electromagnetic showers and hadronic cascades are long processes, especially if the energy studied is low, for example down to thermal neutrons with the link to the MCNP code. For these reasons the CDF MARS model is limited to about ± 150 meters of Tevatron around the CDF detector. The following elements are coded in the model geometry:

Tevatron Magnets

Thirty of the 6-m long superconductive dipoles are coded, each with a bending angle of about 8 mrad. The magnetic field (the field lines shown in Fig. 2.1 (left)) is described in the FIELD subroutine corresponding to the dipole object in the element list of the Tevatron lattice. The dipole field is designed to bend the trajectory of the protons and the anti-protons simultaneously, although only the proton contributions are simulated here since their intensity is about 10 times larger than for the anti-proton beam. Also superconducting quadrupoles are present to focus or defocus the circulating beams by means of the magnetic field whose map is shown in Fig. 2.1 (right). The varying fields are coded according to the MAD lattice file [7] that describes the Tevatron elements, and have been verified with tracking tests.

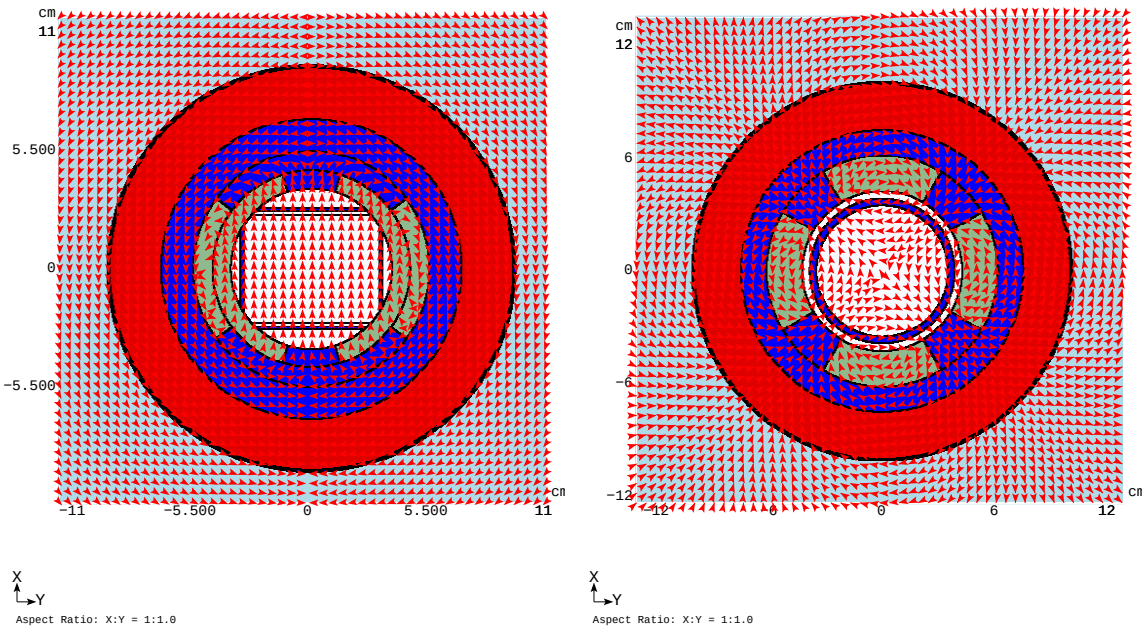

Figure 2.1: Cross section of a dipole (left) and a quadrupole (right) as represented in MARS. The magnetic field lines are indicated by the arrows.

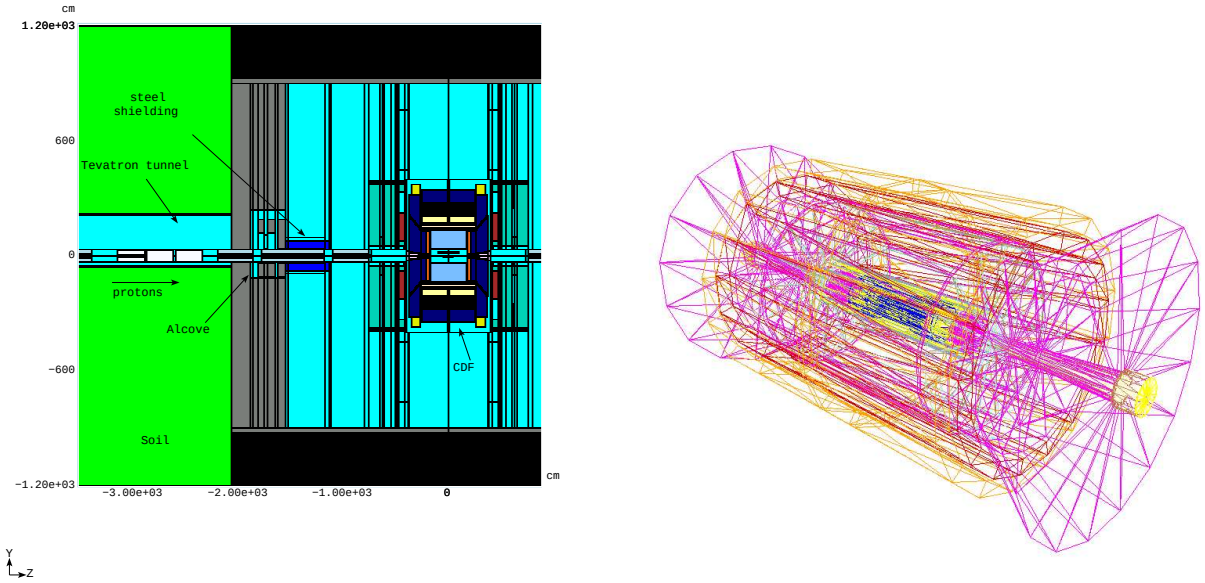

Figure 2.2: Restricted planar view of the CDF MARS model (left) and simplified tracking volume (right).

The CDF MARS Model includes the experimental hall with various detectors, walls, shielding parts and the CDF tracking volume (cf. Fig 2.2). The geometry simulated features the west alcove at the entrance of the CDF hall (incoming proton side) with blocks of concrete and steel shielding around the low beta quadrupoles.
Fig. 2.3 (left) shows the R-Z MARS view of the tracking volume (where a magnetic field of 1.41 T is present) on which flux isocontours will be displayed. Fig. 2.3 (right) shows the details of the silicon detectors not visible in Fig. 2.3 (left).

2.1.3 Tracking Tests and Simulation of Beam Nuclear Inelastic Interactions with Residual Gas

Tracking tests serve as necessary verification of the validity of a model prior to realistic calculations. A perfect beam tracking where radiation should not be produced

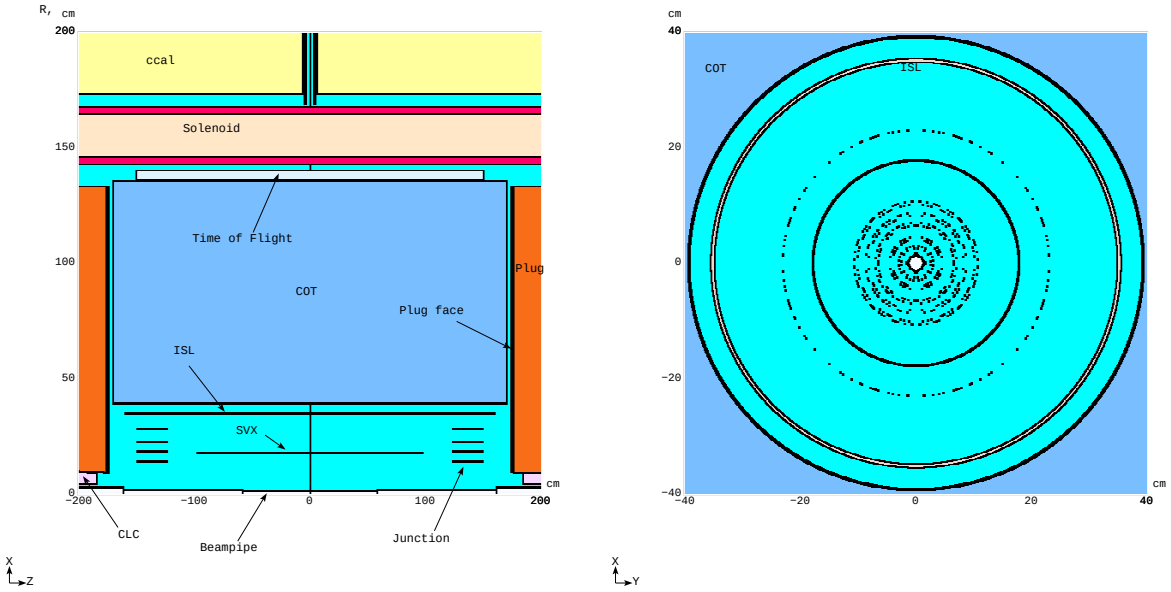

Figure 2.3: Partial elevation views of the inside detector, longitudinally (left), and transversally (right). The scales are different.

is transported in the model to insure that no coding errors lead to an increase of radiation loads due to fake contributions. A proton beam is launched on the axis of the beam pipe at the origin of the model, 150 m before the IP, and going through the lattice with all the accelerator elements. The proton should follow an undisturbed trajectory without being lost, if all the objects' properties (geometry and field) are coded correctly.

The MAD MARS Beam Line Builder (MMBLB) package [6] has been recently implemented in MARS to code the geometry of circular accelerator lattices, with the possibility of describing bending elements. It is a very powerful new feature and its integration within the existing MARS framework requires stability checks for specific cases. The simulation of radiation background due to beam-nuclear inelastic interactions with residual gas in the beam pipe is entirely processed with MARS and does not involve STRUCT calculations. An estimation of the radiation background contribution due to this beam loss channel can be done by launching protons at a random location in the beam pipe along the lattice and to enforce the nuclear interaction to occur, via

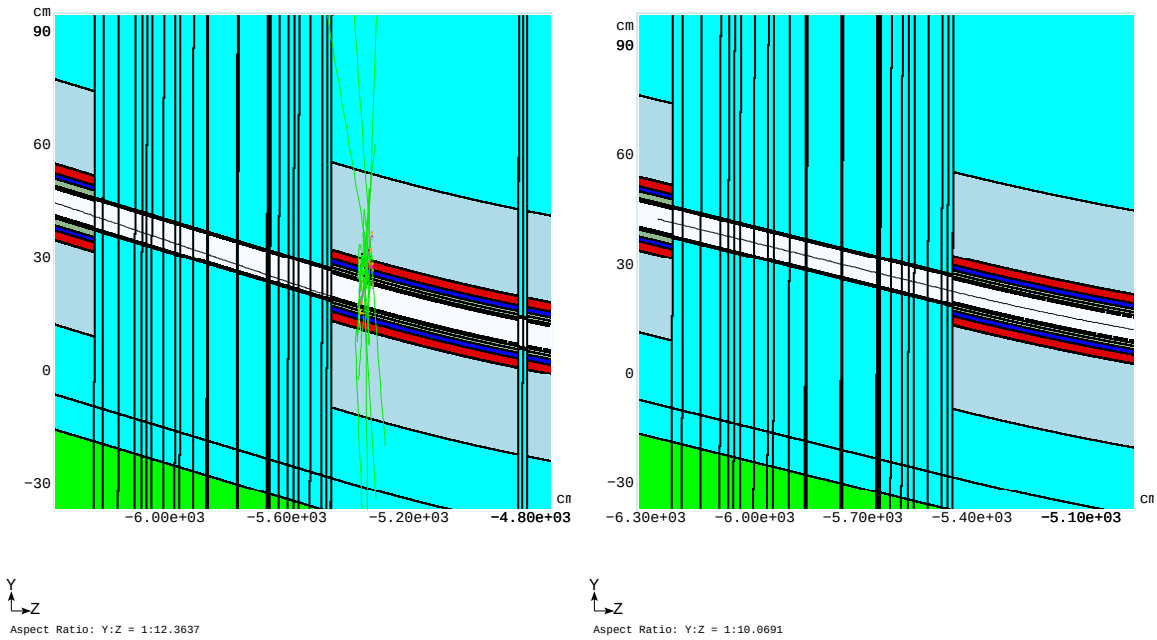

Figure 2.4: Proton track generated in a dipole magnet. The initial conditions are wrongly evaluated with the standard version, and the particle trajectory hits a magnet downstream producing secondaries (left). A correction package is applied and gives the particle the adequate initial conditions wherever the launch is randomly started, consequently no losses occur on tracking tests (right).

the following setting in the MARS.INP card:

```
INDX 7=T
VARS 1.
```

The nature of the target nucleus is specified in the BEG1 subroutine of the m1505.f file for the radiation source definition. A statistical weight for this background contribution is also defined inside BEG1 to relate the number of interactions to the pressure of the target gas material. For this particular application, in the input card MARS.INP, "INDX 7" set to true enables the "VARS 1." simulation mode which corresponds to a point-like forced interaction. Tracking tests without forced nuclear inelastic interactions revealed that "perfect" particle trajectories were computed incorrectly and were inducing non-physical backgrounds (cf. Fig. 2.4(left)). This is due to the fact

that to determine the initial conditions (position and direction) of a particle track, MMBLB calculates the corresponding values via a change of the frame from a global MARS frame to a local MAD frame along the accelerator lattice, and the angles are based on the number of dipoles (bend magnets) involved. The process is however not continuous, in the sense that in a drift section past a dipole (i.e. a straight part), the code keeps in memory the angle resulting from the last dipole. Launching particles from a drift section with the standard MARS version thus does not show any abnormal behavior. If the generation of the particle happens however inside a bending magnet, the additional angle fraction inside this magnet is not recognised. Initial values are computed inaccurately, and the particle is assigned an incorrect kick which results in its loss, producing fake radiation background contributions. A correction package to determine correctly the initial conditions and allow reliable random generation of particle tracks has been created and implemented for the calculation of nuclear inelastic interaction of beam with residual gas (Fig.2.4 (right)).

2.2 Simulations of Beam Losses and New Collimator Impact on the CDF and DØ Sub-detectors

The radiation problems reported by CDF were of two kinds. It happened that electronic devices were damaged by Tevatron beam losses [8] that can have a noticeable effect on the the CDF and DØ detector performance [9]. Providing a new shadow collimator (mask) at the A48 section of the Tevatron was considered as a possible protection for the CDF detector, with a two-fold function for its design: protection of the CDF silicon detectors in the event of an abort kicker prefire (AKP), and reduction of the machine-related background at CDF. Its physical location is roughly 60 m from the interaction point (IP) on the proton side, in the vicinity of the Roman Pots detectors. Crucial aspects for its installation are the impact of this mask on the pots detector lifetime and background, and quench stability of the downstream superconducting magnets.

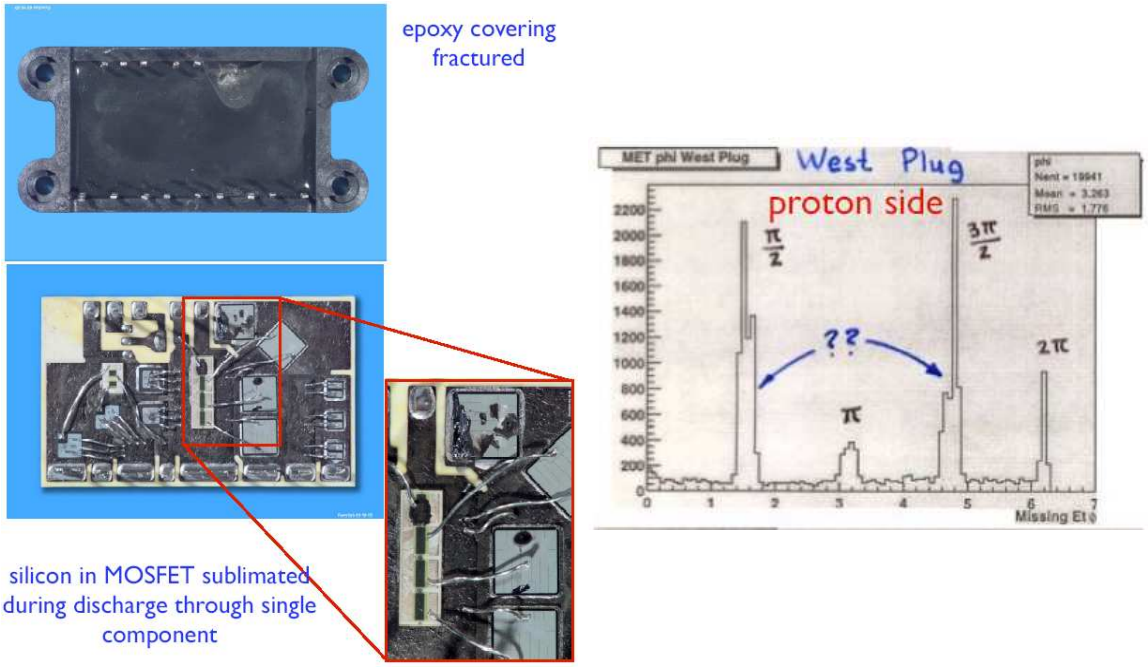

Figure 2.5: Single event burnout damage in electronics (left), and background in a missing E_T reading (right).

2.2.1 Components of Beam Loss in the Tevatron

Proton losses in the Tevatron accelerator may be due to various causes. Three components are thought to be the main contributions and are simulated to evaluate the radiation background:

- *Tails from collimators*, *i.e.* beam loss in the 300-m region resulting from beam halo out-scattered from the components of the *existing* collimation system [10] (Fig.2.6 (left)). At an average luminosity of 10^{32} $cm^{-2}s^{-1}$, the proton beam gives a rate of 3×10^{7} p/s interacting with the primary collimators. Phase space coordinates and the number of protons lost through this process are calculated by A. Drozhdin with the STRUCT code.

- *Beam-gas elastic scattering*, *i.e.* elastic nuclear scattering of a circulating beam on residual gas that leads to protons escaping the beam core, forming the beam halo and ultimately beam loss on the limiting apertures. This component of the source term in the same 300-m region is also calculated by A. Drozhdin with STRUCT. In these multi-turn calculations, the average residual gas pressure in the ring is a key parameter for this channel and the interactions are evaluated for two cases of average pressure (nitrogen equivalent), namely 10^{-9} Torr and 10^{-10} Torr, and a case using a distributed pressure along the accelerator.

- *Beam-gas inelastic interactions* are modeled directly in the course on the MARS runs as mentioned previously. Contrary to the first two processes, particle production angles are relatively large here resulting in short-range tracking (tens of meters). The gas pressure in the vicinity of CDF and DØ is assumed to be 7×10^{-9} Torr, leading to an interaction rate of 4334 $m^{-1}s^{-1}$.

Fig. 2.6 (right) [9] shows a comparison of the cross section evolution calculated by S. Striganov, for different beam-gas interactions. The nuclear coherent (elastic) component dominates over the Coulomb and the inelastic interaction for critical angles of

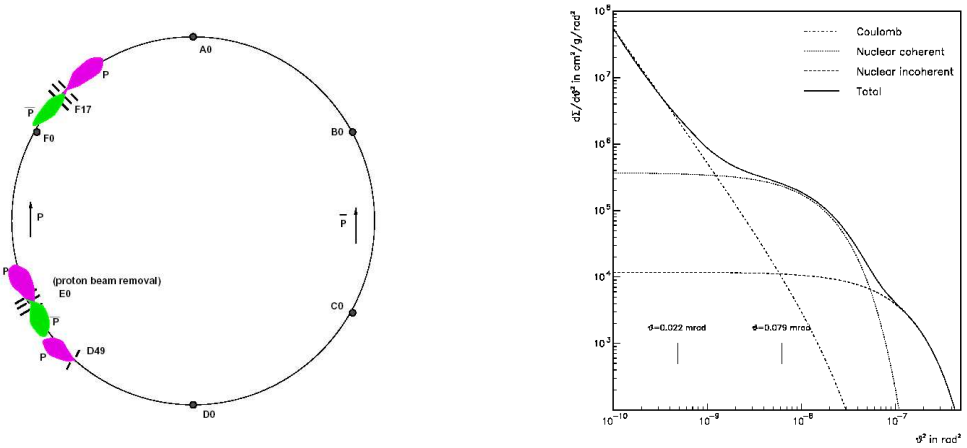

Figure 2.6: Scheme of the Tevatron Run II collimation system (left) and angular cross section of 1 TeV proton for various interaction channels.

deviation that lead to proton losses. For the nuclear elastic channel, with a distributed gas pressure in the accelerator, a total intensity of 10^{13} protons in the machine gives a loss rate of 2.48×10^6 protons/sec in the Tevatron. Fig. 2.7 shows in that case the loss repartition of the STRUCT particles due to nuclear elastic scattering at the entrance of CDF on the proton side. Each STRUCT particle that serves as a source term for the MARS runs corresponds to approximately 9.56 real protons.

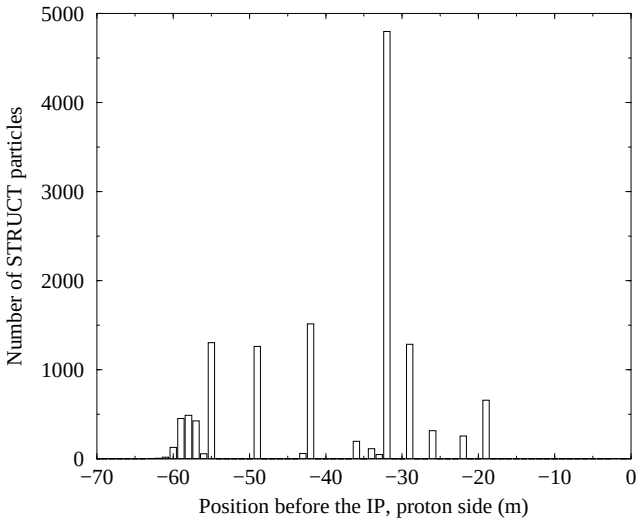

Figure 2.7: Proton loss repartition due to beam-gas nuclear elastic interactions with a distributed pressure model.

2.2.2 A Dangerous Source of Background : Abort Kicker Prefire

In between certain of the circulating bunches in the Tevatron, an abort gap is maintained where the beam is absent to allow the necessary time for beam removal with kicker magnets. However, the accidental trigger of the proton kicker can occasionally occur and thereby deflect bunches with incorrect trajectories into downstream limiting apertures (e.g. separator, dipole). This can result in a magnet quench and up to 200 rad instantaneous doses in CDF. Fig. 2.8 (left) shows an example of STRUCT tracking for an Abort Kicker Prefire (AKP) [11] by A. Drozhdin, where two tracks are accidentally intercepted in the separators upstream of the IP, instead of taking the normal path shown by bunch 7. In such an event, a bunch of protons of more that 2×10^{11} particles (Fig. 2.8 (right)) can hit a limiting aperture close to the main detector and the resulting production of secondaries is a serious concern for near-beam silicon detectors in the tracking volume of CDF.

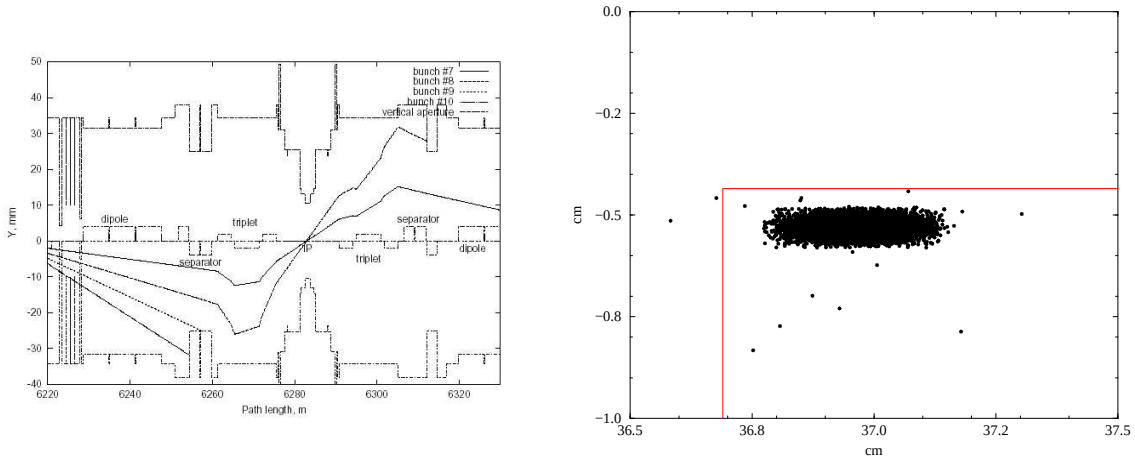

Figure 2.8: Particle tracking during a AKP (left), and spatial transverse distribution of a proton bunch in a AKP event hitting a limiting aperture (right). The solid line here represents the cross section of the "minibar" version of the A48 collimator (see section 2.2.4), suitably placed so that it intercepts the deflected proton bunch before it reaches the main CDF detector vicinity.

2.2.3 Detectors

The following detectors are of particular interest because either they represent a limiting aperture and thus can possibly interact with the beam under certain conditions, or else they are dedicated to measure beam halo related events. The radiation field simulation at these detectors can directly be compared with the measurements they provide.

Roman Pots

The CDF dipole Roman Pots (RP) (Fig. 2.9) [12] set is composed of three detectors one meter apart from each other and starts with RP3 located at about 58 m from the IP, for an incoming proton. The RP horizontal edge is at 12 mm from the beam pipe axis. The scintillator part of the RP facing the beam is 2×2 cm^2. The DØ Roman Pots are made of optical fiber with the same area 2×2 cm^2.

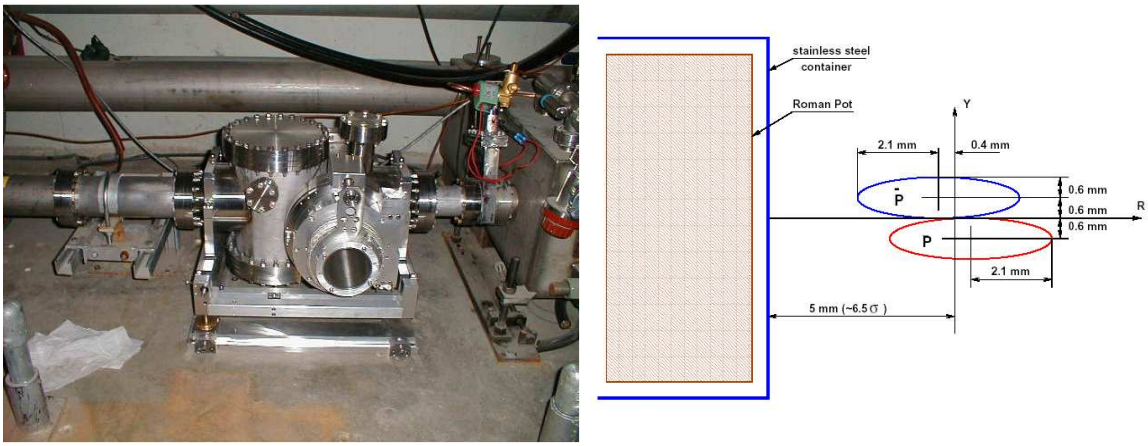

Figure 2.9: Castle of a Roman Pot detector in the Tevatron [13] (left), scheme of one possible transverse configuration of a Roman Pot with respect to the beams [14] (right).

Beam Halo Monitors

The Beam Halo Monitors (BHM) (Fig. 2.10) are scintillator counters disposed by R. Tesarek in an array of 4 detectors surrounding the beam pipe at the entrance of the CDF collision hall, both on the proton and the anti-proton side.

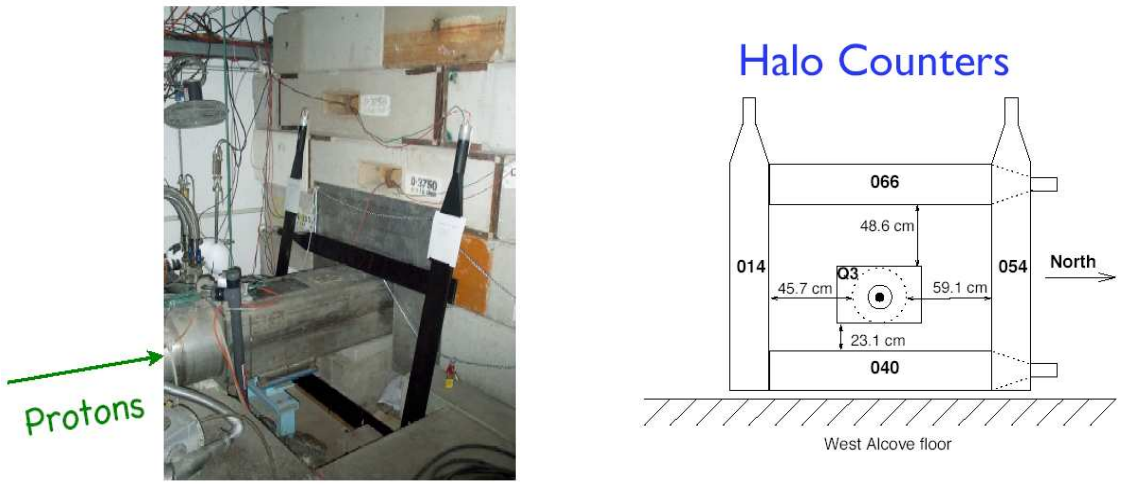

Figure 2.10: Beam Halo Monitor configuration at the CDF entrance [15].

Thermal Luminescent Dosimeters

The CDF Radiation Monitoring Group led by R. Tesarek [16] has collected an extensive set of data to determine the radiation environment in the CDF experimental hall as well as in the main detector. Thermal luminescent dosimeters detectors (TLDs) (Fig. 2.11) are installed in many locations and allow to separate dose from $\bar{p}p$-collisions and from beam losses [17]. Their sensitive parts consist of ^{6}LiF and ^{7}LiF with an emission proportional to the received dose.

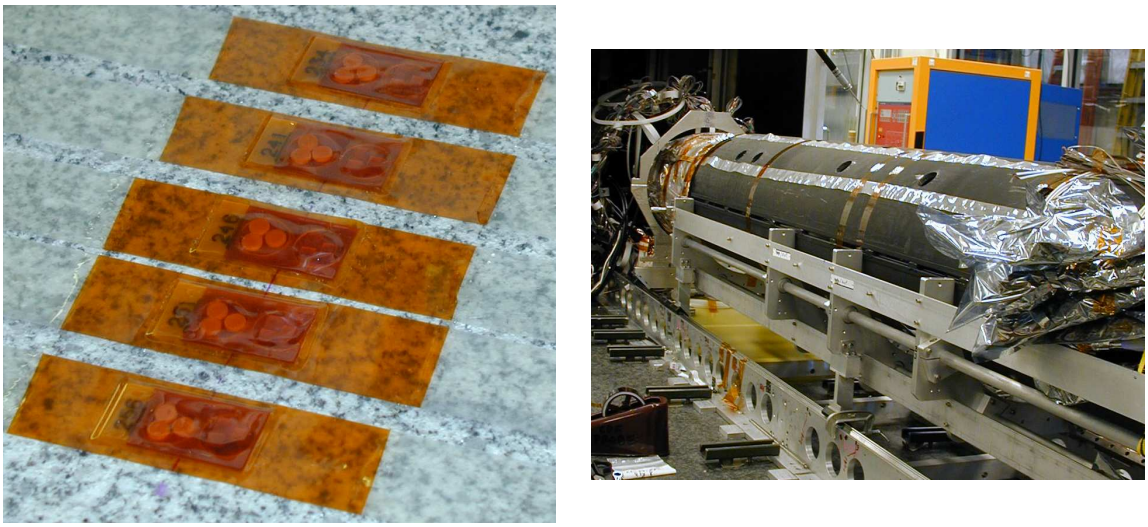

Figure 2.11: TLDs detectors sealed in kapton (left), and installed on a detector part of the inner tracking system of CDF (right).

2.2.4 A48 Mask Configurations

Several shapes and lengths of the new collimator were investigated for cost, spatial limitation and efficiency optimisation, such as an aperture of 18.3 mm×8.7 mm for "double L-shape", "single L-shape" and "minibar" A48 collimator [9] (Fig. 2.12). For the "single L-shape" version, the bottom part of the "double L-shape" version remains along with the vertical right part. In principle, the maximum material present to intercept halo is preferable; however, the only possible position of the A48 location is in front of the Roman Pots and beam-collimator interactions has to be kept minimum. The aim is the most effective protection of CDF in the event of a AKP with simultaneous minimisation of halo generated backgrounds in the RP.

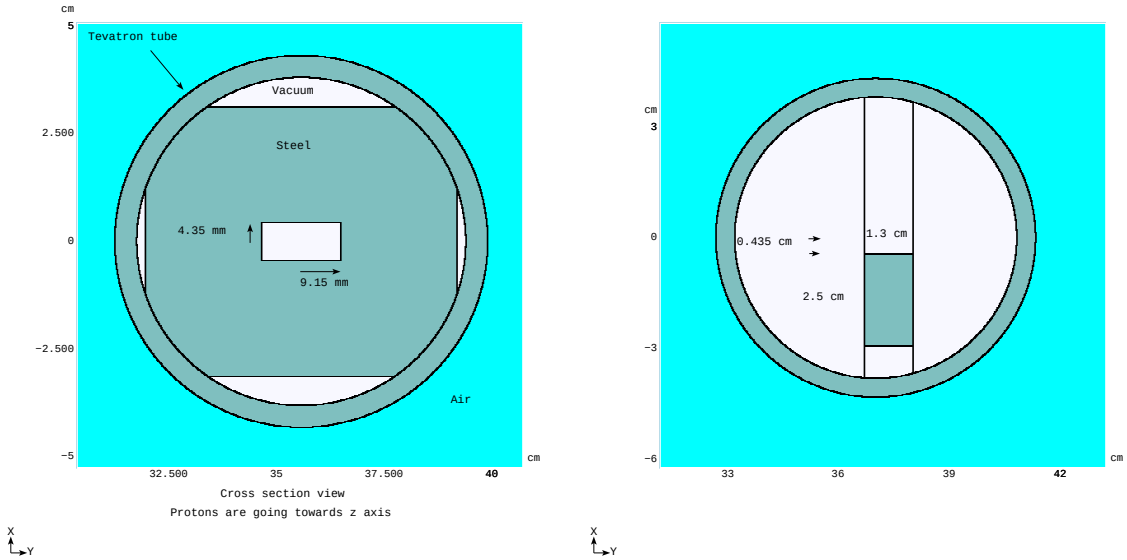

Figure 2.12: Cross section view of the A48 mask double L-shape (left) and mini-bar (right) versions.

2.2.5 A48 Mask Effect and Comparison to Data

Fig. 2.13 (left) shows the reduction up to one order of magnitude of the MARS-calculated charged particle flux in the CDF BHM with the "double L-shape" A48 collimator. The calculations are done with all three components of the beam loss

source term, with an average pressure for beam-gas elastic scattering of 10^{-10} Torr. To provide benchmarking, the simulation results without collimator are used to compare with measurements (Fig. 2.13) (right). Fig. 2.14 (left) details two contributions (inelastic is negligible) at the BHM, while Fig. 2.14 (right) shows a distribution of protons hitting the "double L-shape" collimator for the beam-gas elastic component only. The cross sections shown additionally for "minibar" and "single L-shape" versions illustrate their poor efficiency to intercept protons, about 1/6 of the "double L-shape" ability.

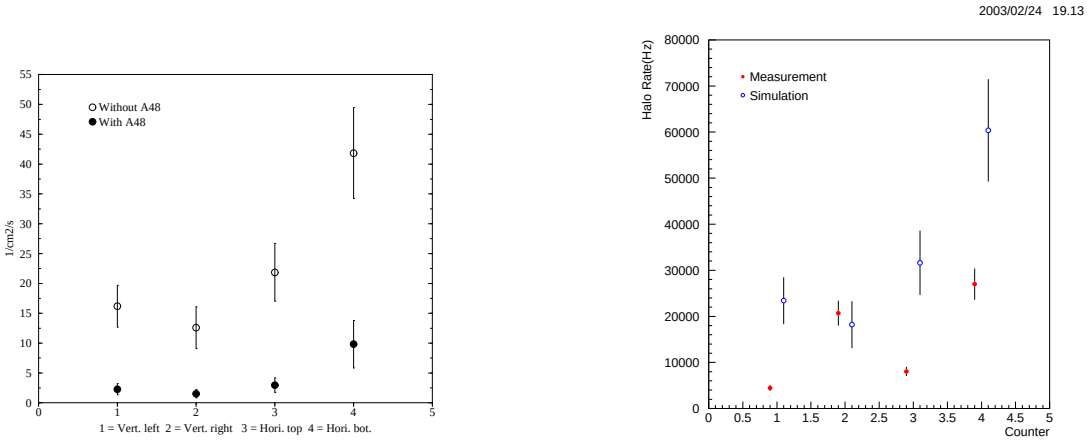

Figure 2.13: BHM hit rate with and without A48 collimator (left) and corresponding comparison of MARS calculations with data without the collimator (right).

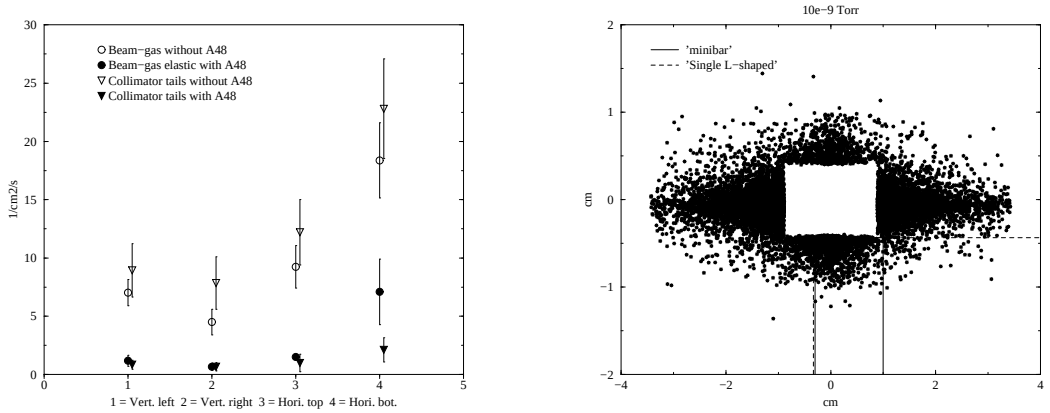

Figure 2.14: Comparison of two beam halo contributions at the BHM with and without the A48 mask (left) and spatial distribution of elastic beam-gas induced hits on several collimator configurations (right).

2.2.6 Impact on the Roman Pots

Radiation Damage

The introduction of the A48 mask in the proton path upstream of the Roman Pots may give rise to two nuisances: a possible premature degradation and effect on the lifetime of the sensitive parts, and an increase of the background levels. Fig. 2.15 compares the rates in the Roman Pot directly downstream of the new collimator due to the main beam halo contribution i.e. beam-gas elastic nuclear interactions, and a single event of a kicker prefire AKP of 2.78×10^{11} protons hitting A48 instantaneously. Several possible lengths are investigated for the collimator, in the geometrical configuration of "double L-shape". This is irrelevant in case of an AKP, but is clearly important for halo hits. A conservative case of the double jaw collimator and an average pressure of 10^{-9} Torr is considered here. With a 0.5-m steel collimator (3 interaction lengths), 0.01 rad/s is an upper limit for the absorbed dose rate in the scintillator. For a 10^7 second physics year, this corresponds to 100 krad/yr, to be compared to 20 krad for a single AKP (Fig. 2.15 (right)). Since good scintillators can withstand about 1 Mrad (estimation by N. Mokhov), none of the events should represent a concern for the lifetime and degradation of the sensitive part of the Roman Pot.

Background for Diffractive Physics: Albedo

The Roman Pot function is to detect protons scattered elastically or diffractively at the IP in $p\bar{p}$ collisions and thus to study these mechanisms. Considering their proximity to the Tevatron beams, any additional background is a major issue for their physics function. A first background component can be the albedo of anti-protons backscattered toward the pots after hitting the collimator. Fig. 2.16 shows the charged particle flux normalized to 1 proton that includes primaries and secondaries as a function of the distance in respect to the beam axis for both the backward (left)

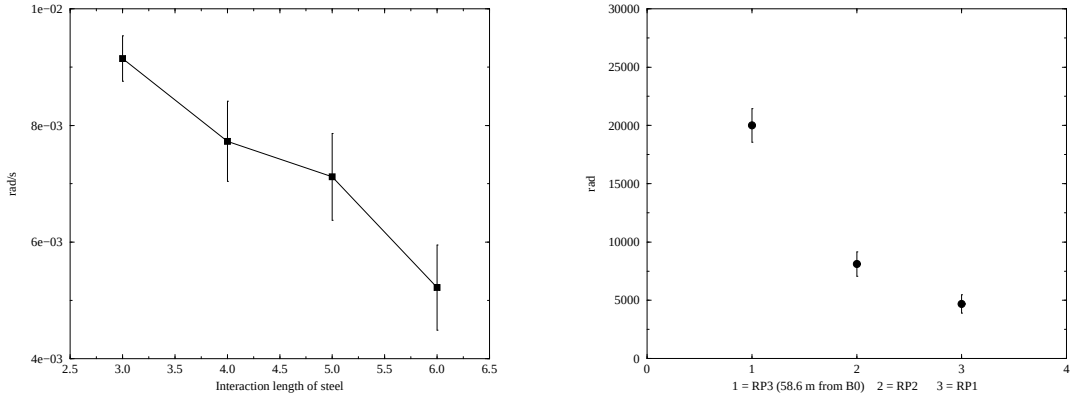

Figure 2.15: Absorbed dose rates in the RP3 due to beam halo (left) and dose in the 3 Roman Pots RP1, RP2, RP3, due to AKP (right).

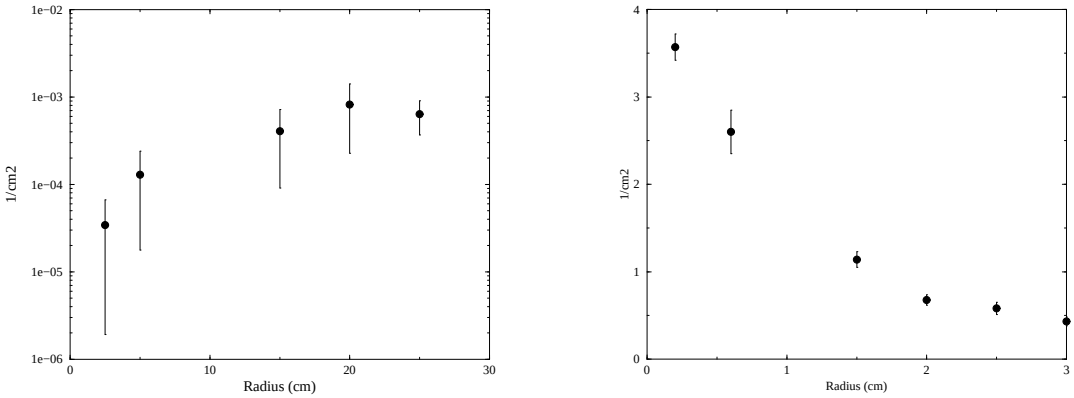

Figure 2.16: Charged particle albedo (left) and forward (right) flux in the nearest RP with a 0.5-m long steel rod.

and forward (right) directions. At a 2.5 cm radius from the initial proton beam, for the worst case, the ratio albedo/forward is approximatively 10^{-4} and does not represent a significant source of background.

Background from Beam Halo

In order to evaluate the background due to beam-gas nuclear elastic scattering (the main beam halo component at 10^{-9} Torr), the stainless steel collimator length was

varied from 0.5 to 1 m, i.e. between 3 and 6 interaction lengths with its three possible shapes. Even if the minibar shape is sufficient to intercept a deflected bunch from AKP (Fig. 2.8 (right)), the double jaw configuration is still much more efficient to protect the main CDF detector from beam halo background (cf.Fig. 2.14 (right)) with the significant drawback of increasing the background in the Roman Pots. Also the RP disturbance is a determining factor for the final collimator design. Fig. 2.17 (left) shows the effect of the length and shape of the mask on the rate of charged particles in the RP3 calculated at 10^{-9} Torr average pressure for beam-gas elastic scattering, both from secondary and primary particles contributions. Results for "single L-shape" and "minibar" shapes are not distinguishable as expected from the distribution patterns shown in Fig. 2.14. The amplification factor due to the implementation of a "single L-shape" mask of six interaction lengths of steel reaches 4.5 compared to the rates without the collimator. For a 0.5-m long "double L-shape" collimator, this difference becomes an order of magnitude (Fig. 2.17 (right)).

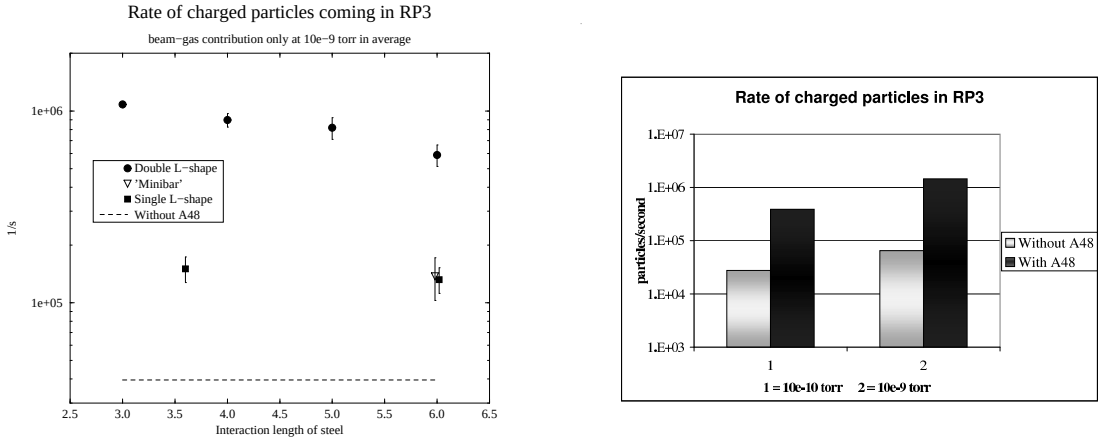

Figure 2.17: Rates of charged particles at RP3 as a function of the mask length for three shapes at 10^{-9} Torr average pressure in Tevatron (left) and their sensitivity to the gas pressure (right). The dashed line corresponds to a case without the mask.

Background from Abort Kicker Prefire

The flux of charged particles reaching the Roman Pots downstream the A48 collimator in the event of an AKP incident intercepted by the new collimator is shown in Fig. 2.18. With about 1.5×10^5 s^{-1} direct halo hits (calculated by A. Drozhdin) in the sensitive part of the Roman Pot detectors under normal conditions (i.e. without the A48 collimator), an integrated 10^7 second physics year gives 1.5×10^{12} of charged particles reaching RP3. Integrated over the area of the Roman Pot, Fig. 2.18 gives 2.27×10^{12} charged particles through 4 cm^2 of RP3, the nearest Roman Pot to the new collimator. Although the background due to a single AKP is of the same order as the background accumulated over a year, this is still an instantaneous background, probably less disturbing than a beam halo related one.

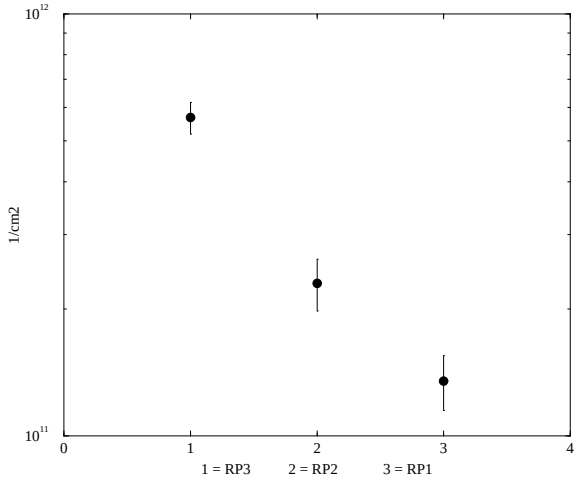

Figure 2.18: Charged particle fluence at the RP1 – RP3 pots (right).

2.2.7 Overall Protection

The shielding efficiency of the new collimator for various CDF sub-detectors is shown in Fig. 2.19 as a function of the distance from the IP for the nuclear elastic beam-gas scattering as a source. For this beam halo component, which represents the major contribution with an average residual gas pressure of 10^{-9} Torr nitrogen equivalent

(Fig. 2.20), it gives a background reduction by a factor of 4.5 to 25, depending on the distance of the sub-detector with respect to the beam line. The Beam Shower Counters (BSC) are a few centimeters from the beam pipe, whereas PLUG and BHM are of the order of one meter away from the beam axis.

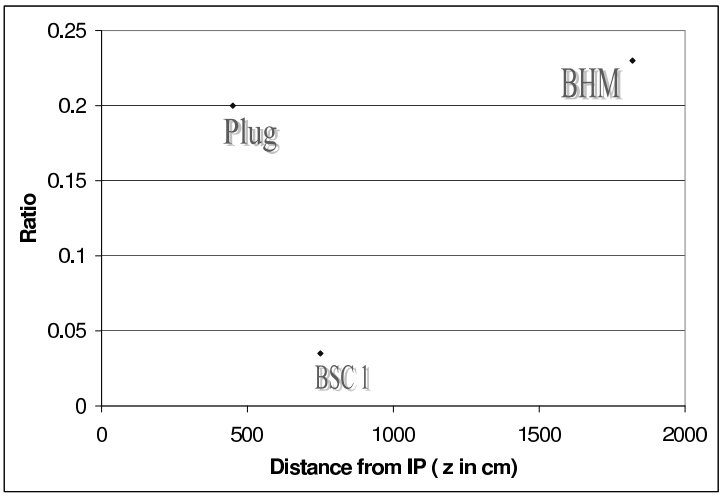

Figure 2.19: Main detector absorbed dose ratio with/without "double L-shaped" collimator for the elastic contribution as a function of the distance from the IP.

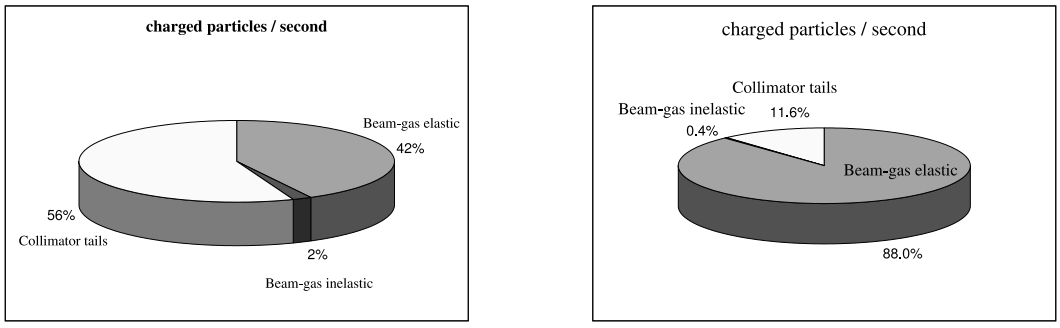

Figure 2.20: Contribution to BHM backgrounds at average pressure in Tevatron of 10^{-10} (left) and 10^{-9} (right) Torr.

Because it offers the protection needed against AKP event and its minimised impact on the radiation background of the RP detectors, the "minibar" version for the A48 collimator was chosen and installed during the Tevatron shutdown 2003.

2.3 Investigation on the Quench Stability of Tevatron BØ Dipoles

Although the introduction of the new A48 collimator constitutes a good protection by allowing the interception of a deflected proton bunch 50 meters upstream the IP instead of its loss in the separators located twice as close to the CDF center, its effects on the Roman Pots are noticeable and the "minibar" version is the most viable option. The Roman Pots are not the only elements that can be affected. Secondaries resulting from beam halo interactions with the A48 collimator (around 10^5 p/s) do not noticeably affect the downstream dipoles of the BØ Tevatron region where CDF is located; however the case of a AKP incident is different. Even if the collimator protects the downstream superconducting (SC) dipoles against damage in such an event, the secondary particles generated are likely to create a significant radiation load on the dipoles. Fig. 2.21 shows a MARS 3D representation of the region including the Tevatron beam pipe, a SC dipole downstream of the A48 collimator, with a secondary particle track sample at an AKP.

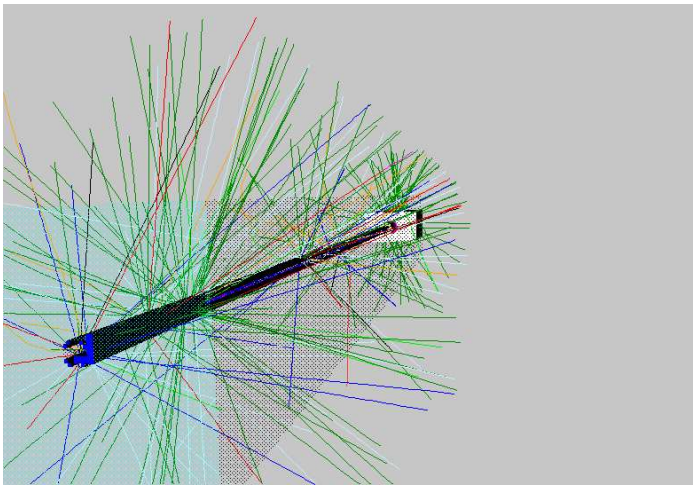

Figure 2.21: Sample of secondary particle tracks in the collimator-mask-dipole system.

2.3.1 Baseline

The baseline consists of the simulation of the retained collimator configuration with the proposed 0.5-m long steel minibar rod. Fig. 2.22 (left) gives some details of the dipole model in MARS calculations with the superconducting material, while Fig. 2.22 (right) shows the energy deposition distribution at shower maximum which takes place at about 65 cm from the non-IP end of the first dipole downstream of the A48 collimator. The energy deposition decays rapidly along the dipole length, being substantially lower in the second and third dipoles closer to the IP due to the effective shielding provided by the first dipole. Consequently, the quench stability analysis only concerns the first dipole. Fig. 2.23 shows the longitudinal energy deposition profile, separately for the right/left and inner/outer SC coils. The peak energy deposition reaches 17 mJ/g in the inner coil, that is 34 times higher than the quench limit of 0.5 mJ/g (limit suggested by N. Mokhov). It is clear that to reduce maximum energy deposition, the A48 collimator length needs to be increased, and possibilities for heavier materials and additional masks should be explored.

2.3.2 Increasing Protection Efficiency

N. Mokhov suggested that most of the energy deposited in the SC coils of the dipole is due to electromagnetic showers induced by photons from π^0-decays, caused by high-energy proton interactions in the collimator. The maximum finally allowable size for the collimator (0.5 m, about three nuclear inelastic interaction lengths λ in steel) is too short to absorb the full cascade induced by a 1-TeV proton, resulting in an excessive irradiation of the dipoles at an AKP. With no room for a significantly large increase of the collimator length, four possible cases are studied to reduce the energy deposition in the dipole downstream of the A48 collimator [18]:

1. The collimator length is increased by one interaction length (17 cm of steel), i.e., from 0.5 to 0.67 m.

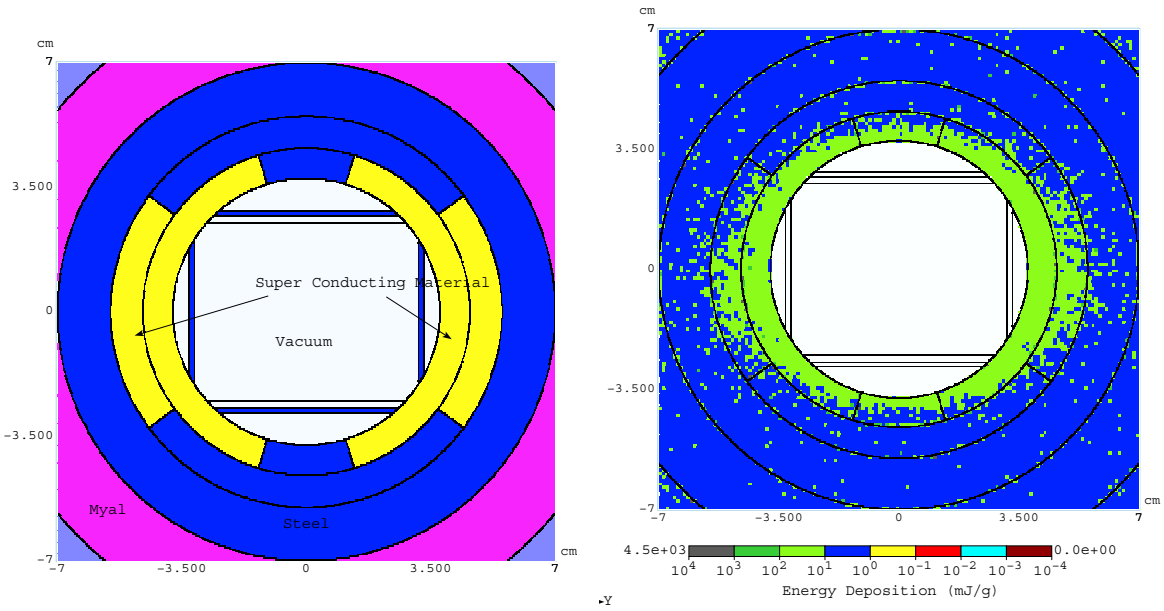

Figure 2.22: A cross-sectional view of the SC dipole in the MARS model (left) and energy deposition isocontours at shower maximum in the first dipole during an AKP event (right).

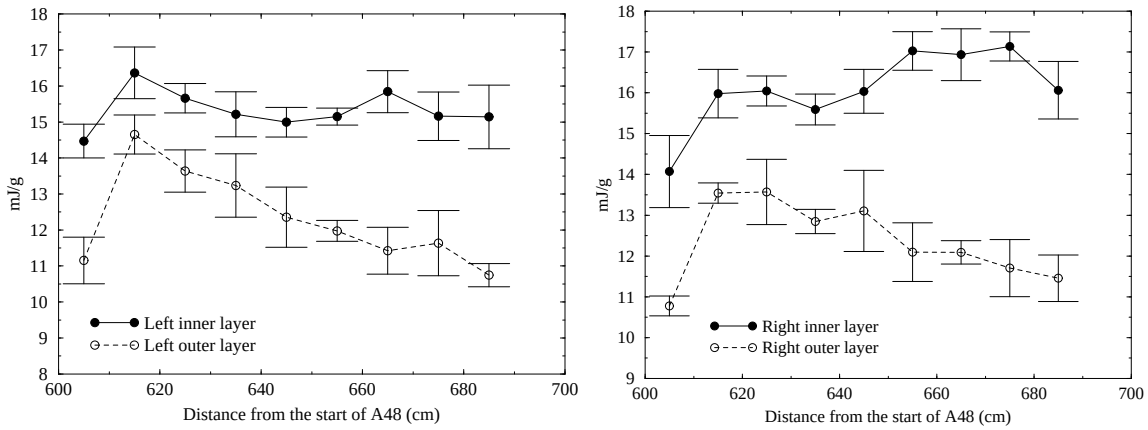

Figure 2.23: Energy deposition in the inner and outer SC coils of the first dipole.

2. In addition, a 0.34 m (2λ) steel mask with a round 2.5-cm radius aperture is placed immediately upstream of the first dipole.

3. Same as (2) with tungsten used instead of steel.

4. Same as (3) with first 0.3 m of the 0.67-m collimator made of tungsten.

Fig. 2.24 (left) shows that the energy deposition is down by about 22% for the first case. Using a steel mask additionally (Case 2) doubles the protection efficiency, reducing the peak energy deposition by 44%. It is further reduced in Case 3, but the maximum reduction is achieved in Case 4 (Fig. 2.24 (right)) where the peak energy deposition in the inner coil reaches about 3.5 mJ/g – almost a factor of five reduction compared to the baseline case. Unfortunately, even this unlikely configuration (higher cost, lack of room) of the A48 collimator and additional mask is not sufficient to prevent a quench of the first dipole.

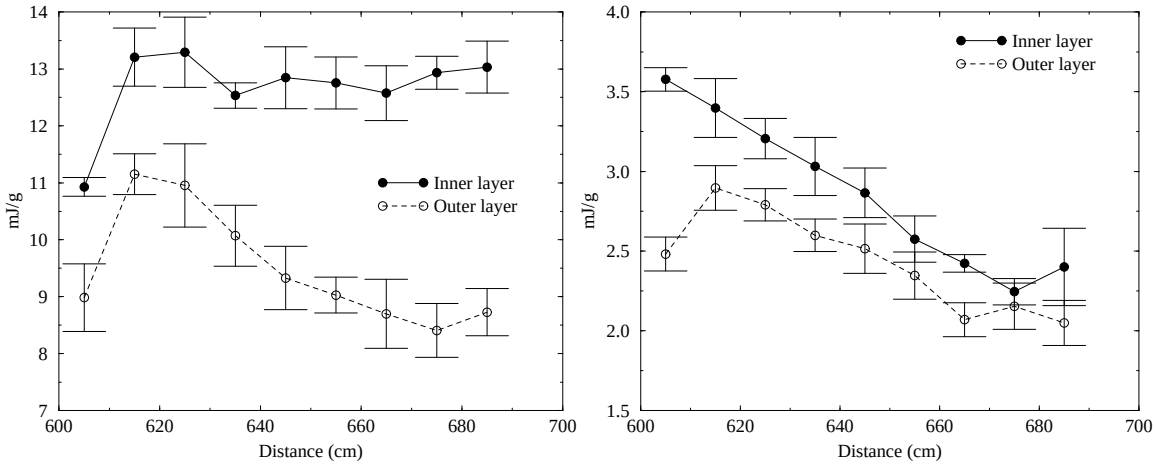

Figure 2.24: Energy deposition in the horizontal plane of the inner and outer SC coils along the first dipole in Case 1 (left) and Case 4 (right).

2.4 Radiation Background in the CDF Time-of-Flight Detectors due to $p\bar{p}$ Collisions

A Time-of-Flight (TOF) counter array located in the tracking volume of the CDF Collider detector is one of the elements of the experimental trigger. A high level of background can disturb the ability of the TOF to function correctly for this purpose, with neutrons and photons being principal constituents of this background. The main concern is related to the background induced by the secondary particle production resulting from the $p\bar{p}$ inelastic collisions in the IP, at a certain time after the collisions.

To investigate this, high energy $p\bar{p}$ collisions are simulated at $\sqrt{s}$=2 TeV with the DPMJET code [19] by N. Mokhov, and the produced secondaries are then transported within the geometry and materials of the CDF MARS model. This serves as the basis for the general study of the radiation environment of the CDF tracking volume due to collisions (cf. section 2.5), but a particular attention is given here to the TOF. For an accurate treatment of low energy neutrons, simulations are carried out with the MCNP option in MARS, using the neutron energy cutoff of 0.001 eV, whereas for all other particles, the threshold is 100 keV.

2.4.1 Neutron and Photon Fluxes

Fig. 2.25 (left) shows a longitudinal elevation view (along z, the beam axis) of the inside of the CDF tracking volume in the MARS model indicating the location of the TOF bars. Fig. 2.25 (right) gives the dependence of the neutron flux, normalized to one $p\bar{p}$, in a TOF bar (dependence is uniform in ϕ), all energies and time integrated. Only the positive part of the $z-$axis is shown since the results are symmetric with respect to the origin. Particle flux isocontours for photons (left) and neutrons (right), are shown in Fig. 2.26, with results normalized to the luminosity of 10^{32} cm^{-2}s^{-1}, with the inelastic cross section $\sigma_{p\bar{p}}$=60 mb. This represents the radiation field produced by the results of the initial collisions with all materials in the tracking volume.

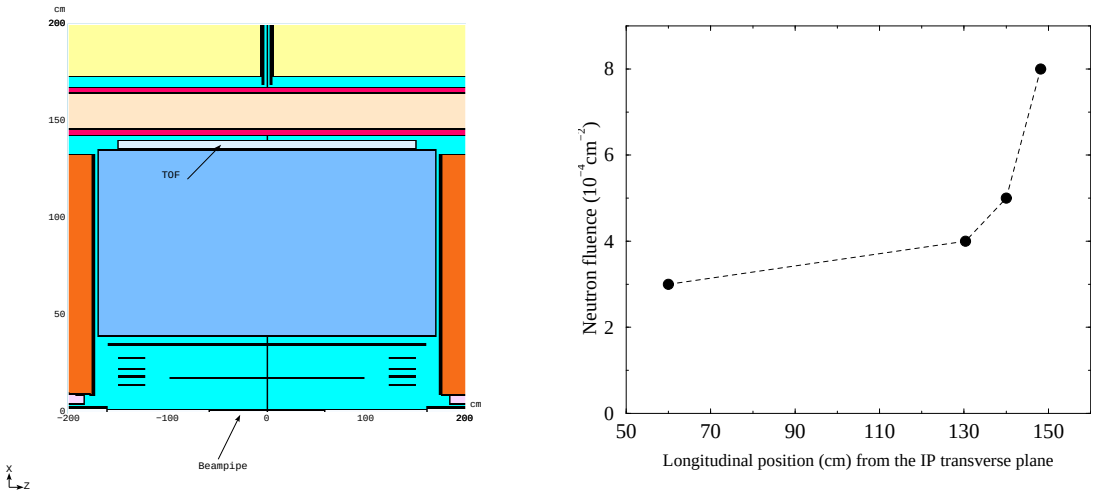

Figure 2.25: MARS view of the inside of the tracking volume (left), and neutron flux in the TOF per 1 $p\bar{p}$-collision (right).

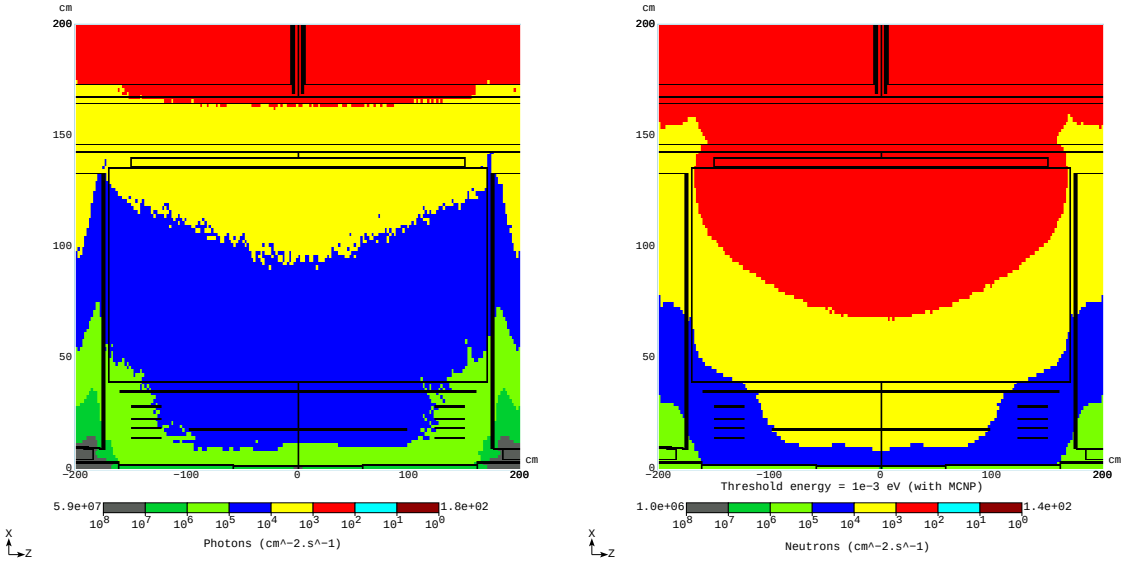

Figure 2.26: Flux isocontours normalised to $\mathcal{L}$=10^{32}cm^{-2}s^{-1} for photons (left) and neutrons (right).

Fig. 2.27 shows the energy spectrum of the population of photons and neutrons inside a box of $300cm \times 300cm \times 300cm$ centered at the interaction point. With 216 counters located at a radius of about 138 cm from the $z-$axis and a length of 300 cm, the TOF system lies inside this box.

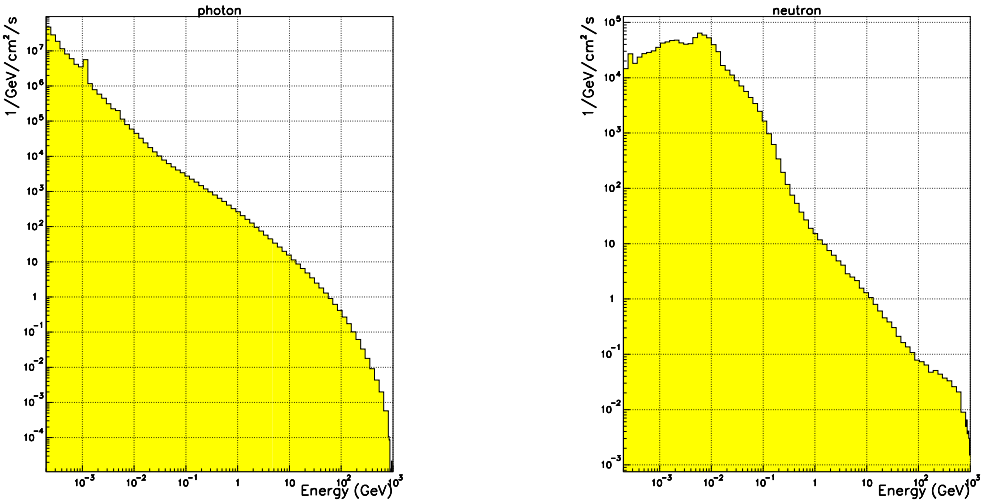

Figure 2.27: Energy spectra of photons (left) and neutrons (right) in the region of the TOF. The peak around 1 MeV for photons is due to nuclear de-excitation following neutron evaporation, the main shoulder of the neutron spectrum. This one has a component from elastic scattering around 100 MeV and inelastic at higher energies.

To estimate the possible background for the trigger, fluxes and energy spectra of particles have to be correlated with timing and the TOF material detection efficiency. A significant flux of neutrons reaching the TOF with irrelevant energy characteristics and time with respect to its detection ability, might not represent a nuisance. The time dependence of the neutron and photon arrival at the TOF as a function of energy is studied in Fig. 2.28, 2.29 with the flux of particles hitting the TOF per nanosecond.

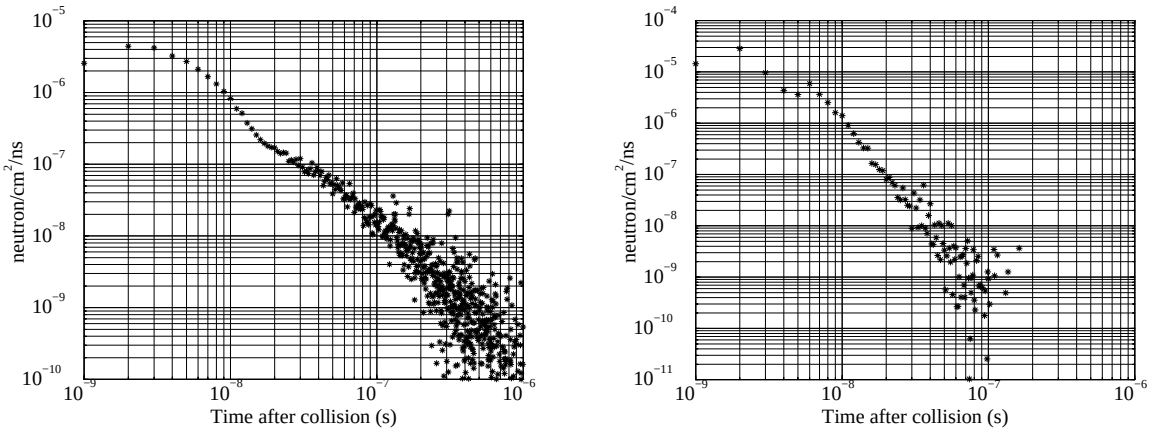

Figure 2.28: Neutron flux per ns per one $p\bar{p}$ collision in the range 10-100 keV (left) and above 1 MeV (right) *vs* time after the collision.

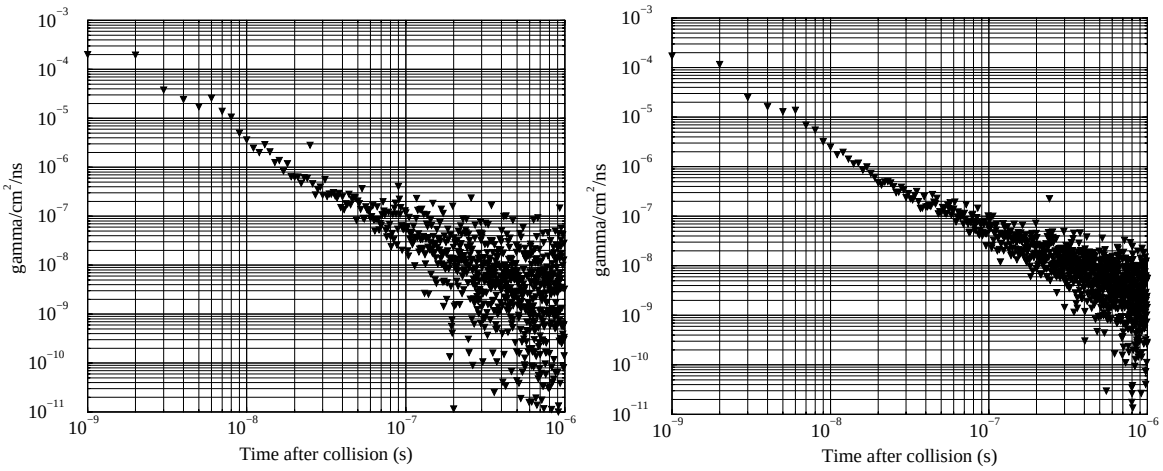

Figure 2.29: Photon flux per ns per one $p\bar{p}$ collision in the range 0.1-1 MeV (left) and above 1 MeV (right) *vs* time after the collision.

Table 2.1 summarizes the number of neutrons and photons reaching the TOF per nanosecond as a function of their energy range, for two specific times after the collision. The numbers given are averaged over 10 ns around the indicated time point. Due to the energy cutoff, no photon flux is recorded below 100 keV. No neutrons above 1 MeV were found in the TOF at 400 ns.

Table 2.1: Flux rate of neutrons and photons (10^{-9}/cm^2/ns) *vs* time after the collision.

$E_{neutron}$(keV)	10 - 100	100 - 1000	$>$ 1000
400 ns	0.52	0.01	-
500 ns	0.20	0.02	-
E_{photon}(keV)	10 - 100	100 - 1000	$>$ 1000
400 ns	N/A	11.8	6.13
500 ns	N/A	6.03	8.1

2.4.2 Effect on Bicron BC-408

The effect of the neutron and photon impact on the TOF material can be determined with a simple MARS calculation on a $4cm \times 4cm \times 4cm$ sample box. The material of the TOF is Bicron BC-408 ($C_{10}H_{11}$), with density of 1.03 g.cm^{-3}. Tables 2.2-2.3 list the particle track-length of produced charged particles when an incident neutron or photon is passing through the Bicron BC-408 with results shown in "electron.cm" and "proton.cm", as well as the energy deposited in the Bicron.

Table 2.2: Total energy deposition dE (keV/g) and charged particle track-length (10^{-4} particle.cm) in the Bicron *vs* energy of one neutron incident (keV).

$E_{neutron}$(keV)	10	100	1000
dE	0.26	1.25	6.64
electrons	1.43±0.74	0.66±0.19	0.106±0.006
protons	-	-	6.06±0.10

Table 2.3: Total energy deposition dE (keV/g) and charged particle track-length (10^{-2} particle.cm) in the Bicron *vs* energy of one photon incident (keV).

E_{photon}(keV)	500	1000
dE	0.66	1.37
electrons	0.61±0.01	3.0±0.2
protons	-	-

2.4.3 Background Expected

The TOF has a detection threshold of 2-5% of a MIP (i.e. a typical value of 2 MeV cm^2/g), such that any energy deposited in the TOF material above 70 keV/cm in average can potentially be seen by the device. From Tables 2.2,2.3, even the lowest energy deposition of 0.26 keV/g obtained with a 10 keV incident neutron would leave in one TOF bar, of mass 4.8 kg, an energy of 1250 keV to be compared to a 280 keV threshold for the 4 cm of Bicron, and hence produce a signal. Consequently all the neutrons and photons reaching the TOF deposit enough energy in the scintillator to be counted. From Table 2.1 at 400 ns, the total flux of secondaries (neutrons and photons) hitting the TOF after one collision reaches 18.46×10^{-9}/cm^2/ns, so that with 216 counters of area 1200 cm^2 each, out of what is counted in the TOF per nanosecond at 400 ns after one $p\bar{p}$ collision, around 0.47% is background dominated by photons. It has to be noted that due to the threshold of 100 keV for photons during the MARS runs, the missing data could modify the results. One can however estimate the energy deposited by a 10 keV incident photon in the Bicron, based on Tables 2.2,2.3 and the results for neutrons. A value of dE 25 times less than for an incident photon of 1 MeV can be expected, i.e. dE=0.05 keV/g which would then not lead to detection. However this is strongly dependent on the discrimator threshold and the accuracy of this evaluation, also a threshold at 5-10% of MIP [20] would probably suppress this potential contribution from low energy photons. It is not taken into account here of any other background rejection systems that the TOF may have. A new set of simulations with higher statistics will update the background prediction for the TOF [21].

2.5 Radiation Environment Simulations Inside the CDF Tracking Volume

The radiation field in the detector would ideally be dominated by the collision of the proton and anti-proton beams, but there is a substantial component coming from beam loss processes. This section describes the simulations of both contributions for comparison with data from detector measurements.

2.5.1 Contributions from $p\bar{p}$ Collisions

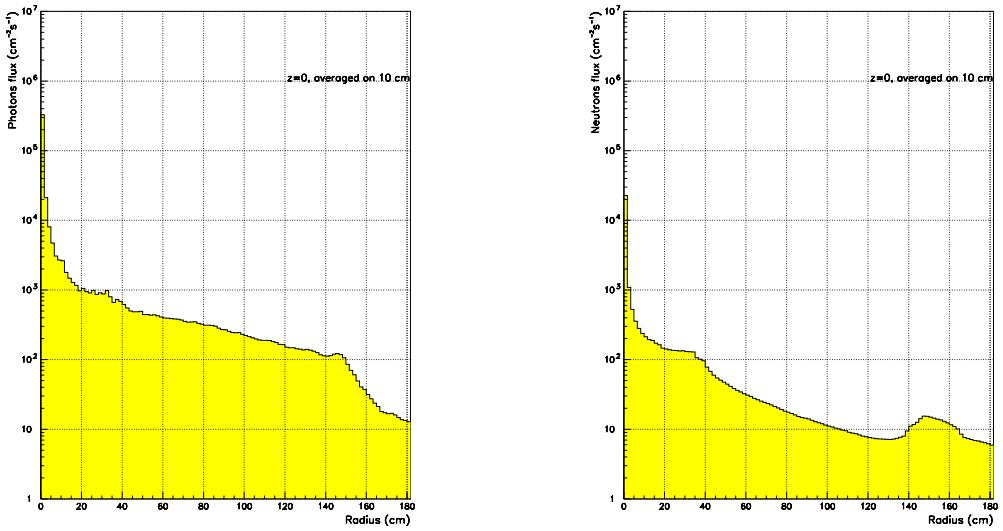

Figure 2.30: Radial dependence of the photon (left) and neutron (right) flux background 10 cm around the IP from $p\bar{p}$ source.

Fig. 2.30 (left) shows the transverse projection of the photon field isocontour from Fig. 2.26 (left) at the longitudinal location $z = 0$. The neutron field case is shown on the right. Fig. 2.31 for charged particles produced as result of the collisions, shows a symmetrical distribution similarly as for the neutron and photon field since the source is located at the IP. The designation "charged particles" refers to the sum of protons,

electrons, muons and their associated antiparticles counted in the R-Z space shown in the flux isocontour as secondary products generated by the collisions.

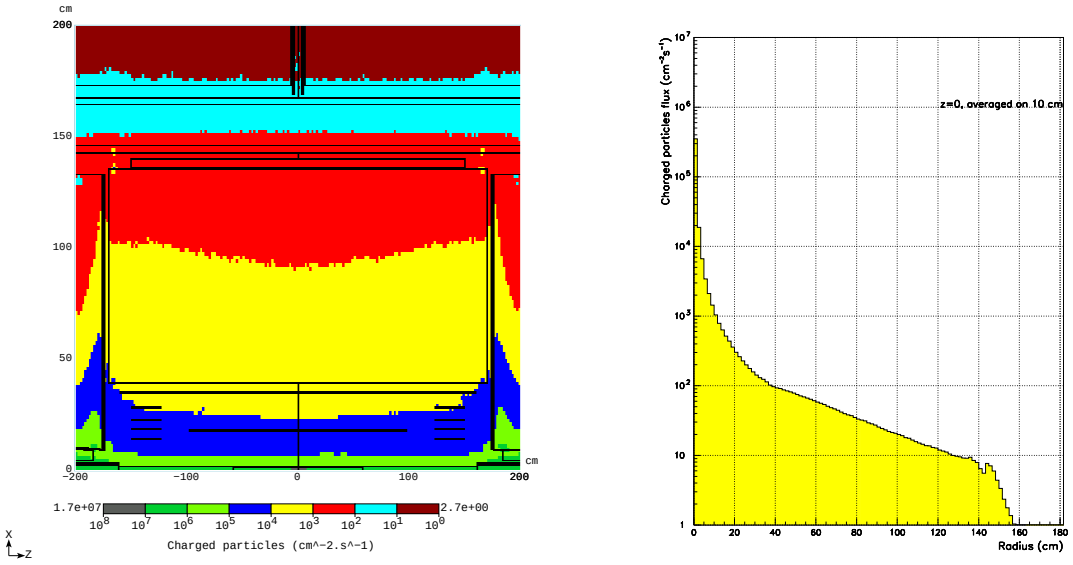

Figure 2.31: Charged particle background from collisions.

2.5.2 Contributions from Proton Losses

As with the $p\bar{p}$ collision contributions, this section presents flux isocontours of radiation background generated by the loss of the proton beam. A complete analysis of all the loss channels contributions would be rather complex, however an acceptable treatment can be achieved by analysing the dominant sources.

Beam-Gas Nuclear Elastic Scattering Channel

The location of these losses upstream the CDF detector was shown in Fig. 2.7, with a distributed pressure model used by A. Drozhdin for the STRUCT calculations. As opposed to the design of the new collimator and the evaluation of its impact, where a conservative assumption of 10^{-9} Torr for the average Tevatron residual gas pressure is sensible, an understanding of the radiation field in the detector requires a more accurate treatment of the Tevatron conditions.

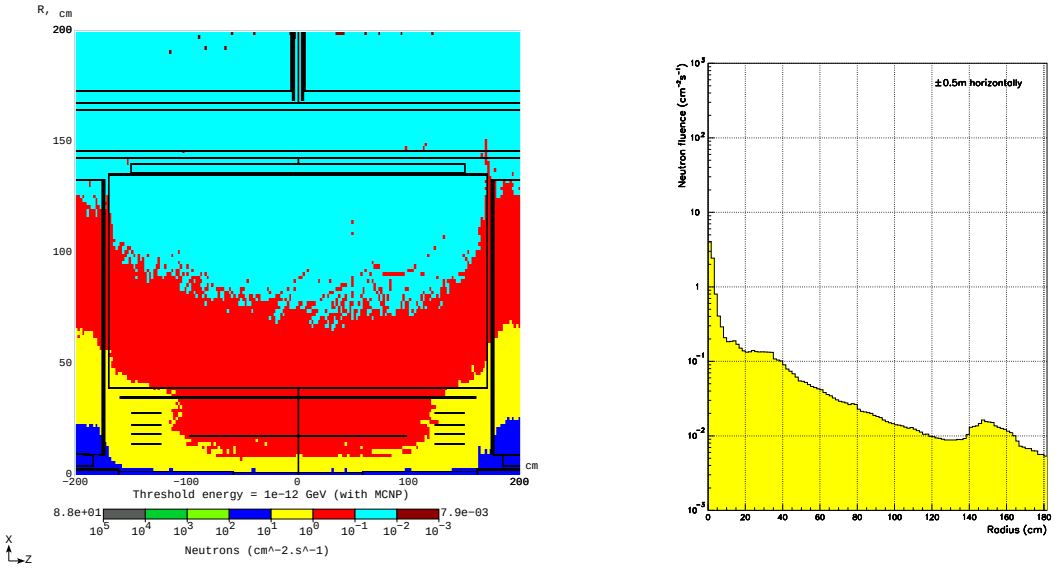

Figure 2.32: Neutron background generated from elastic losses with radial dependence at the center.

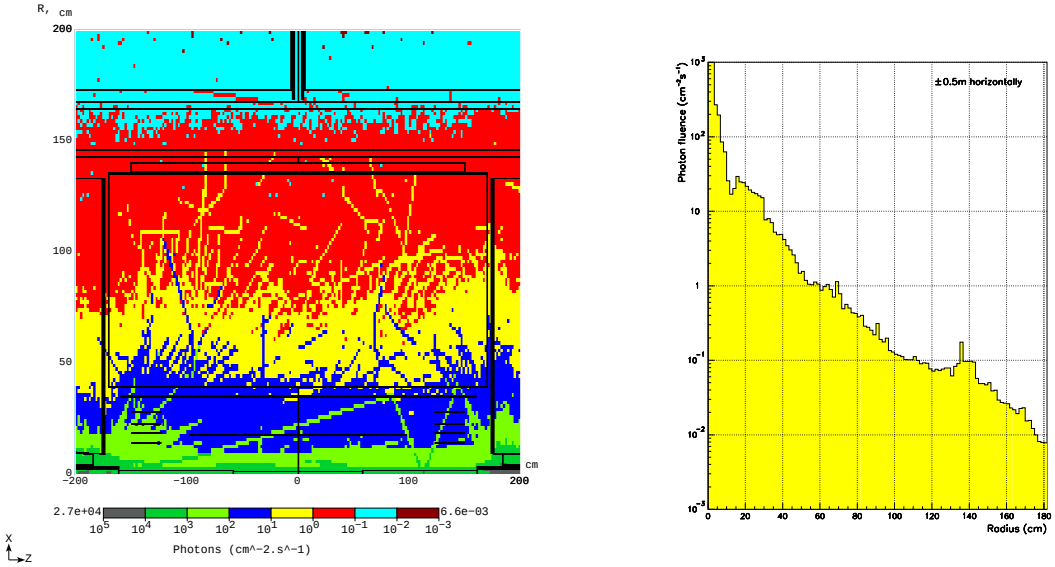

Figure 2.33: Photon background due to elastic losses.

The proton beam originates at negative z values, hence the slight build-up of the radiation field occurs along the longitudinal axis. This is not so pronounced for the neutron case (Fig. 2.32 left), where the very low energy cutoff (10^{-3} eV here) shows the fairly symmetrical neutron gas distribution, whereas the higher cutoff of 100 keV for photons and charged particles underlines their directionality. The change of the beam pipe radius at the location $z = \pm 170$ cm, the backscattered radiation, and the shielding action provided by the plugs explain the systematic peaks between the ISL and plugs (cf.Fig. 2.3), common to the three types of particles. There is a relatively low statistic resolution since losses are occurring in the Tevatron tunnel well upstream the central detector. As a result, a good resolution of the radiation field in the tracking volume is less easily achievable than for collisions contributions.

Fig. 2.35 shows the spectrum of energy for neutrons and photons due to this loss channel inside the tracking volume.

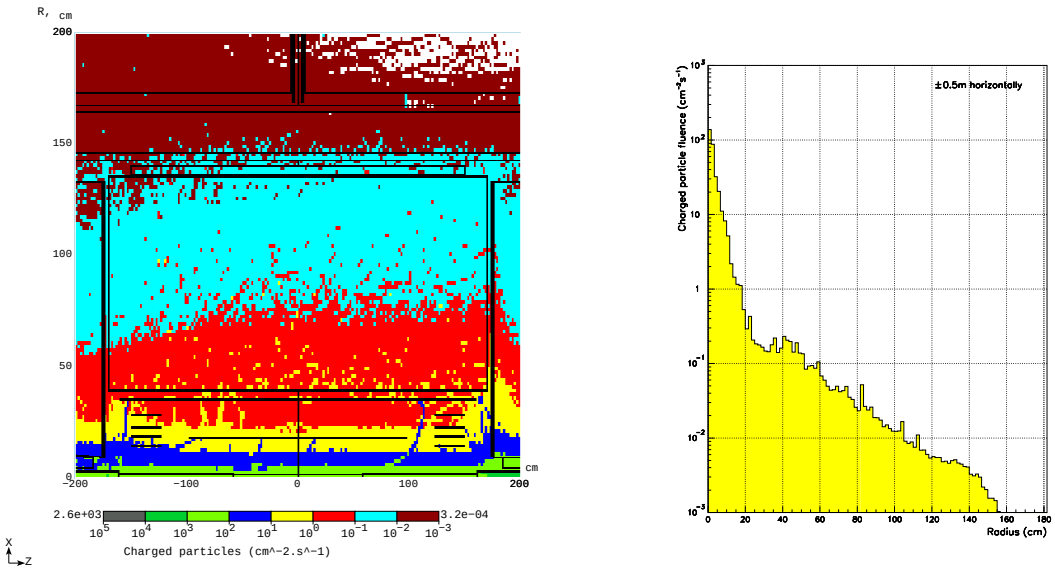

Figure 2.34: Charged particle background due to elastic losses.

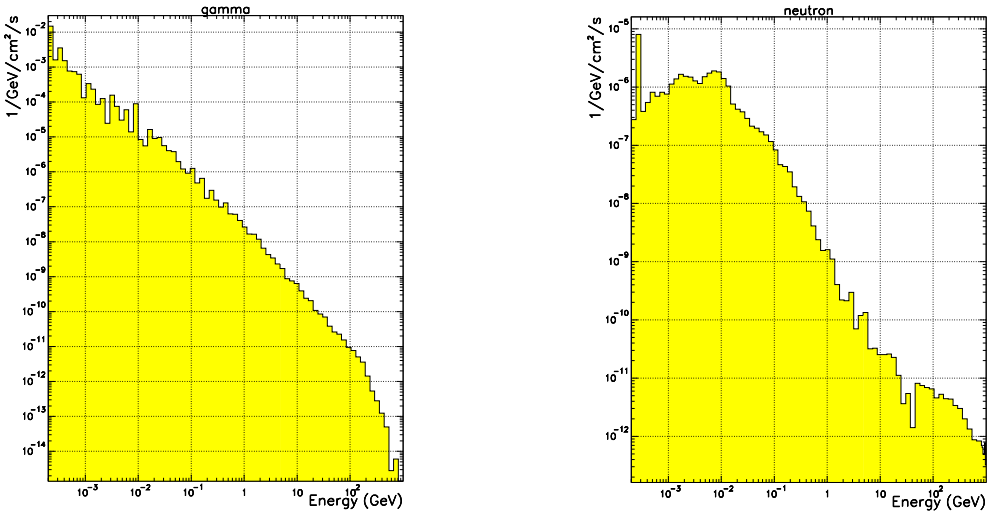

Figure 2.35: Energy spectra of photons (left) and neutrons (right) for elastic losses.

Beam-Gas Nuclear Inelastic Interactions Channel

Residual gas inside the Tevatron beam pipe around the BØ region can give a noticeable contribution to the overall radiation background in CDF through nuclear inelastic interactions. A local pressure of 10^{-10} Torr is assumed for cold region (superconducting magnets), and 7×10^{-9} Torr [22] for the remaining sections (warm region), leading to interaction rates of 62 $m^{-1}s^{-1}$ and 4334 $m^{-1}s^{-1}$, respectively (estimated by N. Mokhov). The resulting flux of the three classes of particles due to this loss channel is shown in Figs. 2.36, 2.37, and 2.38 with energy spectra for neutrons and photons shown in Fig. 2.39. The pressure assumptions taken locally in the BØ region for these calculations result in a higher contribution of this loss channel compared to the nuclear elastic one as seen previously (Fig. 2.20). They were performed with a source generation located well upstream in the Tevatron tunnel hence at a mainly cold region interactions rate mode, for results in the entrance of the collision hall at the BHM detector.

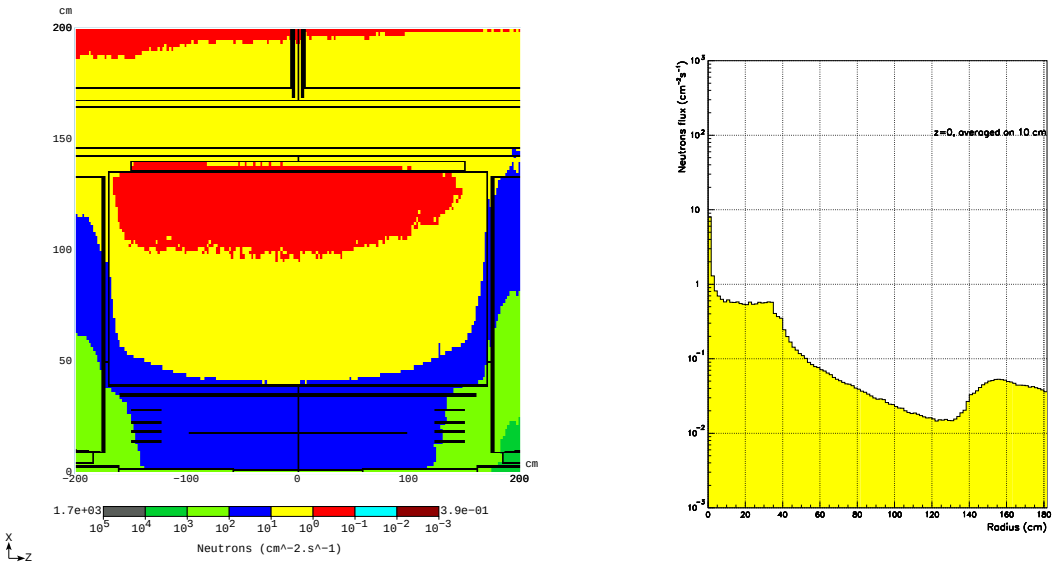

Figure 2.36: Neutron background due to beam gas inelastic interactions.

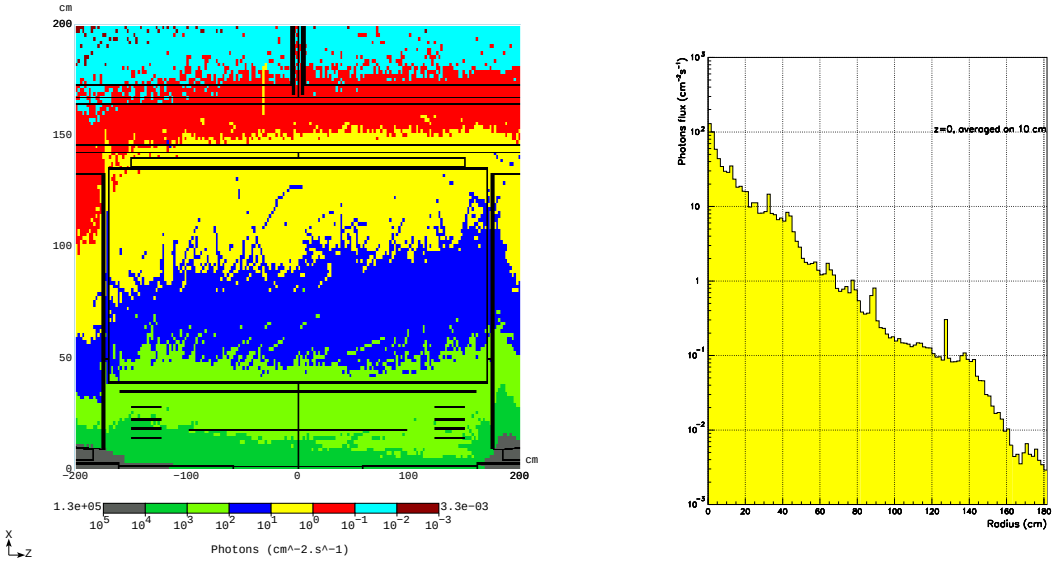

Figure 2.37: Photon background due to beam gas inelastic interactions.

2.5.3 Comparison with Measurements

Radiation simulations are one of the necessary elements for a general understanding of the accelerator/detector background. Although the model is a simplification of the real machine, e.g. for the geometry description, it is interesting to confront the model results with real measurements. In a similar way to Fig. 2.13, where a

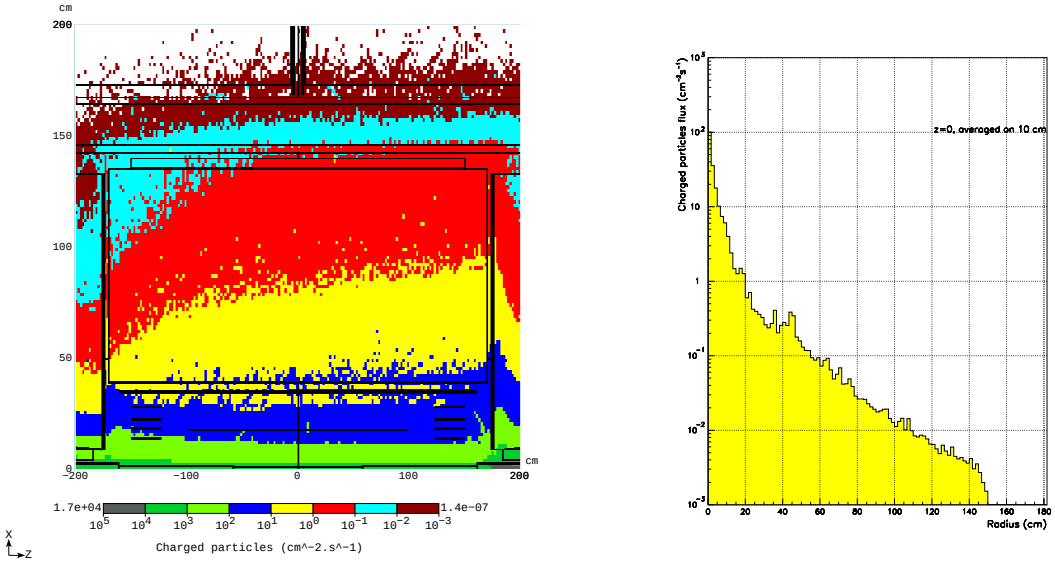

Figure 2.38: Charged particle background due to beam gas inelastic interactions.

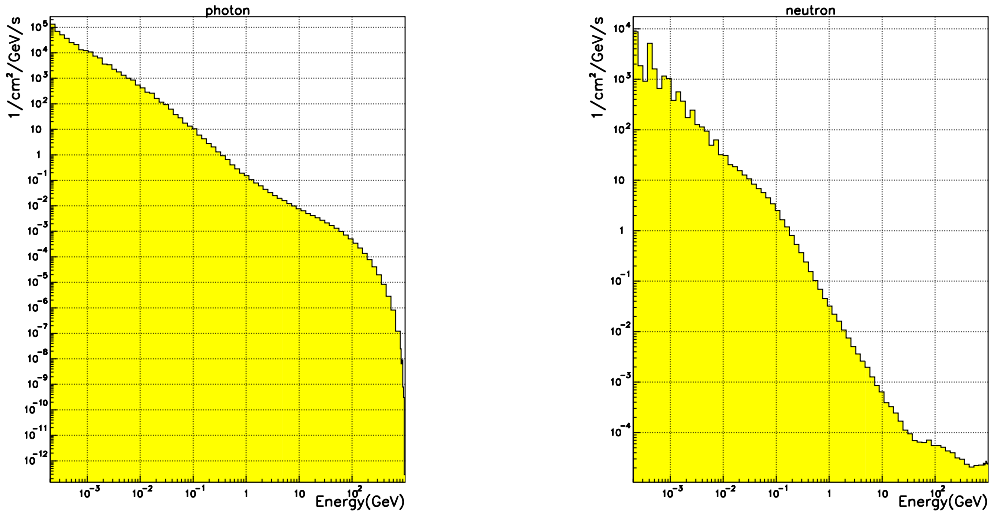

Figure 2.39: Energy spectra of photons (left) and neutrons (right) for inelastic losses.

direct comparison of the CDF MARS model predictions with measurements is shown for the case of accelerator related background, contributions from $\bar{p}p$ collisions are compared in Fig. 2.40 between TLD data and computer calculations, for the dose due to charged particles and photons. Measurements (dots) are collected by the CDF Radiation Monitoring Group along the longitudinal direction of the tracking volume, ± 1.5 m around the IP. The TLD detectors are placed at various z-positions, and at

two different radial locations with respect to the $z-$axis of the beam pipe, on the frame of the silicon detectors (cf.Fig. 2.11 right). One group is placed on the SVX at r=17 cm (upper curve) and the second is placed on the ISL at r=34 cm (lower curve) (cf. section 4.4). There are two sets of dots for each radial location, from ^{6}LiF and ^{7}LiF readings. The comparison data/simulation was done using all the contribution from the charged particle field as predicted by MARS, adding a contribution of 10% of the photon field predicted by MARS in order to match the data. This is necessary since TLD's do not see charged particles exclusively, but this small contribution from photons suggests a lack of material description in the model.

Early comparisons of loss contribution simulations and TLD detectors data in the tracking volume indicate that the radiation field is not well reproduced. Further studies are conducted with an upgraded CDF MARS model in order to explain the radiation field more accurately. A considerably more detailed geometry and material description has been implemented, and preliminary results show an improvement in the data/simulation agreement [21]. Both data and MARS calculations show that $p\bar{p}$ collisions are the dominant source of radiation background in the tracking volume.

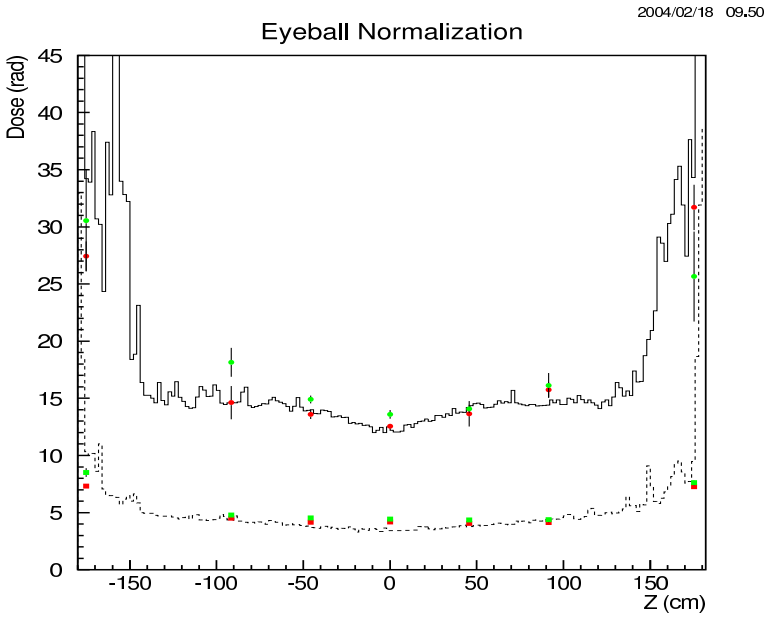

Figure 2.40: Radiation background due to collisions from simulations (lines) and measurements (dots) inside the CDF tracking volume.

Chapter 3

Beam Halo Modeling and Measurements

3.1 Measurement of the Beam Transverse Growth due to Residual Gas

Beam interactions with the residual gas inside the Tevatron beam pipe are partly responsible for the emittance growth (by means of elastic scattering) and loss of particles (by means of inelastic scattering). Both of these cause degradation of the luminosity [23]. It is therefore of potential importance for the improvement of the machine performance to evaluate the beam transverse growth due to residual gas. The method makes use experimentally of the partial scraping of the beam, and calculations with a recently developed beam transverse growth model.

3.1.1 Experimental Procedure

Several different processes are responsible for the beam halo formation [9]. Since this study aims at beam growth due to residual gas, the experimental conditions have to

be such that all other mechanisms are minimised so as to leave beam-gas interactions as the dominant effect. A beam of 150 GeV protons is injected in the machine on a central orbit with a total intensity of about 6×10^{11} protons. A large density of protons can contribute to halo formation due to intra-beam scattering, and particles repelling each other. This reduced beam population attenuates this contribution and generates less secondaries during beam scraping. To prevent particles from leaking out of the bucket due to RF noise, the beam is then debunched by removing the RF. The experiment is based on the partial scraping of the beam using a vertical collimator at the D49 section of the Tevatron (D49V), leaving a zone of high diffusion when the beam is subsequently left by itself interacting with gas. The halo population immediately outside the beam centre is dominated by the diffusion from the beam core caused by multiple Coulomb scattering, whereas further away, it is more driven by single nuclear scattering and single Coulomb scattering. It is assumed that coupling between the two transverse planes is negligible, so that a unidimensional treatment is possible.

Three measurements were made with the help of V. Lebedev and D. Still:

1. The beam is injected and partially scraped horizontally, then totally scraped with D49V, constituting the first reference.

2. Another injection follows with the same conditions, with the vertical scraping stopped before the total removal of the beam, leaving the intensity of 2×10^{11} protons. The beam is left by itself for 1.5 hours, before being fully scraped.

3. A third injection and complete scraping constitute the second reference. The two reference measurements allows measuring the beam displacement during the experiment and as an initial condition for the beam transverse evolution.

During all these measurements, the beam intensity, the collimator positions and the signal from one beam loss monitor are recorded. Fig. 3.1 shows on two different scales the evolution of the beam current in the Tevatron.

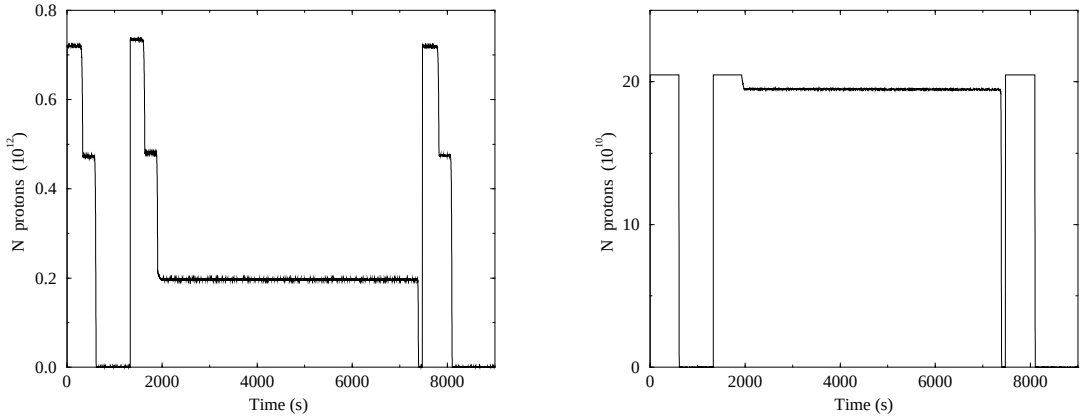

Figure 3.1: Evolution of the Tevatron beam intensity during the time of the experiment. The two references are given by the immediate beam removal, while the actual experiment consists of the beam scraping 5400 seconds after injection to allow enough diffusion time.

3.1.2 Beam Size

The beam size (and thus emittance) can be determined with the shape of the current pattern during scraping. An example is given in Fig. 3.2 (left) where the x-axis corresponds to the vertical collimator position as it is inserted toward the beam from the outside of the beam pipe, up to the extinction of the current (around -28 mm). The collimator moves from right to left, and only starts to affect the beam intensity when the position has passed -26 mm. Each point is separated by one second in time due to a data acquisition frequency of 1 Hz.

The beam centre location is given by the collimator position x_0 where the beam disappears, since the particles experience betatron oscillations. With this particular position x_0 and the initial beam intensity before the scraping, the beam size can be determined by fitting the data, assuming a Gaussian beam and using the following expression [24]:

$$N_{int} = \begin{cases} N_0(1 - e^{\frac{-(x-x_0)^2}{2\sigma^2}}), & \text{if } x > x_0, \\ 0, & \text{if } x < x_0, \end{cases}$$

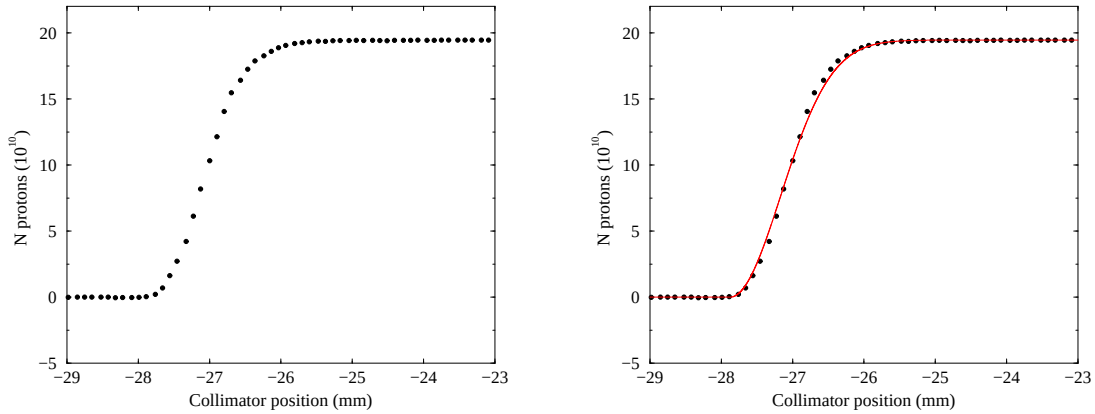

Figure 3.2: Beam scraping during the 2nd measurement (left), and its fit (right).

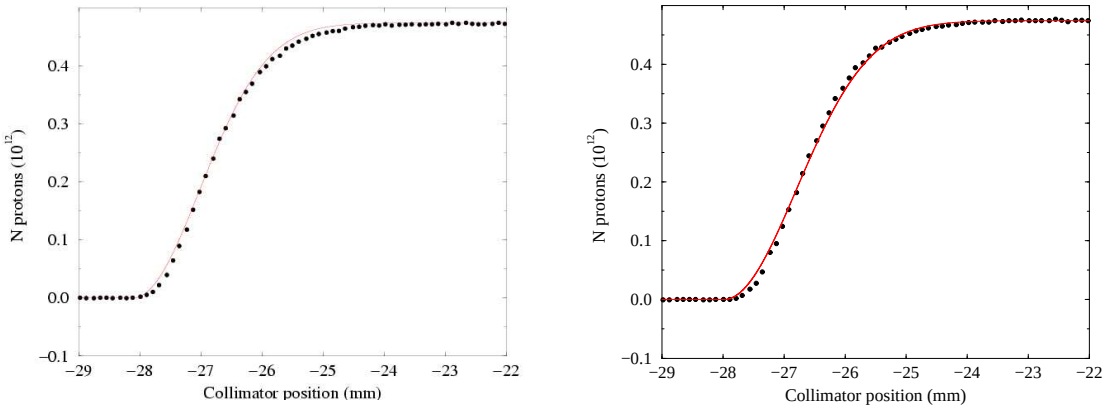

Figure 3.3: Intensity fits for the 1st (left) and 3rd (right) measurements, the two references.

where N_{int} is the beam intensity, N_0 is the initial value of N_{int}, x is the collimator position, and σ is the standard deviation of the projection of the distribution. Fig. 3.2 (right) shows a fitted example for the second measurement. Using the same method, the beam size for the 1st and 3rd measurement is obtained and shown in Fig. 3.3.

The fit of the 1st measurement is done with $\sigma = 1.07 \pm 0.02$ mm, the 3rd with $\sigma = 1.19 \pm 0.03$ mm, and the 2nd with $\sigma = 0.70 \pm 0.02$ mm. The 2nd measurement cannot be compared with the two references since the scraping was done after a delay

in time. The emittance can then be obtained as:

$$\epsilon_N = 6\gamma_L\beta_L\frac{\sigma^2}{\beta_S}$$

from the usual definition of the normalised emittance at FNAL of 95% [25], where β_S is the beta function at the location of the collimator, so that an average for the two reference measurements gives $\epsilon_N = 15.58 \pm 0.81$ mm.mrad.

3.1.3 Diffusion Speed

The beam growth is estimated by simulating the scraping pattern after 1.5 hours with the reference measurements as initial conditions. Fig. 3.4 (left) compares the two patterns, where the filled symbols are the average of the two reference measurements. Fig. 3.4 (right) demonstrates the beam displacement between the first and third measurement. It is necesary to evaluate this displacement to set the initial beam conditions for the simulation. An average is taken to this effect.

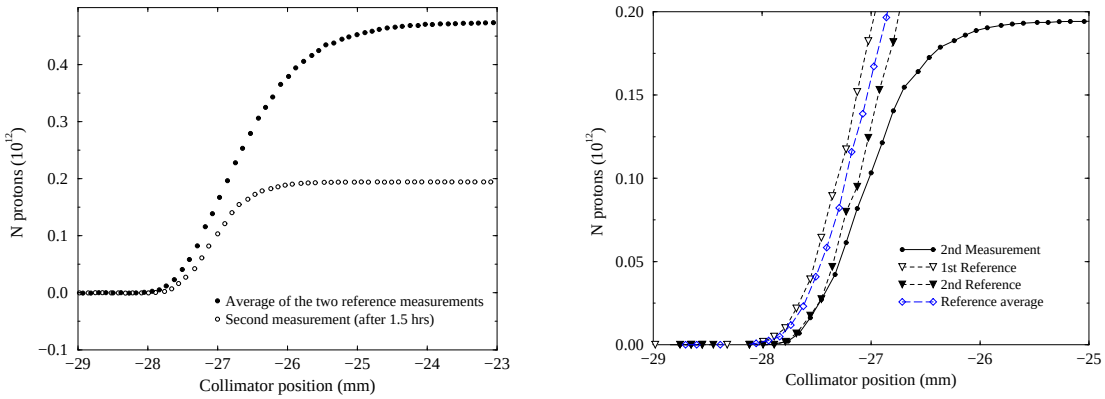

Figure 3.4: Comparison between reference and delayed scraping profile.

The evolution of the beam transverse phase-space distribution function f can be described by the Fokker-Planck equation expressed with the action variable $I = \frac{r^2}{\beta}$ [26]:

$$\frac{\partial f}{\partial t} = D\frac{\partial}{\partial I}\left[I\frac{\partial f}{\partial I}\right],$$

where t is the time, and D is the diffusion coefficient of the beam scattering on residual gas:

$$D = 4\pi\ r_e^2 v_0 \left(\frac{m_e c^2}{p v_0}\right)^2 \sum_i Z_i(Z_i+1)\ L_c^i \oint\ n_i \beta(s) \frac{ds}{L}.$$

This equation for diffusion is however not appropriate for handling large changes of the action variable I. An improved formalism including both multiple and single Coulomb scattering has been developed by V. Lebedev and S. Nagaitsev in [27]. The distribution function f now obeys:

$$\frac{\partial\ f}{\partial\ t} = \int_0^\infty W(I, I') f(I', t) dI',$$

where $W(I, I')$ is related to the proton scattering probability and includes the coefficient D. The starting distribution f^i has to match the reference measurement and the fact that the beam is scraped before being left for 1.5 hours. Assuming that the initial distribution is Gaussian, the number of protons in a region of thickness dr is:

$$dN(r) = \frac{N_0}{\sigma^2} e^{-\frac{r^2}{2\sigma^2}} r dr,$$

where $r^2 = x^2 + (\alpha x + \beta x')^2$. Changing to the action variable I, then

$$dN(I) = \frac{N_0}{2I_0} e^{-\frac{I}{2I_0}} dI$$

where $I_0 = \frac{\sigma^2}{2\beta}$, so that the initial beam distribution f^i is a truncated decreasing exponential:

$$f^i(I) = \begin{cases} \frac{N_0}{2I_0} e^{-\frac{I}{2I_0}} & \text{if } n < n_{sc}, \\ 0 & \text{if } n > n_{sc}. \end{cases}$$

This initial distribution is then propagated in time by a numerical method. The system is discretized in N bins of the action variable I, with an upper boundary value I_b being the admittance of the Tevatron, which at injection is estimated at $I_b = 1.32$ mm.mrad using calculations by A. Drozhdin. The evolution with time of each n value of f is given by:

$$\delta f_n = \frac{\delta t}{\delta I} D \sum_{m=0}^{N-1} \widetilde{W}(n, m) f_m.$$

It is necessary to compute the matrix $\widetilde{W}_{n,m}$, making use of analytical formulae given in [27] and with representation shown in Fig. 3.5 (left). Each of the matrix elements is related to the probability of the particle to be in the n, m state of action:

$$\begin{pmatrix} \widetilde{W}_{0,0} & \widetilde{W}_{0,1} & \widetilde{W}_{0,2} & \dots & \widetilde{W}_{0,N} \\ \widetilde{W}_{1,0} & \widetilde{W}_{1,1} & \widetilde{W}_{1,2} & \dots & \widetilde{W}_{1,N} \\ \vdots & \vdots & \vdots & \vdots & \vdots \\ \widetilde{W}_{N,0} & \widetilde{W}_{N,1} & \widetilde{W}_{N,2} & \dots & \widetilde{W}_{N,N} \end{pmatrix}$$

The initial distribution referred earlier as f^i is the first line of the array below, which represents the evolution in time of the distribution function $f_I(t)$:

$$\begin{matrix} f_0(t_0) & f_1(t_0) & f_2(t_0) & \dots & f_N(t_0) \\ f_0(t_1) & f_1(t_1) & f_2(t_1) & \dots & f_N(t_1) \\ \vdots & \vdots & \vdots & \vdots & \vdots \\ f_0(t_k) & f_1(t_k) & f_2(t_k) & \dots & f_N(t_k) \end{matrix}$$

The time propagation is then given by δf_n. This is best explained by an example. The transition between $f_0(t_0)$ and $f_0(t_1)$ follows from:

$$f_0(t_1) = f_0(t_0) + \delta f_0(t_0 \rightarrow t_1),$$

where

$$\delta f_0(t_0 \rightarrow t_1) = \frac{\delta t}{\delta I} D(\widetilde{W}_{0,0} f_0(t_0) + \widetilde{W}_{0,1} f_1(t_0) + \widetilde{W}_{0,2} f_2(t_0) + \ldots + \widetilde{W}_{0,N} f_N(t_0)),$$

and the same applies for all the elements of the f distribution. The δf_n relation implies a convergence condition on the time step δt, i.e. $\delta t < \delta I^2$. The simulation then runs over k iterations of a dimensionless time step $\bar{\delta t}$ satisfying this condition, and for a specific k, the quantity $\int f(I,t) dI$ is calculated and gives a profile similar to a beam intensity scraping pattern. The iteration stops when the obtained profile matches the experimental data. Fig. 3.5 (right) shows the distribution function $f(I)$ in action and its evolution with time, given the initial truncated exponential at the start of the simulation (solid line).

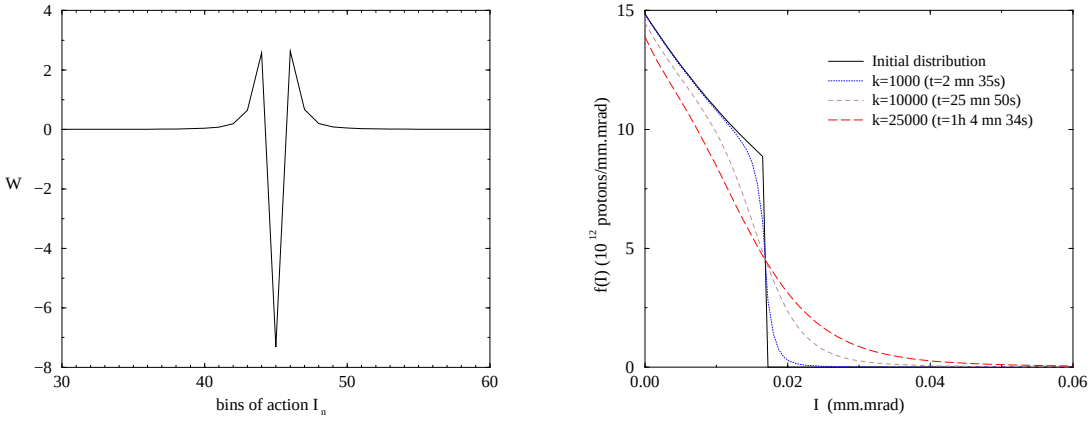

Figure 3.5: Function $\widetilde{W}$ responsible for the change in action (left) and iterations on $f(I)$ (right). A particle with a specific action is easily displaced on a short range (the two positive sharp peaks - from multiple Coulomb scattering) and there is a non zero possibility to be displaced to a higher range (smooth slope of these two peaks - from single Coulomb scattering). In any case it is displaced from its current action state (negative peak).

A good description of the data distribution (plain dots) with the initial distribution f^i (solid line) as shown in Fig. 3.6 (left) is strongly dependent on the bin size of the action variable; the finer the bin in action δI, the closer the initial value of $N = \int f(I,t)dI$ to the starting intensity. However, a δI step choice that is too small leads to inconveniently large matrix sizes and computing time due to the convergence requirement. With a suitable δI, the index n_{sc} representing the initial scraping is obtained when $\int f(I,t)dI$ equals the starting intensity, i.e. the intensity value at the moment the vertical collimator has stopped its course toward the beam and is being retracted. With a dimensionless step in time set to $\bar{\delta}t = 2.5 \times 10^{-7}$, chosen in concordance with the convergence requirement, the data are best fitted for $k = 36000 \pm 100$ as shown in Fig. 3.6 (right), with a correction to the beam position as this cannot be anticipated by the model.

The diffusion coefficient is set to $D = 1$ for the calculations; the choice of $\bar{\delta}t$ allows

then the following relation :

$$\bar{\delta t} = D\ \delta t = 2.5 \times\ 10^{-7}.$$

With a good agreement obtained for $k = 36000 \pm 100$ corresponding to the 5427 seconds of duration of the experiment (about 1.5 hrs), i.e. for $k\ \delta t = 5427$ s, the step in time is given by:

$$\delta t = \frac{5427}{k} = 0.1507 \pm 0.0004 s.$$

This gives:

$$D = \frac{2.5 \times\ 10^{-7}}{\delta t} = (1.658 \pm 0.004) \times\ 10^{-6} mm/s,$$

i.e. a corresponding beam growth of $(5.96 \pm 0.01) \times 10^{-3}$ mm/h on average.

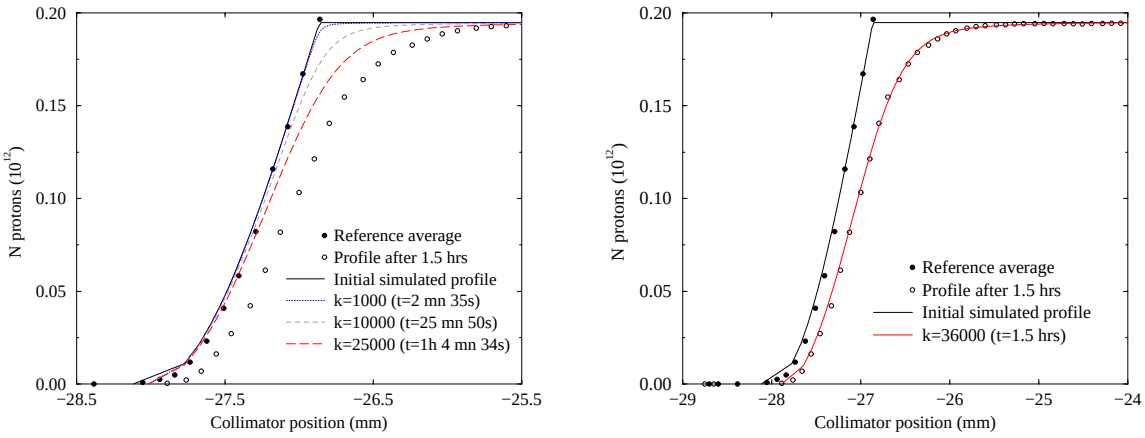

Figure 3.6: Number of particles $\int f(I,t)dI$ corresponding to the iterations on $f(I)$ shown in Fig. 3.5, without beam position correction (left), and best match to the data of the 2nd measurement (right).

3.2 Measurement of the Beam Transverse Profile

The beam transverse spatial distribution is commonly taken as a Gaussian distribution, usually an acceptable approximation to determine the emittance using collimator scans. The tail of the distribution is not however necessarily well described by a Gaussian expression [23], and the distribution of the particles referred as beam halo is not well known a priori and is likely to vary greatly depending on what halo generation mechanism is involved. A knowledge of halo characteristics in the Tevatron is rather desirable since it is a known source of background and beam degradation.

3.2.1 Experimental Method

This study also uses the standard beam diagnostic technique of the collimator scan, where the falling beam intensity pattern is recorded while the scraper is inserted. With beam intensity correlated with collimator position, the beam current vanishes then following a typical behavior as shown in Fig. 3.2 (left). A loss monitor with an increased gain can provide the necessary information on the beam centre location, i.e. the moment when the loss monitor signal disappears. In contrast to the experiment described in the previous section, the purpose is to provide a picture of the beam transverse profile rather than its growth, and so there is no partial scraping and diffusion time allowed for the beam to expand. The device used to measure the beam intensity is also of greater sensitivity for this specific application so as to allow the observation of a beam with small population. The study aims at finding the highest extent of the beam transverse tail reconstruction that is possible with this technique.

The collimator used for this experiment is the EØ proton removal collimator, a steel jaw of 1.5 m length located in a dog-leg section of the accelerator to avoid producing a direct spray of secondaries in the downstream superconducting magnet during beam collimation. To mitigate the risks for the machine during this measurement, the beam consists of protons only at 150 GeV.

3.2.2 Formalism of Beam Reconstruction from Beam Intensity Decrease due to Collimation

The intensity profile from collimation needs to be interpreted for the reconstruction of the beam density and a general treatment should be adopted. This has been described elsewhere [28] and is summarised here. In the transverse plane of Cartesian coordinates (x, y), the motion of the proton can be described by the Hill's equation [29]:

$$x'' + K(s)x = 0,$$

with projection to the $x-$axis only, where s is the curving longitudinal coordinate along the accelerator. The solution has then the form:

$$x(s) = A\sqrt{\beta(s)}sin[\mu(s) + B],$$

so that

$$x'(s) = \frac{dx}{ds} = \frac{A\beta'(s)}{2\sqrt{\beta(s)}}sin[\mu(s) + B] + A\sqrt{\beta(s)}cos[\mu(s) + B]\mu'(s);$$

introducing $\alpha = -\frac{\beta'(s)}{2}$ and $\mu'(s) = \frac{1}{\beta(s)}$,

$$x'(s) = -\frac{A\alpha}{\sqrt{\beta(s)}}sin[\mu(s) + B] + \frac{A}{\sqrt{\beta(s)}}cos[\mu(s) + B].$$

The following linear combination (where the dependence on s has been dropped for clarity):

$$\frac{\alpha}{\sqrt{\beta}}x + \sqrt{\beta}x',$$

leads to the expression

$$Acos[\mu + B].$$

Changing the variables such that:

$$\begin{cases} X = \frac{x}{\sqrt{\beta}} = Asin[\mu + B] \\ X' = \frac{dX}{d\mu} = \frac{\alpha}{\sqrt{\beta}}x + \sqrt{\beta}x' = Acos[\mu + B] \end{cases}$$

gives the result:

$$R^2 = A^2,$$

with $R = \sqrt{(X^2 + X'^2)}$. This area A^2 in the phase-space (X, X') is the emittance. With $n(X, X')$ as the particle distribution density, the total number of particles N_{tot} is given by:

$$N_{tot} = \int_{-\infty}^{+\infty} \int_{-\infty}^{+\infty} n(X, X')dXdX',$$

i.e. the density of particles at each position X is obtained when the integration on X' is performed:

$$N(X) = \int_{-\infty}^{+\infty} n(X, X')dX'.$$

It is easier to eliminate the dependence on the conjugate quantity X' by means of a variable change with R. The dependence of the particle density goes now from $n(X, X')$ to $n(R)$ and since $R = (X^2 + X'^2)^{1/2}$, $dX' = RdR(R^2 - X^2)^{-1/2}$ and the density of particles at each position X is given by:

$$N(X) = 2\int_{X}^{\infty} (R^2 - X^2)^{-1/2} n(R)RdR.$$

$n(R)$ is unknown. However from an experimental standpoint, $n(R)$ can be extracted from the scraper action, since at each step of the collimator inside the beam halo, the drop of intensity dI obeys:

$$\frac{dI}{dR} = 2\pi R\ n(R).$$

Isolating $n(R)$ and injecting it in the previous formula leads to:

$$N(X) = \frac{1}{\pi}\int_{X}^{\infty} \frac{dI}{dR}(R^2 - X^2)^{-1/2}dR.$$

3.2.3 Numerical Reconstruction

With a beam profile given by

$$N(X) = \frac{1}{\pi}\int_{X}^{\infty} \frac{dI}{dR}(R^2 - X^2)^{-1/2}dR,$$

the beam reconstruction from the decreasing intensity is performed by a numerical method. To be able to use this formula practically from data, it is necessary to have the system discretised, and for small steps of the collimator position :

$$N(X_i) = \frac{1}{\pi} \sum_{j>i} dI_j (R_j^2 - X_i^2)^{-1/2}.$$

Since the sum is a variable of the X position, which has as the origin the centre of the beam, its position is determined from the loss monitor information, and the data are converted into a function of distance with respect to the beam centre rather than the collimator position with respect to the beam pipe. With the position X with respect to the beam centre divided in $i = 1, n$ steps, $N(X_i)$ at each i step is given by:

$$N(X_1) = \frac{1}{\pi}(dI_2(X_2^2 - X_1^2)^{-1/2} + dI_3(X_3^2 - X_1^2)^{-1/2} + \ldots + dI_n(X_n^2 - X_1^2)^{-1/2})$$

$$N(X_2) = \frac{1}{\pi}(dI_3(X_3^2 - X_2^2)^{-1/2} + dI_4(X_4^2 - X_2^2)^{-1/2} + \ldots + dI_n(X_n^2 - X_2^2)^{-1/2})$$

$$\vdots$$

$$N(X_{n-1}) = \frac{1}{\pi}(dI_n(X_n^2 - X_{n-1}^2)^{-1/2})$$

The calculation of the $N(X_i)$ distribution allows to reconstruct the beam density.

3.2.4 Data Analysis

Fig. 3.7 (left) shows the beam intensity in the Tevatron for the duration of the experiment with four injections, each with subsequent immediate collimation. Initially used for the experiment, the horizontal jaw of the EØ collimator did not respond after starting partial beam removal, so that the vertical jaw was used to scrape the beam completely. Consequently, the first injection cannot be used for profile reconstruction, and there are only three beam profiles coinciding with the 2^{nd}, 3^{rd} and 4^{th} injections. To study the effect of the beam intensity on the reconstructed profile, the

number of protons in the Tevatron is increased at each injection. A primary concern for this unusual Tevatron operation is the risk of quench for the cold magnet downstream the scraping region. Fig. 3.7 (right) shows the second beam collimation where the intensity in the machine is decreasing with the position of the EØ proton removal collimator with respect to the beam pipe. Three other diagnostics are also

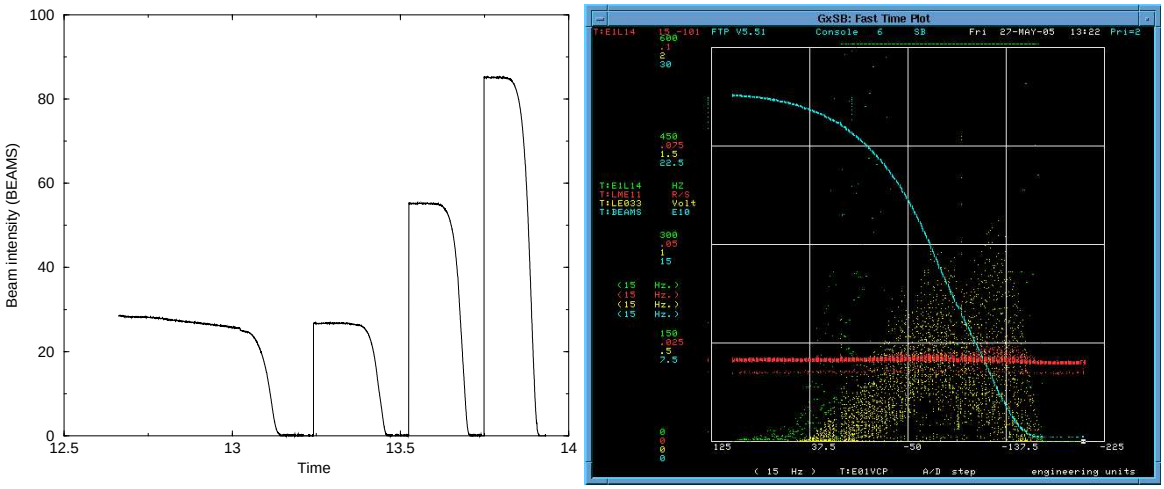

Figure 3.7: Beam intensity during the experiment (left), accelerator control readings during the beam collimation (right).

displayed, a scintillator detector and beam loss monitor response both in the vicinity of the scraping location, and a loss monitor signal at the location of the downstream cold magnet, provided by the reading of the variable T:LME11. This monitor gives a value around 0.025 rad/s of instantaneous dose with almost a flat response during the beam removal, indicating a safe operation for the magnet, below a safety limit of 0.1 rad/s (estimated by D. Still).

The beam transverse profile reconstruction method is then applied to the three valid beam removals as shown in Fig. 3.8, with an estimation of the obtained beam size using a single Gaussian fit.

The extracted σ for the three profiles are σ_1=2.077±0.002 mm, σ_2=1.913±0.001 mm, and σ_3=1.899±0.008 mm. The use of a logarithmic scale for the display of the 3^{rd} beam density transverse profile (Fig. 3.9) shows that the simple Gaussian

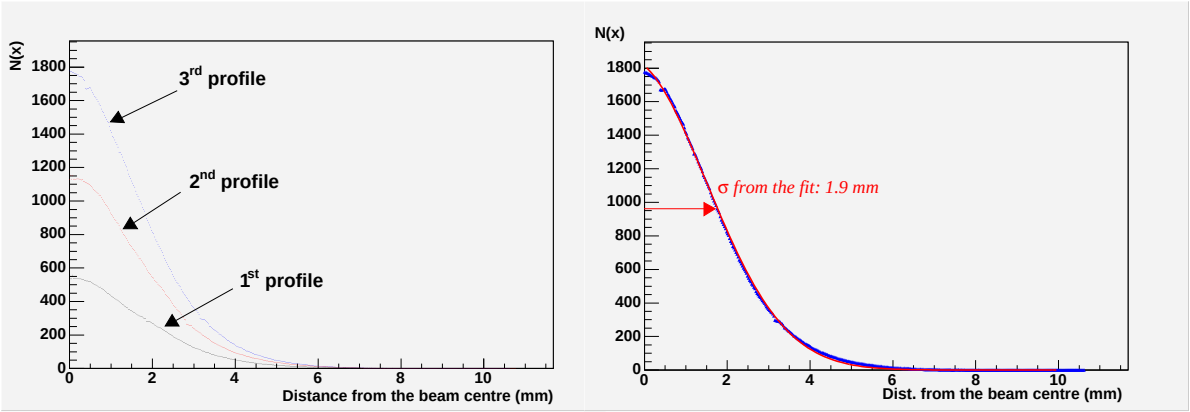

Figure 3.8: The 3 reconstructed beam profiles (left), and simple Gaussian fit to the 3^{rd} one (right).

approximation is not valid above 4 mm, i.e. 2σ. A fit with a function $N(x) = e^{-x^2/2\sigma^2} + C_0 ln(P/P_0)\frac{P}{x^2}$ [23] where x is the distance from the beam axis in mm, C_0 a pressure constant, and P,P_0 gas pressures in Torr, also does not describe correctly this profile. The collimation promptly followed the injection so that the beam tail distribution does not have time to be affected by residual gas in the Tevatron. Multiple factors determine the mathematical law of the tail population in these experimental conditions, such as the injection from the Main Injector to the Tevatron or the presence of the RF.

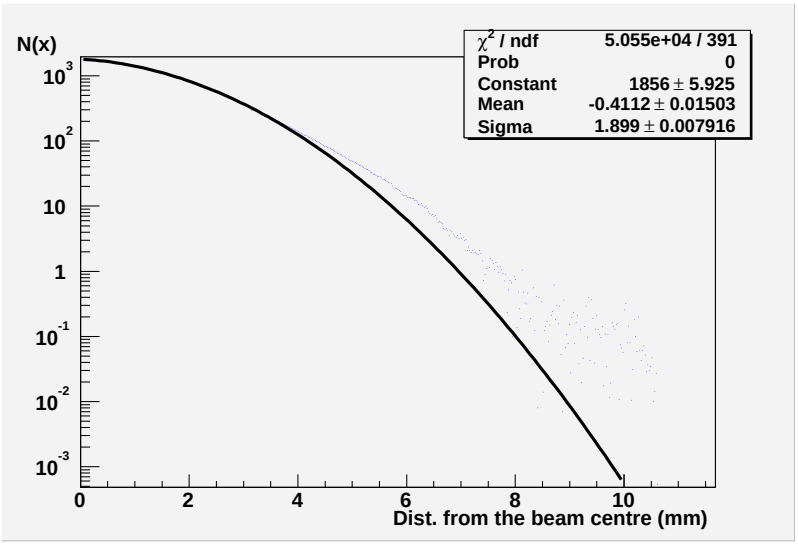

Figure 3.9: Simple Gaussian fit to the 3^{rd} profile.

The three obtained profiles can be compared by normalisation, and do not show an obvious dependence on the beam intensity (Fig. 3.10). The beam reconstruction with this technique appears possible up to 5σ, however its use to provide a beam diagnostic at the end of an High Energy Physics store at Tevatron, would need to be commissioned because of the energy and intensities involved (980 GeV, 10^{13}), which could represent a risk for the machine.

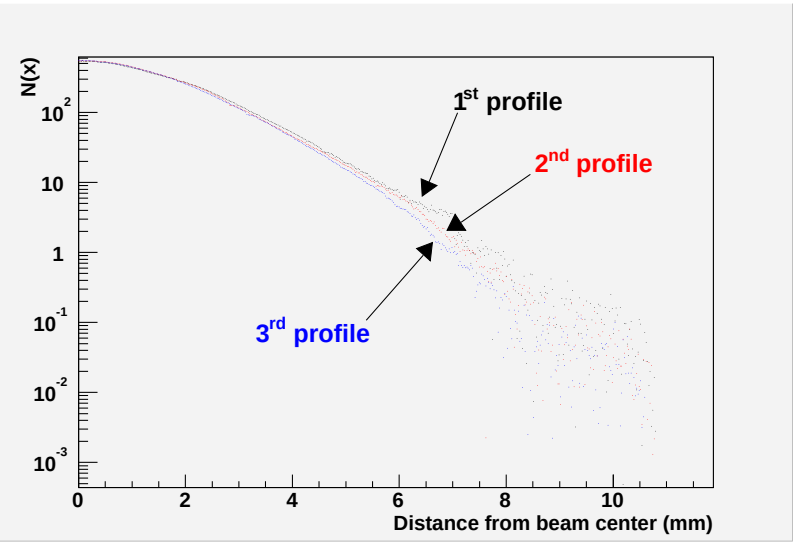

Figure 3.10: Comparison of the 3 reconstructed profiles corresponding to 3 intensities, 2.67×10^{11}, 5.52×10^{11} and 8.52×10^{11} protons.

Chapter 4

Search for a $B_c \longrightarrow J/\psi\ \pi$ Signal at CDF

4.1 Motivation

The B_c meson is a charged bosonic hadron formed of 2 quarks: a $\bar{b}$ antiquark (4.0-4.4 GeV/c^2) and a c quark (1.15-1.35 GeV/c^2). One of its decays is expected to be a J/Ψ meson ($c\bar{c}$) and a charged π meson (u, d). The present study aims at the observation $B_c^{\pm} \longrightarrow J/\Psi\pi^{\pm}$, at $\sqrt{s}$=1.96 TeV with 360 pb^{-1} of CDF Run II data. One of the primary aims in searching for this channel is to make a mass measurement using a fully reconstructed mode. The existence of the B_c meson was deduced at Fermilab in the Run I CDF data (1998) [30] with the observation of about 20 events, and later in the Run II DØ Experiment (2004) through the semi-leptonic decay $B_c \longrightarrow J/\Psi l\nu_l$. In these channels, part of the information carried by the neutrino ν_l escapes the detector. The resulting B_c mass value has a rather large uncertainty (6.4$\pm$0.4 GeV/c^2) and the lifetime is not precisely measured ($\tau = 0.46\pm0.17$ ps). The search for the identification of a fully reconstructed decay mode where all the produced particles are detected (the J/Ψ rapidly decays in two muons, both detected by CDF muon chambers), should lead, if observed, to a much more precise measurement.

Several different theoretical models predict the mass of the B_c (cf. Fig. 4.1). The experimental determination of the mass value can therefore serve as a validation of these models, which represents a rare opportunity: along with the η_b, the B_c is the only ground state meson that is at present without a precisely measured mass. The B_c is a system of a particular interest since it is constituted of two heavy quarks of different flavors, which provides a test possibility for the theory predictions of this intermediate state lying between charmonium and bottomonium. The identification of the B_c meson on the mass spectrum can also allow several other precise measurements such as its lifetime, momentum and angular distributions and thus help us to learn about its production mechanisms.

The physics project proposed to the author consists on identifying the variables to extract the signal after taking part in the Monte Carlo prediction validation, the optimisation of the cut values including studies on various resolutions as a function of silicon hits, analysis on the data, and contributions to the detection and verification of the presence of a genuine signal.

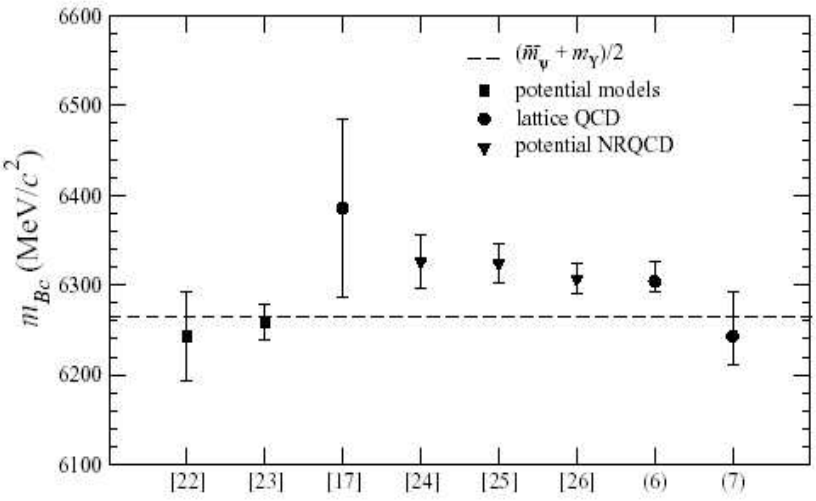

Figure 4.1: Theoretical predictions of the B_c mass from various models. The line is the average of the addition of the $\bar{c}c$ and $\bar{b}b$ meson masses. Cf. references [31].

4.2 B_c Production and Decay

The Tevatron at Fermilab provides a unique window for the production and identification of B_c mesons. The hadronic nature of the accelerated beams allows gluon-gluon recombinations, the dominant production mechanism shown in Fig. 4.2 (a) with one out of the 38 possible recombination forms [32], via the formation of $\bar{b}$ and c. The production rate is low because it involves an α_s^4 process. The B_c produced can be in excited states which decay to the ground state through electromagnetic or hadronic transitions [33]. The excited states have different masses from the ground state and their identification in some cases would need the ability to detect low energy photons, which is not possible with a good efficiency at CDF. However the ground state can be identified in suitable decay channels such as $J/\Psi\pi$.

The B_c meson can decay either with one of the two quarks as spectator while the other decays weakly, or by annihilation. For the spectator decay mode, the $c-$quark decay accounts for about 65% of the contribution to the B_c decay rate, while the $b-$quark decay represents a contribution of 25% [34]. This is the decay mechanism experimentally studied here and illustrated in Fig. 4.2 (b).

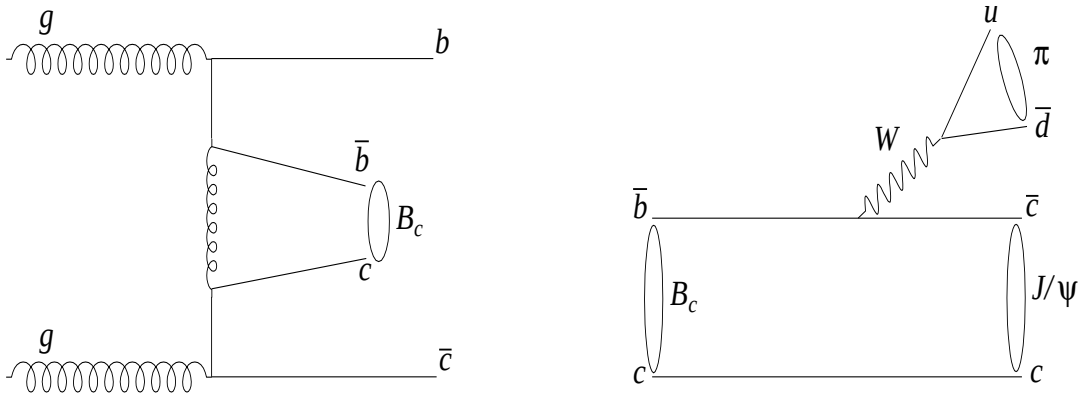

(a) (b)

Figure 4.2: B_c generation through recombination mechanism (right), and Feynman diagram of the B_c decay through the spectator model.

4.3 Analysis Strategy

4.3.1 General Considerations

The aim of the analysis is to use CDF data to identify the signal of the $B_c \longrightarrow J/\Psi\pi$ decay. The search strategy consists of evaluating physical quantities whose characteristics for a B_c decay signal would be significantly different from those of the background. Discriminating against the background accordingly, using analysis cuts that are optimised for this purpose, should then improve the possibility to observe a resonance in a mass spectrum - i.e. a peak - at the value of the B_c invariant mass (as illustrated in Fig. 4.4 for the $B^{\pm}$ case). It is not guaranteed a priori that such a resonance can be seen, despite the fact that the existence of the B_c has been deduced from the previous experiments and that it is predicted by theoretical models, since the production cross section of B_c as well as the $J/\Psi\pi$ decay cross section are known as limits only. Also the capability of the detector, both on the hardware and software sides, plays an important role in searching such a small signal. Below we discuss the observation possibility at CDF before conducting the analysis.

The choice of this B_c decay channel is motivated as follows. The final products are three charged particles, a simple 3-body topology, and there is a very well defined mass peak of the J/ψ decaying into two muons, associated with one charged track coming from the same vertex. The majority of the background comes from prompt J/ψ and prompt pions, i.e. particles produced at the primary vertex, and a cut in decay length should largely suppress this contribution. However the lack of precise knowledge of the B_c meson lifetime makes the use of this cut slightly dangerous. A source of background is due to J/ψ's that come from $B-$meson decays and that are wrongly associated with charged tracks; a good strategy to reduce this is a precise determination of the decay vertex, in order to cut at the minimum possible decay length, and to precisely determine the vertex fit probability. The analysis is consequently well suited to the CDF detector and makes full use of its tracking power.

4.3.2 Blinding Procedure

The predicted cross section and branching ratio for $B_c \longrightarrow J/\psi\pi$ production are small. Thus our expectations are not to find a large resonance peak, and the conclusions of the analysis are liable to interpretation. Therefore, a neutral position on the study is adopted in advance in order not to bias the result. This is achieved by blinding the mass spectrum of the region where the B_c could be, and by conducting the search method without looking at the signal. It is known to be possible to make "resonances" appear by means of analysis artifacts, and the blind analysis offers a suitable protection. An important consequence of this strategy is that *all* the criteria of the analysis that we propose to reveal and interpret the signal have to be evaluated and reviewed *before* the study of the data. Fig. 4.3 gives a representation of the blind method that was adopted, where the histogram shows the entries as a function of the mass spectrum. The region below 5.6 GeV/c^2 has information entered in bins of 50 MeV/c^2, with 2 bins only after 5.6 GeV/c^2. The width of these two bins is chosen to be large so as not to allow us to see structures, and any kind of fine tuning is made impossible. The centre of the blind region, covering 5.6 to 7.2 GeV/c^2 is at the PDG B_c mass value: 6.4 GeV/c^2, and the 0.8 GeV/c^2 bin size corresponds to twice the PDG uncertainty on the B_c mass (0.4 GeV/c^2).

The blind mass window is large with respect to the predicted searched signal width ($\sim$15 MeV/c^2 from Monte Carlo simulations); therefore the data from the whole blind region is considered as background, since our hypothesis is that a signal contribution is small.

4.3.3 Use of a Reference Decay: $B^{\pm} \rightarrow J/\Psi K^{\pm}$

As the mass, lifetime and p_T spectrum of the B_c are not precisely known, it is not possible to rely completely on Monte Carlo samples to optimize the cuts that will

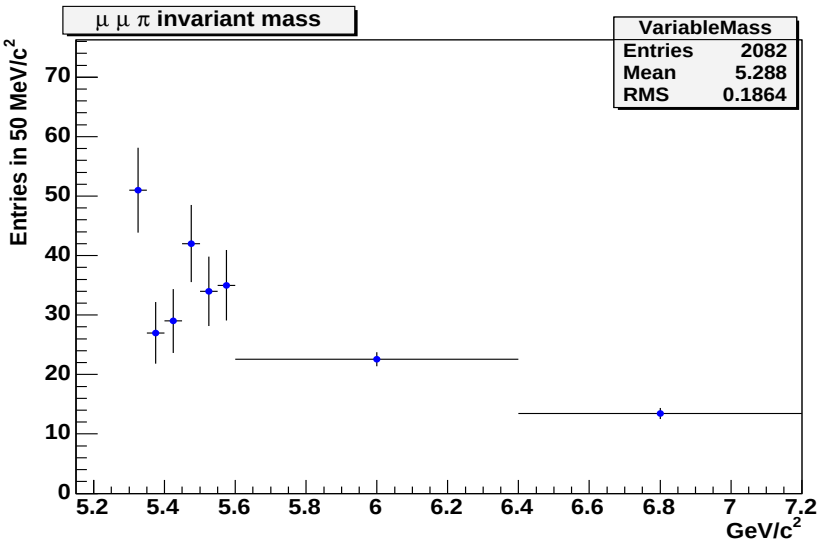

Figure 4.3: Blinded region of the $J/\psi\pi$ mass spectrum.

be used to reject background relative to signal. For this reason, the analysis of the B_c decay is conducted with reference to the decay of the $B^{\pm}$ meson via the channel $B^{\pm} \to J/\Psi K^{\pm}$, where about 3600 events in total are present in approximatively 360 pb^{-1}. This is referred as the control sample and is used to establish the expected yield of a B_c signal. The mass, the lifetime and possibly the p_T spectrum are different, but this decay has the same topology as that of the B_c, so that for certain aspects, as will be shown later, no differences between the two samples are expected.

The events comprising the control sample are selected from the same data stream than for B_c, allowing us to perform quality controls of the data. During the Tevatron operations, the 360 pb^{-1} of data were acquired with the Central Outer Tracker (COT, a detector component of CDF) before and after a period in which the COT showed symptoms of aging. There is therefore a need to validate the use of the data as a function of this detector state. To do so, the signal yield of the control sample for both datasets (before and after aging) is compared with the yield obtained in a $B^{\pm}$ lifetime analysis performed by CDF [35], using the same cuts that were ideally suited for assessing vertex properties. They are as follows:

- 3 hits on SVX layers
- Muon matching $\chi^2 < 9$ on all muon types.
- Vertex probability $> 0.1\%$
- $|M_{J/\Psi} - 3096| < 80$ MeV/c^2
- $P_t(K) > 2.0$ GeV/c, $P_t(B^{\pm}) > 6.5$ GeV/c

with the resulting mass spectrum shown in Fig. 4.4. Table. 4.1 shows that the yield in the first dataset (COT aged) is compatible with that of the lifetime analysis, whereas for the second dataset, there is a slightly larger yield, explained by a larger trigger efficiency for the recovered COT. However mass and width values are comparable, which validates the use of both datasets of COT condition.

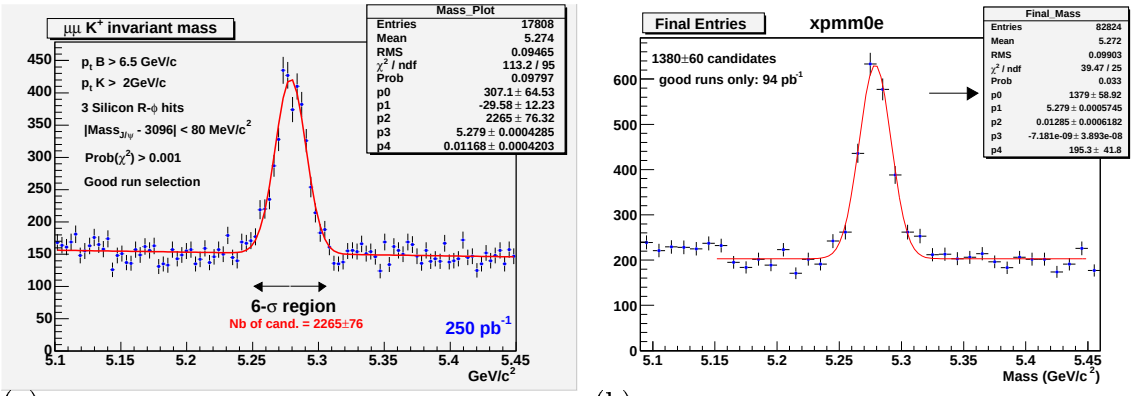

(a) (b)

Figure 4.4: Mass peak of the $B^{\pm}$ for the two datasets, before the problem on the COT (a), and after its recovery (b).

The number of predicted B_c signal events can be evaluated with:

$$RN\frac{\epsilon_c}{\epsilon_u}$$

where R compares the number of B_c mesons produced during $\bar{p}p$ interactions with a subsequent decay into the $J/\psi\ \pi$ channel, with the numbers of $B^{\pm}$ mesons produced

dataset	$\mathcal{L}(\mathrm{pb}^{-1})$	Candidates	Yield (pb)	Mass ($\mathrm{GeV/c^2}$)	Width (MeV)
$B^{\pm}$ lifetime	70	710 ± 50	10.14 ± 0.71	5278.8 ± 1.1	15.2 ± 1.1
dataset (a)	250	2265 ± 76	9.66 ± 0.32	5279 ± 0.43	11.68 ± 0.42
dataset (b)	108	1379 ± 59	12.8 ± 0.5	5279 ± 0.6	12.6 ± 0.6

Table 4.1: Comparison of yield, mass value and width of the $B^{\pm}$ between various data samples. The data (a) is before the COT problem, (b) is data after its recovery. The 70 pb^{-1} of data for the $B^{\pm}$ lifetime analysis is part of the dataset (a).

and decaying in the $J/\psi\ K^{\pm}$ channel:

$$R = \frac{\sigma(B_c) \times \mathcal{BR}(B_c \to J/\psi\pi^{\pm})}{\sigma(B^{\pm}) \times \mathcal{BR}(B^{\pm} \to J/\psi K^{\pm})},$$

and N is the number of $B^{\pm}$ signal events in the control sample. ϵ_u and ϵ_c are the detection efficiencies for the $B^{\pm}$ and B_c mesons respectively, when some cuts are applied indicating the attained sensitivity. Based on various theoretical results and experimental measurement, R is estimated to $0.8 \pm 0.1\%$ [36].

4.4 The CDF Detector

The Collider Detector at Fermilab (CDF) [33] has already been described in connection with the MARS radiation background simulations discussed in chapter 2. The names and types of detectors, as well as the reconstruction stage were also briefly introduced. A description of the different parts of the detector that play a role for the signal search is presented in the following section.

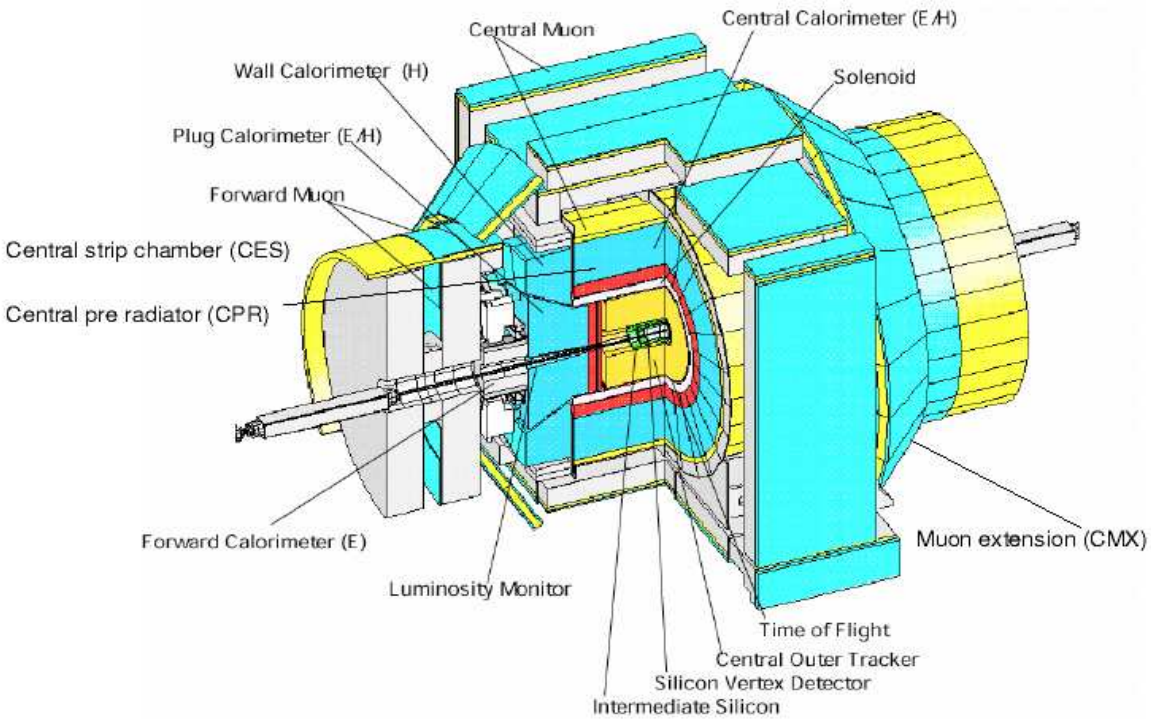

Figure 4.5: Schematic representation of the CDF detector.

4.4.1 Layer L00

Layer 00 is the innermost part of the tracking system for trajectory reconstruction. It provides a detection very close to the interaction point for the enhancement of impact parameter resolution, and it has a high resistance to radiation damage in order to withstand 7.4 fb^{-1} of data, with a signal-to-noise ratio of 8 after 5 Mrad of irradiation

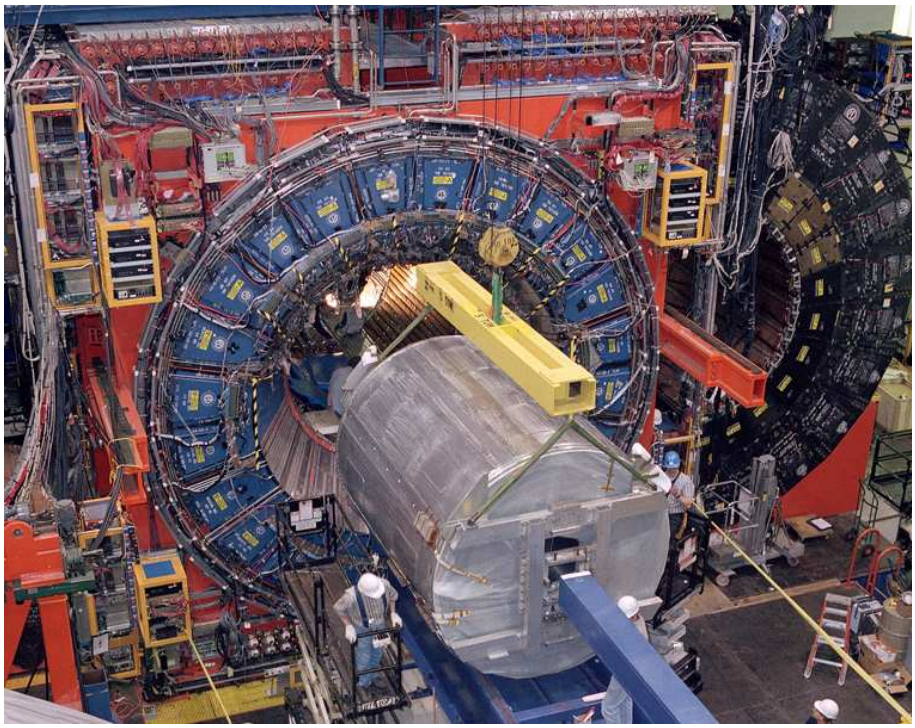

Figure 4.6: Insertion of the COT as part of the tracking volume inside the CDF detector.

corresponding to 5 fb^{-1} [37]. It is a single silicon layer at two radial coverages (1.35 cm and 1.65 cm) supported by a lightweight carbon structure to minimise the amount of material in the particle path. Fig. 4.7 (a) shows a cross section of the system with the layout of the sensor parts divided in ϕ in 6 narrow segments at the first radius and 6 wide segments at the other radius, for a total length of 95 cm along the $z-$axis. As for the other silicon detectors, the detection principle is based on the passage of particles through the depletion region between the p and the n electrodes where a resulting electric field is present [38]. The track creates charges (electrons and holes) that are collected at the electrodes and the axial position resolution per measurement is 6 μm. This is the first time that the L00 layer has been used in an analysis at CDF, and several checks concerning its impact on the data were performed during the analysis.

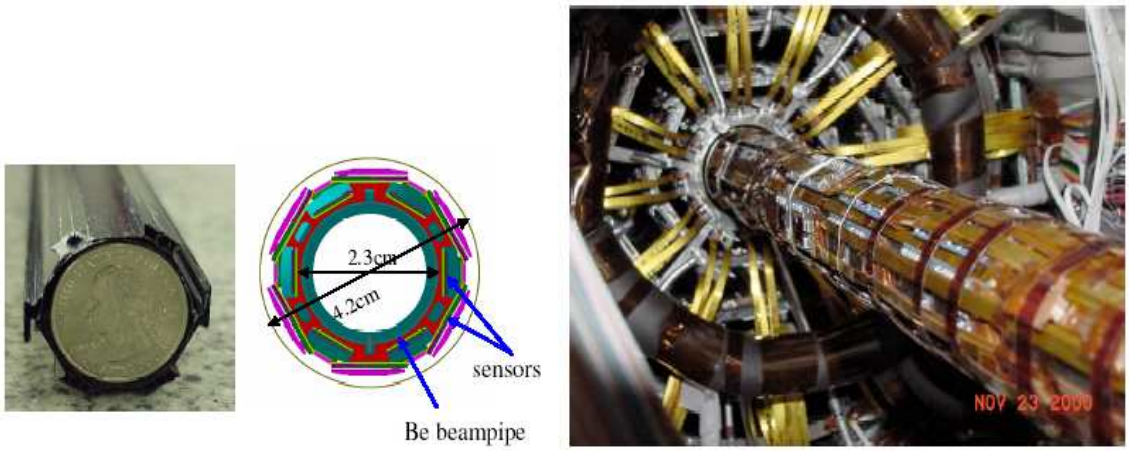

(a) (b)

Figure 4.7: Photographs of the Layer 00 (a), and SVX (b).

4.4.2 SVX and ISL

The second silicon system after the Layer 00, the Silicon Vertex detector II has a radial coverage from r =2.4 cm to r =10.7 cm. It consists of 5 layers of double sided silicon with a coverage $|\eta| < 2$ and a total length of 96 cm. The ϕ coverage is fragmented in 12 with three layers having a 0°-90° stereo and two with 1.2° small-angle stereo, providing $r - z$ readout for 3-D vertex reconstruction with an impact parameter resolution $\sigma_\phi < 30$ μm and $\sigma_z < 60$ μm [39].

Also part of the inner tracking volume of the detector, the Intermediate Silicon Layers represent the third silicon-based system after layer L00 and the SVX. It consists of two layers of double-sided silicon detectors [40] inside an overall structure of carbon with a length exceeding 3 meters and a maximum radius of about 35 cm allowing the entire device to be inserted inside the COT inner part space reserved for this effect. The silicon detectors are divided into five rings in the sensitive region, two placed at the radius r =28 cm from the beam pipe with its centre at $|z|$ =67.5 cm and 45 cm long, and two others located at the radius r =20 cm with the centre at $|z|$ =37.5 cm allowing the coverage $1 < |\eta| < 2$. To cover the region $|\eta| < 1$, a fifth module is placed at the radius r =22 cm with its centre at z =0 but with a length of 50 cm.

4.4.3 COT

The Central Outer Tracker (COT) is a 310 cm long cylindrical drift chamber along the z-axis and centered around the interaction point with a radius ranging from 43.4 cm to 132.3 cm. This permits the tracking of charged particles in the central pseudo-rapidity region ($|\eta| < 1$). The chamber is filled with 30240 gold plated tungsten anode wires of 40 μm diameter, parallel to the z-axis and immerged in an Argon Ethane medium of equal proportions.

4.4.4 Muon Chambers

The muon detectors are the most external parts of the detector. The amount of material that particles coming from the IP encounter before reaching the muon detector provides a filter as hadronic absorption to leave mostly muons interacting with the drift chambers and scintillator counters of the muon detector system. This material is provided by the other detector parts such as the calorimeter made of lead, or 60 cm of steel wall for the CMP system located laterally to the detector.

The muon system is divided in several parts. The Central Muon Detector (CMU) covers the region $|\eta| \leq \sim 0.6$ [39] with cells containing 50μm stainless steel wires. The wires measure the ϕ and z positions of the muons with a minumum detectable p_T of 1.4 GeV/c. The Central Muon Upgrade (CMP) covers a region $|\eta| \leq \sim 0.6$, and have scintillator counters in addition to the drift tubes. Trigger hits are formed from coincidences of nearby wires that are used in association with trigger information from the CMU chambers, and the threshold of detection is 2.2 GeV/c. The Central Muon Extension (CMX) (cf. Fig. 4.5) with the coverage $\sim 0.6 \leq |\eta| \leq \sim 1.0$, also consists on the association of drift chamber and scintillator, forming a conical surface.

4.4.5 Reconstruction

The reconstruction procedure uses the "BcFind" program. It searches for two oppositely charged muons in the event, with each muon track satisfying a restriction $\chi^2 < 9$. If the vertex fit converges and the mass is within 80 MeV/c^2 around the J/ψ mass, a second vertex fit is tried where a third track (3-D vertex) is attached to the two muons, with the invariant mass of the muon pair constrained to the PDG value of the J/ψ mass. A distance cut $\Delta z < 5$ cm is applied between the two muons and between the reconstructed J/ψ and the third track. A restriction on the 3-D vertex is applied with a cut $\chi^2 < 50$.

The determination of the primary vertex position can be done by two methods. The standard method uses the triggered tracks to retrieve the position of the vertex.

Another method, the "track–fitted primary vertexing" technique [41], also referred as event by event primary vertex (EbE), uses the tracks in each event to measure the position of the primary vertex, excluding the ones belonging to the candidate and those that do not pass some quality cuts. These tracks are provided to the vertex fitting routine, together with a beam constraint. The resulting position of the primary vertex is then subtracted from the candidate vertex to calculate its decay length and its lifetime.

4.4.6 Monte Carlo

The analysis makes an extensive use of the Monte Carlo simulation of the decay and its characteristics, based on the available data and theoretical models. It is particularly important for the purpose of the cuts optimisation. To realistically reproduce the events, the Monte Carlo includes the full detector simulation.

The Monte Carlo code principally used, named BGENERATOR [42], [43] with the EVTGEN [44] decayer to generate the final state, can simulate $B^{\pm}$ and B_c decays.

The $B^{\pm}$ signal Monte Carlo sample is generated using the meson p_T spectrum derived from the CDF J/ψ analysis [45]. The B_c signal Monte Carlo sample is based on two p_T distributions, one (C) derived from Chang *et al.* [46], and chosen as reference p_T spectrum for the cut optimisation, while the other (B) is derived from Berezhnoy *et al.* [47], with an harder spectrum (Fig. 4.8) and used to evaluate systematic effects. For both samples, the p_T distributions start from $p_T = 0$, and an interval rapidity $|y| < 1.3$ is used for all samples.

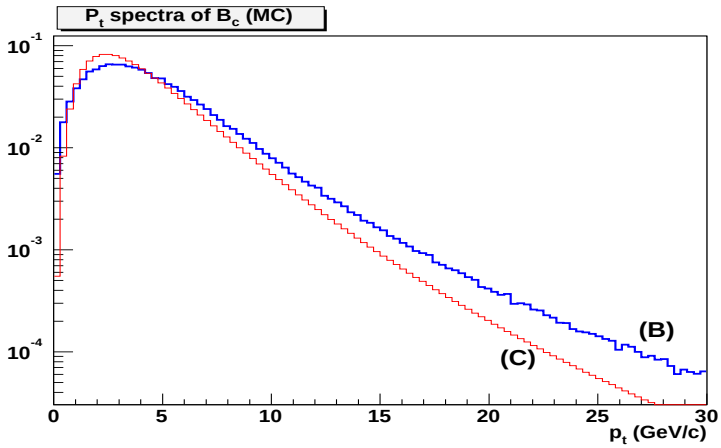

Figure 4.8: Comparison of Monte Carlo p_T spectra used for B_c (C) and (B). The spectrum (C) is the reference for this analysis. (B) is slightly harder.

The B_c Monte Carlo sample predominantly used for the analysis assumes a mass of 6.4 GeV/c^2 and a lifetime of $c\tau = 138\mu$m. For the evaluation of the variation of sensitivity of the analysis, other Monte Carlo samples with different lifetimes and mass values in the limit of the known uncertainties are also used. To simulate physical backgrounds due to other B_c decays (e.g. semileptonic), some additional Monte Carlo samples are generated using BGENERATOR with full reconstruction.

For studies where the EbE technique is used, since the primary vertex is calculated using other tracks than the $J\psi$ π candidates, the BGENERATOR Monte Carlo can not be used. A PYTHIA [48] Monte Carlo is employed instead, for its ability to simulate underlying events. Only events with a B_c candidate are selected and all the B_c mesons

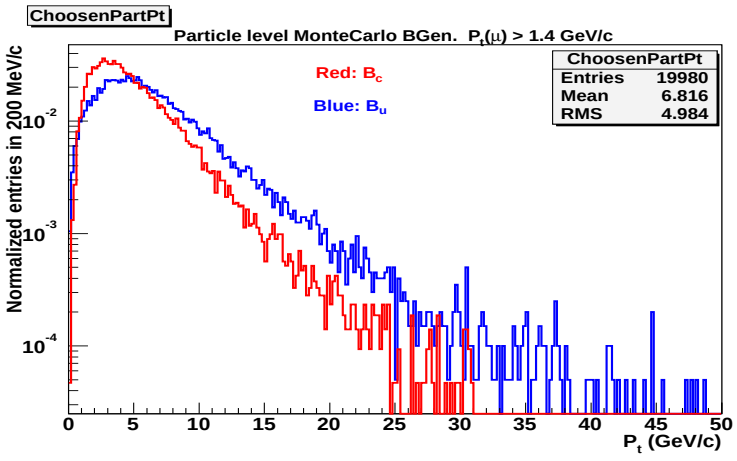

Figure 4.9: Comparison of Monte Carlo p_T spectra used for B_c (C) and the one used for B_u. The B_c spectrum is considerably softer.

are decaying to the signal mode. This Monte Carlo sample has a different p_T spectrum and has a B_c mass set at 6.6 GeV/c^2, since it is the default mass value provided by PYTHIA.

4.5 Cuts Optimisation

The cut optimisation stage aims to evaluate the best selection requirements on quantities so as to maximise the predominance of a possible signal over the background. An analytical discriminating function and Monte Carlo/Data information are used for this purpose.

4.5.1 The Optimisation Function

The determination of the predominance of an eventual signal over a background is a key parameter in this search. It is of primary importance since the blind restriction does not allow to look directly at the consequence of a cut on the mass spectrum; so another method is needed to evaluate the impact of a cut systematically. As a *significance* formula, it is usual to see variations of the ratio:

$$\frac{S}{\sqrt{B}},$$

where S is the signal contribution and B, the background events. For this analysis, the following function Σ is used to *optimise* the cuts:

$$\Sigma = \frac{S}{1.5 + \sqrt{B}},$$

where S is the expected number of events for the signal and B is the number of background events in the same mass region used to determine S. For cases where the signal location is known, such as for the $B^{\pm}$ decay, it is straightforward to define a selection region around the signal as a $\pm 2\sigma$ band centered on the mass with the σ determined by the fit of the peak, and consequently to obtain the number of signal events in this region. Similarly, the background in sidebands can be fitted, interpolated to its contribution under the signal peak, and a significance, which relates to how well the signal stands out above the background, can be evaluated with $\frac{S}{\sqrt{B}}$. It is natural to see with this form how a signal S compares to a Gaussian fluctuation of

a background $\sqrt{B}$, and this is equivalent to evaluating the probability that a fluctuation would look like a signal. This discussion for the $B^{\pm}$ decay need only to involve the data.

This present analysis is different since it aims at finding the location of a mass peak, thus an unknown quantity. The fraction of the data that corresponds to the signal, if present, is not known. The optimisation function Σ used here is a search formula designed to give the optimal cut on a quantity with a condition on the desired degree of background rejection as parameter, for instance 3σ of a single tail Gaussian distribution. G. Punzi describes a method in [49] which aims to achieve this goal.

In a counting experiment, the repartition of the events follows a Poisson distribution that can be approximated with a Gaussian. Fig. 4.10 shows a comparison of a distribution of pure background events B with a distribution of B background events plus S signal events on average. Despite of the Gaussian approximation, the spread of the distribution is essentially governed by the Poisson fluctuation $\sqrt{B}$ for the pure background, and $\sqrt{B+S}$ for the other distribution. Intuitively, searching for a function that optimises a cut to select signal over background relates to how distinct these two distributions are from each other. Clearly this depends on the signal S size. With a small signal, there is an overlapping of the two distributions and a region β of the $B+S$ distribution can extend under the pure background one. The problem finally consists of the definition of boundaries to determine whether a particular case belongs to the B distribution or to the $B+S$ distribution, according to these defined boundaries. For instance a choice can be made to accept that the background only extends to a times its fluctuation. As a consequence, any fluctuation after $B + a \times \sqrt{B}$ cannot represent a background characteristic. Similarly, a choice can be made that a $B+S$ distribution extends from a mean value $B+S$ only b times its fluctuation $\sqrt{B+S}$, i.e. down to $(B+S) - b \times \sqrt{B+S}$. To make a clear

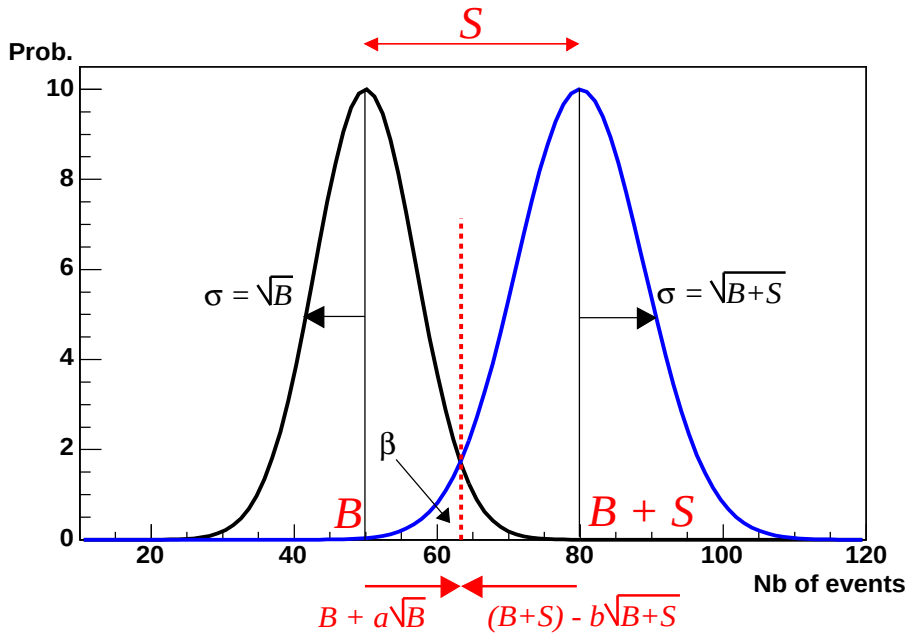

Figure 4.10: Distributions of probability of observation given the number of background events with the mean value B, and background plus signal events with the mean $B + S$ in a counting experiment. The Poisson distributions are approximated to a Gaussian shape.

separation, a harmonisation is needed such that:

$$B + a \times \sqrt{B} = (B + S) - b \times \sqrt{B + S}.$$

G. Punzi proposes that the β region satisfies the following [49]:

$$1 - \beta > CL$$

where CL is the confidence level. This is equivalent to say that the power of the chosen requirements on a and b allows to identify a $B + S$ distribution, thus a signal presence, and rules out a pure background case with a degree of confidence above CL. The size of the signal present has clearly an incidence on the choice and relates to the confidence level with a minimum number of signal events S_{min} to satisfy the last relation. Consequently the confidence level is incorporated when:

$$B + a \times \sqrt{B} = (B + S_{min}) - b \times \sqrt{B + S_{min}}$$

which is solved in [49] and leads to the following requirement for S_{min}:

$$S_{min} \geq \frac{b^2}{2} + a\sqrt{B} + \frac{b}{2}\sqrt{b^2 + 4a\sqrt{B} + 4B}$$

[49] concludes that in the particular case where the choice $a = b$ is made, the maximum sensitivity is reached when the following expression is maximised:

$$\frac{\epsilon}{a/2 + \sqrt{B}}$$

where ϵ is the efficiency of the cut on the signal (the efficiency relates to the signal S since the expected value of S is $S = \epsilon \cdot L \cdot \sigma_{xec}$ where σ_{xsec} is the associated cross section and L the integrated luminosity). Since a (or b) are the number of σ corresponding to one-sided Gaussian, a background rejection at the 3σ level corresponds to $a = 3$, which leads to the 1.5 term.

4.5.2 Optimisation Procedure with Various Samples

Depending on whether the optimisation is performed using the $B^{\pm}$ decay or the B_c decay, the procedure for the use of the optimisation function Σ is different. For certain variables related to the detector capacity, such as a 3-D vertex χ^2 which is a measure of the accuracy of the fit to the reconstructed vertex, the result does not depend on the decay studied. Consequently the control decay $B^{\pm}$ can be used for the optimisation of the χ^2 cut. The location of the signal for the decay is well known and not in a blind region, so that S and B can be directly obtained from the data sample. An optimisation routine is created and applies a cut on the data sample by an iterative procedure. A fit is performed on the resulting distribution at each iteration, to calculate a Σ score as a function of the cut value, and search for its maximum. A typical example shown in Fig. 4.11 illustrates the principle, with a histogram constructed from a linear background

$$ax + b,$$

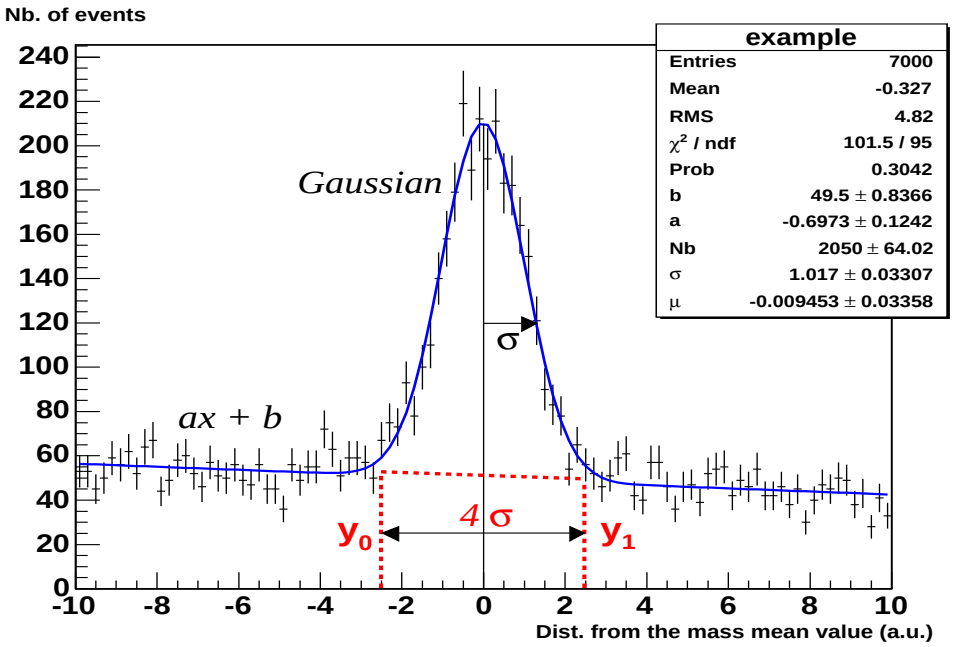

Figure 4.11: Example of the procedure for an optimisation using a data sample. A cut is applied on a variable and the resulting mass distribution with a signal and background is fitted. This method is applied when optimising a cut variable on a $B^{\pm}$ sample with the signal taken from the data.

and a Gaussian signal

$$\frac{N \cdot \omega}{\sigma\sqrt{2\pi}} exp(-1/2 \cdot (\frac{x-\mu}{\sigma})^2).$$

For the i^{th} iterative fit, the number of signal events N_i, the σ_i of the Gaussian, the mean value μ_i of the distribution and the linear parameters a_i and b_i are extracted with their associated uncertainties. While N_i immediately provides S_i for the optimisation function Σ_i, the associated background B_i for the $4\sigma_i$ signal region considered is obtained with the following relation:

$$B_i = \frac{1/2 \cdot (y_{0,i} + y_{1,i}) \cdot 4\sigma_i}{\omega},$$

where the values of $y_{0,i}$ and $y_{1,i}$ indicated in Fig. 4.11 are obtained from the a_i, b_i parameters, and ω is the bin width of the histogram. For each iteration, the signal size and the background level, both normalised to 4σ, change with the new value of

the applied cut, and a corresponding Σ_i score is obtained:

$$\Sigma_i = \frac{S_i}{1.5 + \sqrt{B_i}}.$$

For an optimisation using the signal from a Monte Carlo sample, the signal distribution is fitted with a Gaussian, and the three parameters S, σ and μ are obtained from the fit. A unique Gaussian function without any background is used most of the time, since the BGENERATOR Monte Carlo contains only information about the B decay. With the PYTHIA Monte Carlo however, the other tracks in the event are also generated.

For an optimisation performed with a $B^{\pm}$ Monte Carlo, it is verified that the mean of the signal μ (the value of the mass) is consistent with the mean provided by the data. The σ obtained from the fit to the Monte Carlo signal is used to define a background population on the data sample based on the μ, as shown in Fig. 4.12. The background is taken from the sideband regions between 4σ and 6σ away from the mean. Contributions from below and above the peak are combined to form a 4σ background population. This provides a good background evaluation without signal events.

For an optimisation using a B_c decay sample, the fit on the Gaussian Monte Carlo signal also provides S, σ and μ. The background B is however calculated differently. The σ value obtained from the signal fit allows us to define a 4σ region in the 1600 MeV/c^2 wide blind region with N_{blind} total events. The background B is estimated with:

$$B = \frac{4\sigma}{1600} \cdot N_{blind}.$$

In both cases, the optimisation procedure consists on obtaining a set of S and B from fitting the resulting distribution due to the cut action, and identify a cut value that maximises the Σ function.

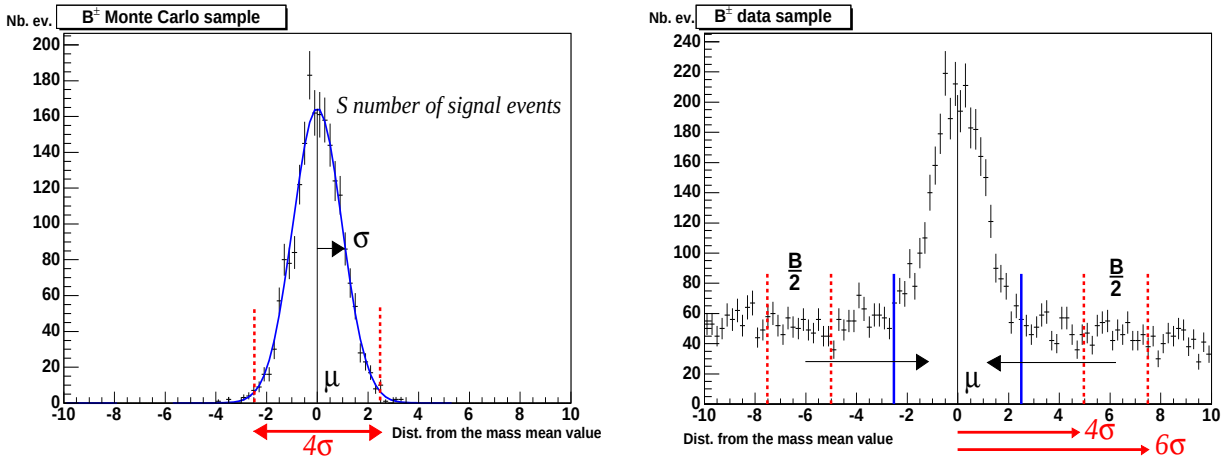

(a) (b)

Figure 4.12: In the case of an optimisation using the control sample and the signal provided by Monte Carlo, a fit of the Monte Carlo signal (a) to obtain S also allows to define sidebands on the data sample (b) for the definition of B.

4.5.3 Selection of the Cut Variables

Three types of variables can be distinguished to select the B_c candidates: those whose distributions are reproduced by the Monte Carlo, those that are not well reproduced, and those that depend on unknown parameters. For the first category, an optimisation using a signal simulated from Monte Carlo can be safely used; for the second the control sample ($B^{\pm}$) has to be used. Cutting directly on the third type of variable should be avoided, but if this not possible, it is necessary to use a Monte Carlo sample based on the central value of the unknown quantity. In that case, the experimental 1-σ uncertainty on the value serves to estimate the effect of the cut in the worst and best case scenarios.

The Monte Carlo validation showed that the projected decay length (L_{xy}), the impact parameter of the B-meson ($d_0(B)$) and the collinearity angle ($d_0(B)/L_{xy}$) are all well reproduced by simulation. On the other hand, the distribution of χ^2 of the vertex fit was shown not to be reproduced correctly by the Monte Carlo, and consequently, the value has to be extracted from the control sample data.

The transverse momentum p_T of the B_c meson depends on the production and fragmentation models, therefore several Monte Carlo samples were produced to assess the systematic uncertainty on the expected events. The transverse momentum of the pion depends on the mass of the B_c. Any cut on L_{xy}, ct or a track impact parameter depends strongly on the lifetime, so these cuts, although powerful discriminants against background, have to be used with care. In order to reject the prompt background without knowing precisely the lifetime of the B_c, the significance of the projected decay length in terms of its uncertainty σL_{xy} can be used instead. There are some technical developments that affect this variable such as the use of L00 hits, and the use of track-fitted primary vertex. In particular, the more precise knowledge of the $z-$position of the vertex allows us to use a 3-D angle between the candidate momentum and the direction of flight.

4.5.4 Optimisation of Cuts Individually Using $B^{\pm}$ Samples

$B^{\pm}$ χ^2

The χ^2 of the vertex fit determines if the candidates can be considered. A high value would indicate a likely error in the tracking or in the multi-track association at the vertex. The highest possible background rejection produced by a cut, i.e. the maximum Σ value obtained during the optimisation, is naturally the property desired here; however the rejection of *signal* is also a concern. The fraction of signal lost is the efficiency of a cut, and it can be easily evaluated with the Monte Carlo sample by comparing the number of events in the sample after the cut with respect to the initial number. Fig. 4.13 shows for instance that for the optimisation on $B^{\pm}$ χ^2, a cut at 22 retains 90% of the Monte Carlo sample. Fig. 4.14 shows the result of two cases of the cut optimisation method, one employing the $B^{\pm}$ signal from data (a), and the other using the signal from Monte Carlo (b). The disagreement is the consequence of the poor reproducability of 3-D χ^2 with Monte Carlo, and the optimisation cannot be

done with the Monte Carlo signal. The quality of the vertex fit from tracks is however independent of the decay channel studied, whether the signal comes from two muons associated with a $K^{\pm}$ third track originated by a $B^{\pm}$, or with a $\pi^{\pm}$ third track from a B_c. Therefore, the sensitivity test for the B_c χ^2 from data should be similar to the one for the $B^{\pm}$ shown in Fig. 4.14 (a).

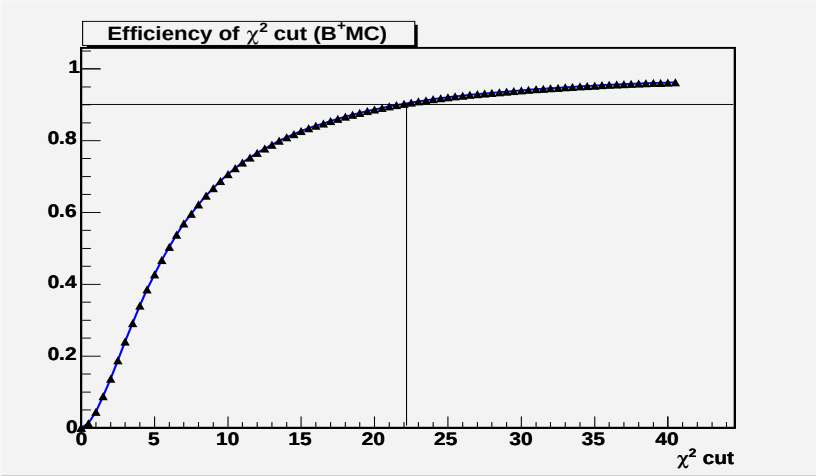

Figure 4.13: Efficiency of χ^2 cut, i.e. fraction of $B^{\pm}$ Monte Carlo candidates retained.

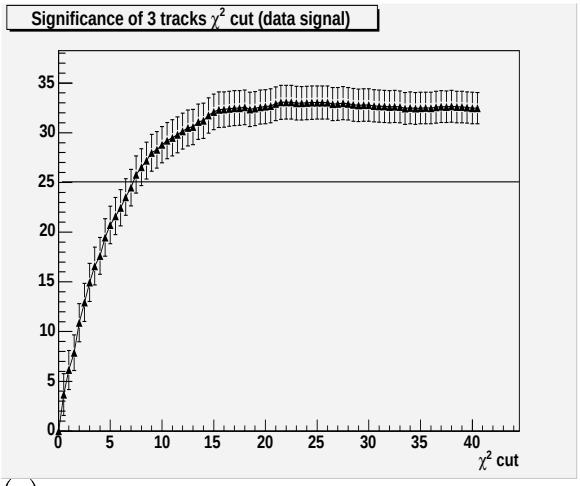

(a)

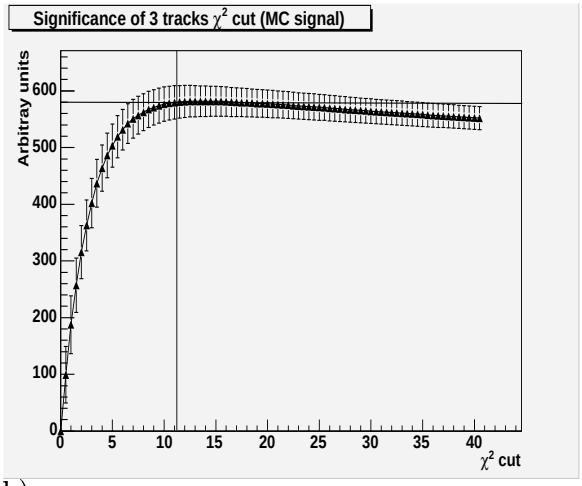

(b)

Figure 4.14: Sensitivity Σ as a function of a cut on the χ^2 of the vertex fit using signal from data (a), and from Monte Carlo (b). The asymptotic value of Σ, when no cut is applied, is indicated for the case of the data. The $y-$axis cannot be compared since the calculation of Σ is done with different signal samples in both cases.

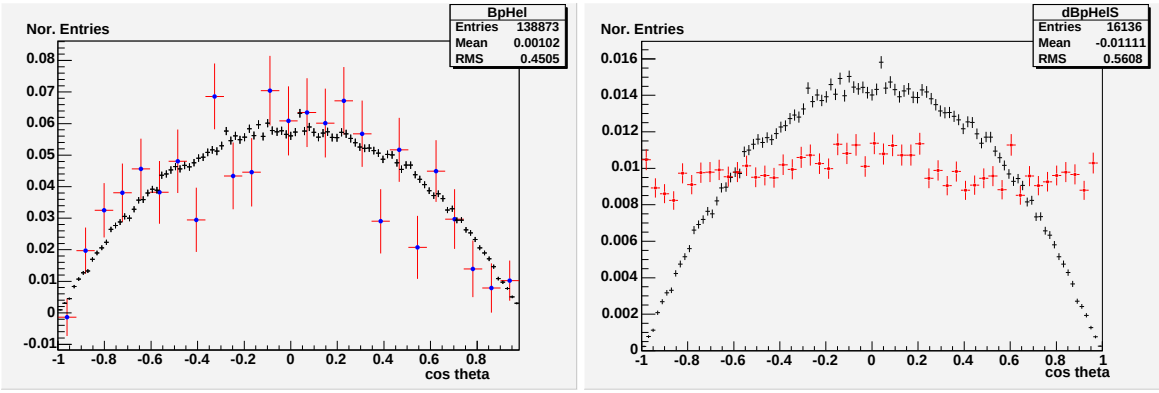

(a) (b)

Figure 4.15: (a) Helicity corresponding to the J/ψ region (the most numerous points are from the Monte Carlo). (b) Helicity from outside the J/ψ peak compared with the signal-only Monte Carlo distribution (same as in (a)).

J/ψ-μ Helicity

The helicity angle θ_h of the J/ψ is defined as the angle between the positive muon and the direction of flight of the B-meson in the rest frame of the J/ψ. In the decay $J/\psi \rightarrow \mu^+\mu^-$, this angle is distributed as $1 - \cos^2\theta_h$. Fig. 4.15 (a) using the $B^{\pm}$ control sample, shows that the Monte Carlo reproduces well the expected distribution whereas the flat background distribution in $\cos\theta_h$ is in clear contrast to that of the J/ψ region. An optimal cut of $|\cos\theta_h| < 0.9$ is found, removing only 1% of the Monte Carlo signal sample.

4.5.5 Effect of Individual Cuts on B_c Samples.

The investigations are now done using the B_c Monte Carlo as the signal sample, and the data in the search region as background. A set of cuts is applied while performing studies, as a preliminary selection requirement. They are muons $\chi^2 < 8$, dimuon mass within 55 MeV/c^2 of the nominal J/ψ mass, and J/ψ helicity < 0.9.

Comparison of Different Theoretical $p_T(B_c)$ Spectra.

Although there is no experimental knowledge of the $p_T(B_c)$ spectrum, several Monte Carlo samples for the B_c signal are available, based on theoretical models with different p_T spectra. An optimal cut on the p_T is investigated with a signal from Monte Carlo using two theoretical spectra. Fig. 4.16 shows the sensitivity of the cut on the p_T with one associated efficiency, for two spectra models. Fig. 4.8 showed that the two p_T distributions are similar, and consequently the optimisation curve has the same behavior. No maximum corresponding to an optimal cut value in $p_T(B_c)$ is found, in agreement with the small difference between the p_T distribution from Monte Carlo (signal) and data (assumed to be mainly background).

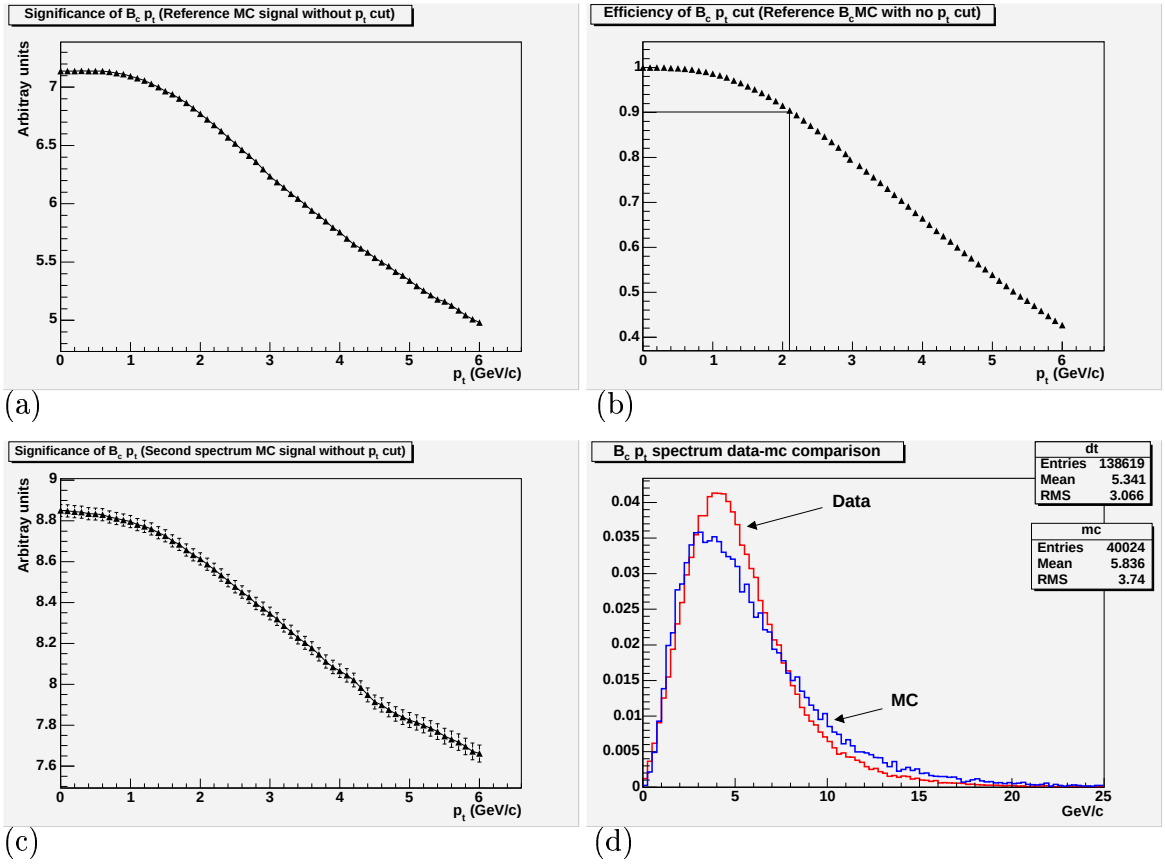

Figure 4.16: Evaluation of Σ as function of p_T cut for the (C) spectrum (a), with corresponding efficiency (b); Σ for the (B) spectrum (c); Signal (Monte Carlo) - Background (Data) comparison for the (C) $p_T(B_c)$ spectrum.

Pion p_T

The third track of the decay, the π, can potentially provide a powerful background rejection. Since it depends on the B_c mass, the p_T spectrum of a decay π should be characteristic and somewhat different from that of pions with other origins. This is shown in Fig. 4.17 (a) where the data (essentially background) has a softer component than the predicted Monte Carlo model. Consequently, the optimisation reveals a clear peak (Fig. 4.17 (b)) and a cut value for the $p_T(\pi)$ variable. Since the maximum happens over a broad p_T window, an adequate cut value is determined from the efficiency response (Fig. 4.17 (c)). A cut at $p_T(\pi) > 1.6$ GeV/c^2 could be preferable to $p_T(\pi) > 2$ GeV/c^2, since the number of candidates predicted from the Monte Carlo changes dramatically while the sensitivity is less affected.

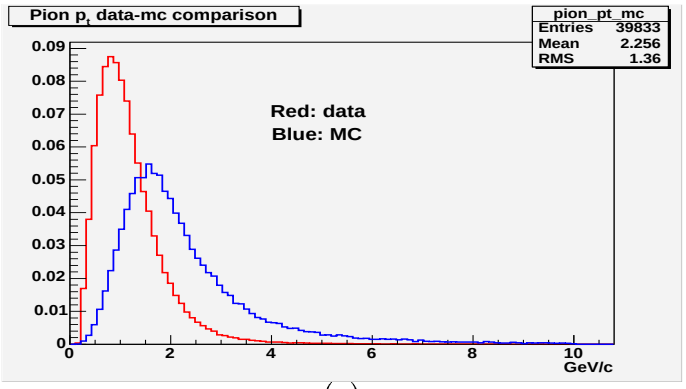

(a)

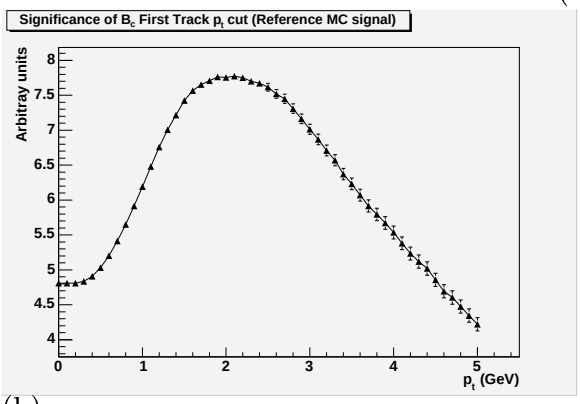

(b)

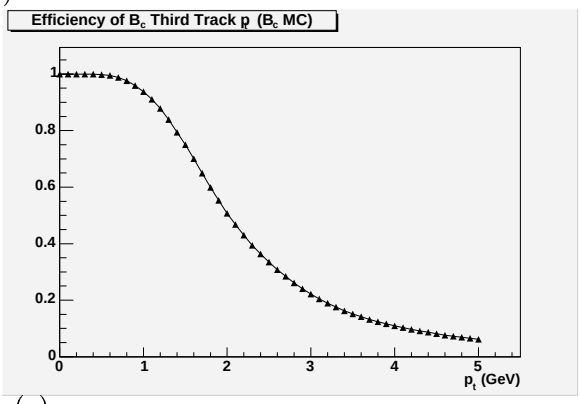

(c)

Figure 4.17: (a) Signal (Monte Carlo with M(B_c)= 6.4 GeV/c^2) - Background (Data) comparison as a function of p_T of the charged pion; (b) sensitivity and (c) detection efficiency varying the cut on this quantity.

Projected decay length L_{xy}

The lifetime of the B_c meson could in principle be advantageously used for background rejection. The projected decay length on the transverse plane, denoted L_{xy}, is investigated for an optimal cut as shown in Fig. 4.18 (a). This is not however an ideal variable, because the lifetime of the B_c is not precisely known. Since it includes the errors on the reconstructed L_{xy}, the use of the significance of the measured L_{xy} variable instead ($L_{xy}/\sigma(L_{xy})$) could allow a better discrimination of poorly measured prompt events with a certain potential of background rejection (Fig. 4.18 (b)). This cut is optimised in a later section.

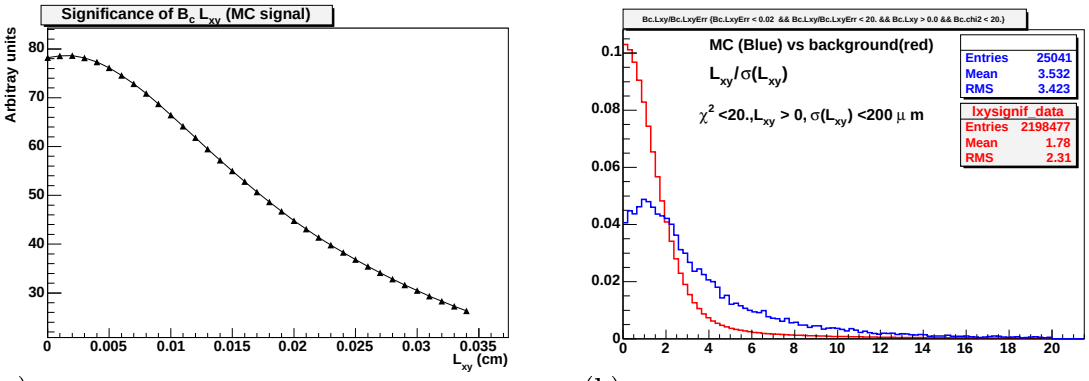

(a) (b)

Figure 4.18: Optimisation of the L_{xy} variable (a), and comparison of the distribution of $L_{xy}/\sigma(L_{xy})$ for signal (Monte Carlo) and background (data). The distributions are normalised for the comparison, and the Monte Carlo has the broadest repartition.

Distance Traveled During the Meson Lifetime ct

The value of the lifetime for each B_c candidate is calculated from the L_{xy} value, and Fig. 4.19 (a) shows a comparison between the predicted signal from Monte Carlo and the background. A component of the background has a longer lifetime than the B_c meson (e.g. due to other B mesons), also a difference appears after 600 μm. At this distance however, this represents only a small population of events and does not reflect in a significant gain in sensitivity, as shown in Fig. 4.19 (b) for the optimisation curve on an upper cut on ct.

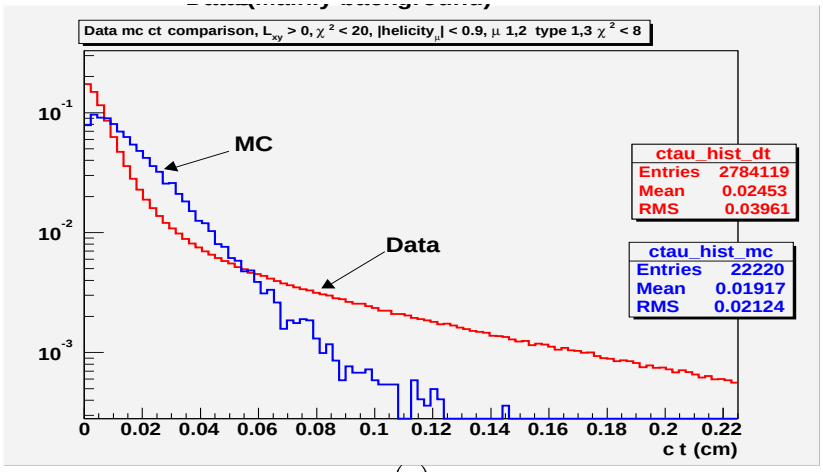

(a)

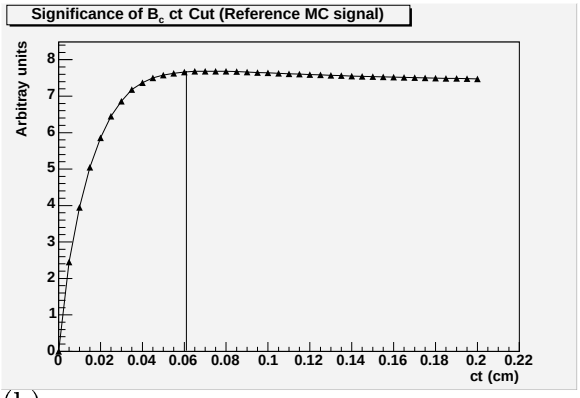

(b)

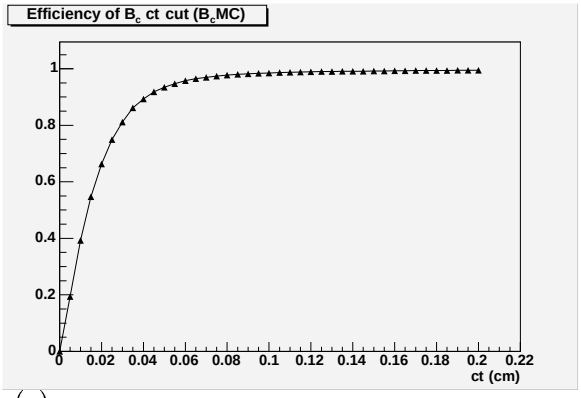

(c)

Figure 4.19: (a) Signal (Monte Carlo) - Background (Data) comparison as a function of lifetime ct of the B_c candidate; (b) sensitivity and (c) detection efficiency varying the cut on this quantity.

B_c Impact Parameter (d_0)

The impact parameter d_0 of the B_c is potentially useful in discriminating against combinatorial background. It is the distance of the reconstructed three track combination with respect to the primary vertex, measured in the xy plane. Genuine signal events should point accurately toward the primary event vertex with a small d_0, while partially reconstructed decays are more likely to have a momentum imbalance that would shift the reconstructed momentum vector away from the measured direction of flight. A random association between a J/ψ and a pion not originated from the searched decay would likewise not have a strong pointing characteristic. Fig. 4.20

shows this with a narrower distribution of the predicted signal from Monte Carlo in comparison with the background. The collinearity angle (d_0/L_{xy}) of the B_c also gives a pointing information that makes use both of L_{xy} and d_0. For the signal events, this angle is peaked to 0, and shows a discriminating potential (cf. Fig 4.21).

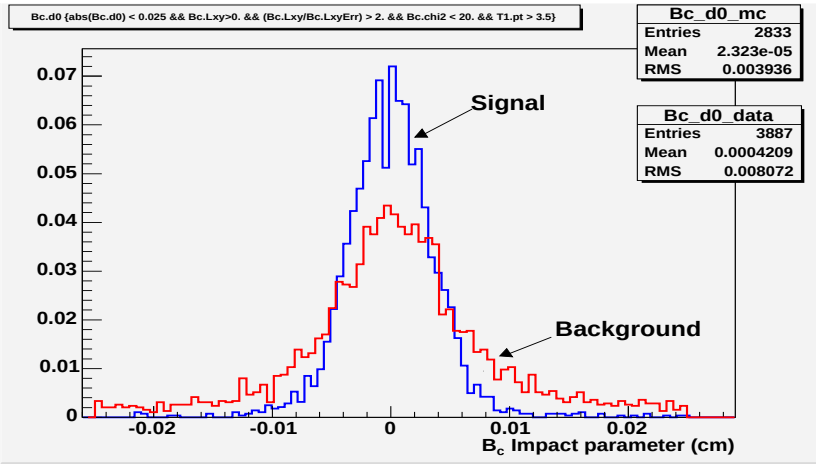

Figure 4.20: Impact parameter distribution from data (assumed as B_c background) and from the B_c Monte Carlo sample.

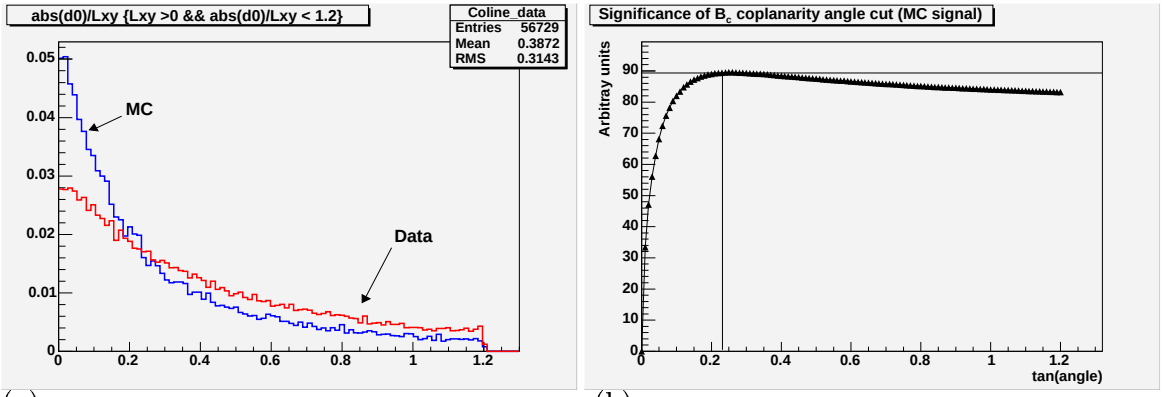

(a) (b)

Figure 4.21: Signal (Monte Carlo) - Background (Data) comparison for the B_c collinearity angle (a), and optimisation on a d_0/L_{xy} cut.

4.5.6 Grid Optimisation Procedure for B_c

The interaction between the cuts is a concern of this study. Each optimisation was performed so far independently on one quantity at a time, with sometimes the application of other fixed cuts during the procedure. There is however a need to understand mutual effects of cuts when several are simultaneously active, for stability purposes. The previous optimisations indicated ranges of values that can serve for a grid method. This is performed using the same technique as for individual cuts, but with the logic of a series of nested loops. A grid of three cut variables is set up so that values range as follow:

1. Collinearity angle = $0.11 + i \times 0.02$; i=0,9
2. $p_T(\pi) = 2. + j \times 0.2$; j=0,9
3. $p_T(B_c) = 8. + k \times 1$; k=0,9

Each set of indices (i,j,k) is sorted in a array of triplet elements represented by an integer l ranging from 0 to 999, such that

$$\begin{aligned} l_0 = \quad & 0 \quad && = (i_0, j_0, k_0) && = (0,0,0) \\ l_1 = \quad & 1 \quad && = (i_0, j_0, k_1) && = (0,0,1) \\ l_2 = \quad & 2 \quad && = (i_0, j_0, k_2) && = (0,0,2) \\ \vdots \quad & \vdots \quad && \vdots && \vdots \\ l_{999} = \quad & 999 \quad && = (i_9, j_9, k_9) && = (9,9,9) \end{aligned}$$

This allows the graphical representation of a maximally significant occurrence, and the identification of the corresponding triplet, thereby giving the potentially optimal cuts. This is illustrated in Fig. 4.22, which shows the search for a maximum Σ value, and the Monte Carlo efficiency is shown in Fig. 4.23 . In particular, it is investigated if there could be an optimal value in $p_T(B_c)$ revealed in the context of a grid method. The $x-$axis represents the l index, while the $y-$axis gives the corresponding sensitivity in arbitrary units. The choice of these three quantities is motivated by the broad range

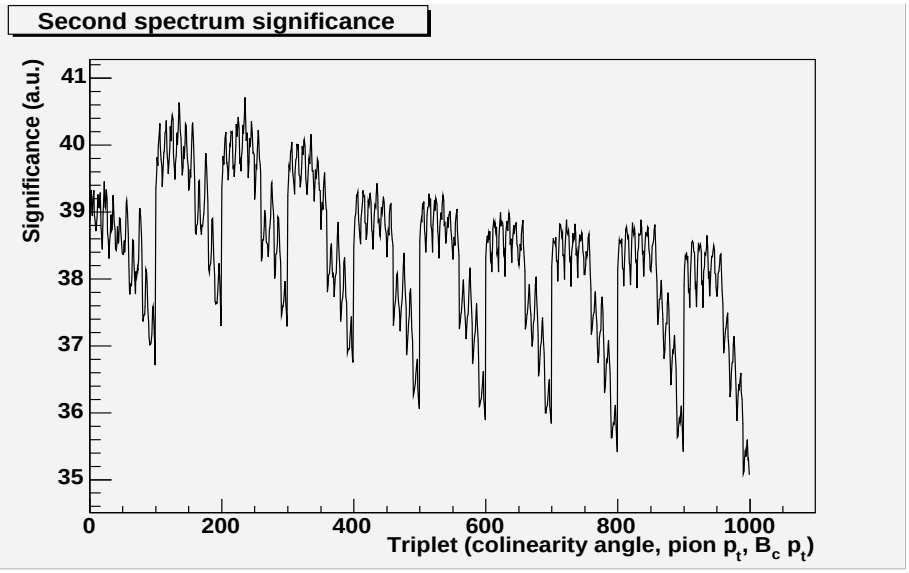

Figure 4.22: Grid optimisation sensitivity.

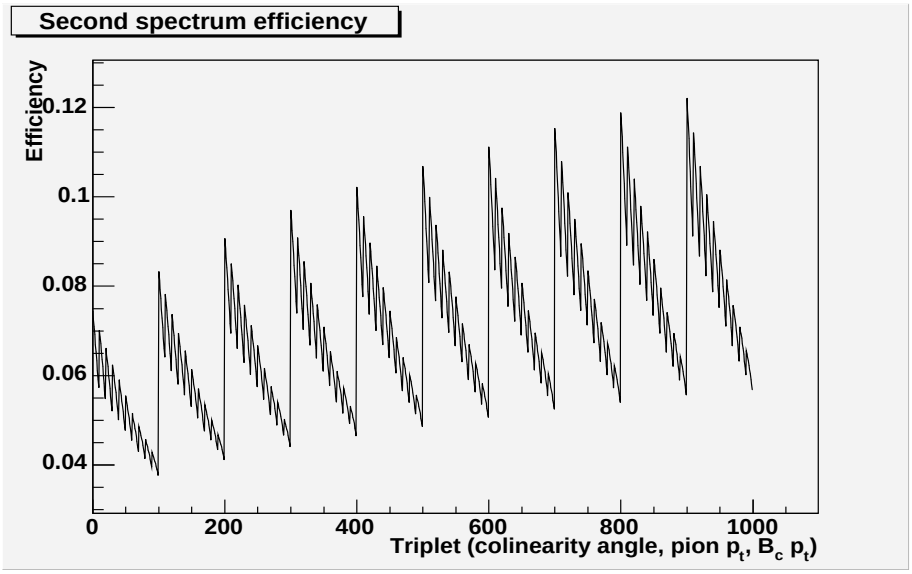

Figure 4.23: Grid optimisation resulting efficiency.

of parameters covered (d_0, L_{xy}, p_T). During the grid study, the cuts B_c $\chi^2 < 20$, $L_{xy} > 0$, abs(helicity) < 0.9, and muon $\chi^2 < 8$ are applied. These are not very restrictive cuts, and merely provide a slightly cleaner sample. The pattern of the oscillations seen are due to the chosen logical sequence of the loops. For the example shown, the scan on the collinearity angle cut drives the main oscillations. The amplitude of the oscillations is an indication of the background rejection power for a cut variable, and

Quantity	No χ^2 cut	$\chi^2 < 20$	$p_T(B_c)$ 2	$p_T(B_c)$ 3
Collinearity angle	0.13	0.16	0.13	0.12
Pion p_T(GeV/c)	3.2	3.6	3.6	4.1
B_c p_T(GeV/c)	8.0	8.0	7.5	9.25

Table 4.2: Optimised values of some of the more important kinematic parameters using the grid procedure. Three different $p_T(B_c)$ spectra are used, with a restriction on the χ^2 for the first one.

the $p_T(\pi)$ has a more dramatic effect than the pointing cut. The resulting following values maximize the Σ function:

1. Collinearity angle = 0.12
2. π p_t = 4.1 GeV/c
3. B_c p_t = 9.25 GeV/c

with a corresponding efficiency of 6.7 % of the initial Monte Carlo signal sample remaining after the cuts.

Several grid studies are performed with different quantities, conditions and ranges, and some results are given in Table 4.2. The values for the optimised cut quantities are similar, providing confidence that the cuts are stable and insensitive to the details of the dynamical model and the vertexing. However, the values found have a high magnitude which results in a poor efficiency; in particular, the application of a $p_T(B_c) > 8$ GeV/c cut on the distribution shown in Fig. 4.16 would lead to the removal of most of the predicted signal. Consequently, the analysis does not use any cut on the candidate transverse momentum.

4.5.7 Sequential Optimisation with B_c Samples: the "N-1" Method

The optimisation studies of variables performed independently are useful to estimate the effects of different cuts, and to determine their potential power of background removal. A grid optimisation method using a matrix based algorithm is also useful to verify the stability of the cuts. For the final determination of the cuts used in the analysis, the most suitable method for the optimisation stage is a sequential iterating technique ("n-1" method) where the cuts are optimised one after the other, using and applying the obtained previous cut values.

To evaluate realistically the possibility of the observation of a signal, the sensitivity Σ is now calculated using the ratio of the two Monte Carlo physics sample efficiencies $(B^{\pm}, B_c)$. This optimisation makes thus the use of the control sample, with the number of $B^{\pm}$ signal events $N_{B^{\pm}}$ when a cut is applied, and the relative fraction between the two decays R introduced in the section of expected B_c signal events. The function Σ is calculated with:

$$\Sigma = \frac{\frac{\epsilon_c}{\epsilon_u} \times N_{B^{\pm}} \times R}{1.5 + \sqrt{B}}$$

Some requirements on silicon hits are also applied; every track used should be fitted with a hit on at least one of the layers L0 or L00. This removes a significant fraction of the signal, but at the same time a very large fraction of the background since it increases the vertexing precision.

Starting from the initial values tabulated in Table 4.3, the cuts are optimised in turn, as shown in Fig. 4.24. Because of the silicon hits requirements and the presence of other cuts, an optimisation on L_{xy} is investigated. A set of optimal values is found and indicated on the right column of the table. The most important cuts in terms of efficiency reduction and background rejection are L_{xy} and the $p_T(\pi)$, illustrated by their clearly peaked distributions in Fig. 4.24. The $p_T(\pi)$ restriction indicates that

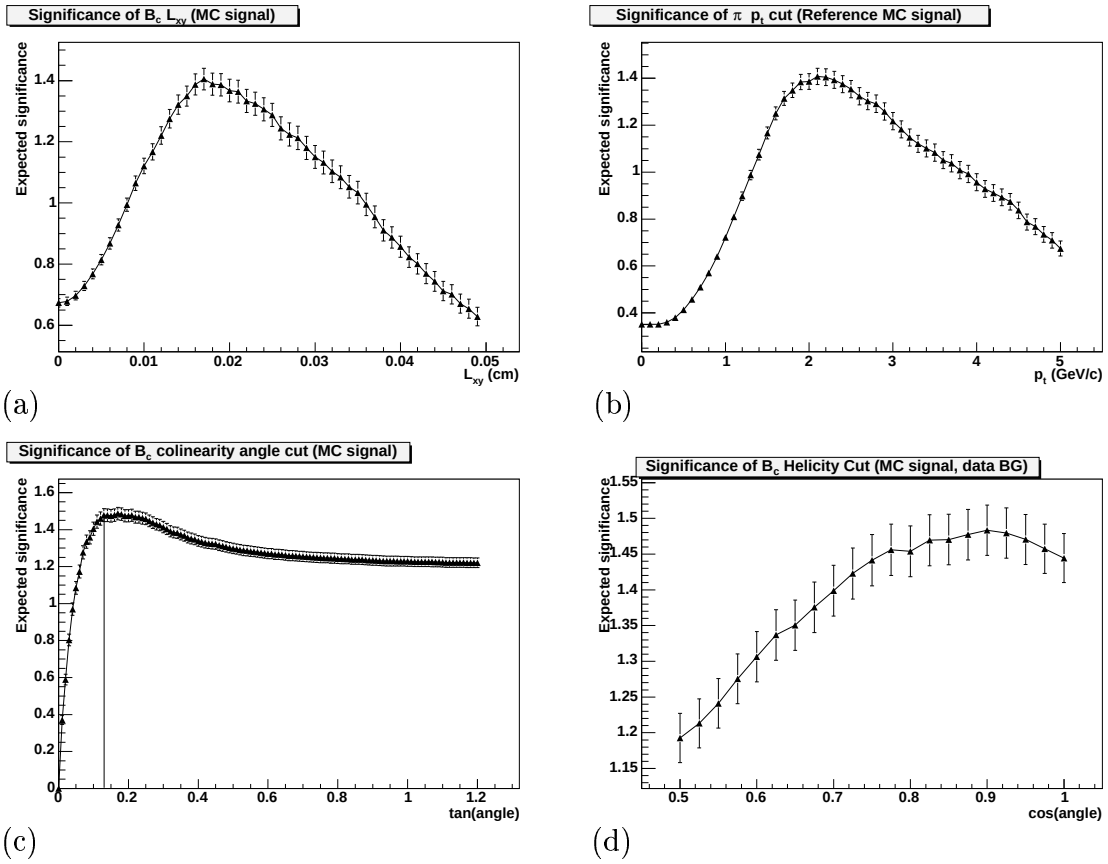

Figure 4.24: Sequential optimisation of cuts: (a) L_{xy} (b) pion p_T (c) Collinearity angle (d) J/Ψ helicity angle. The sensitivity is plotted in Σ terms, with the trigger and reconstruction efficiency ratio assumed to be 1 in this scale.

the background consists of a population of relatively soft pions that are fortuitously associated with a J/ψ.

The optimal cuts applied on both Monte Carlo and data sample give the breakdown of efficiency and background rejection shown in Fig. 4.25, with the detailed power of each cuts. With the additional silicon track requirements, the data sample now only features $N_{B^\pm} = 2300$ $B^\pm$ candidates. The relative efficiency, the ratio of the number of B_c Monte Carlo events remaining after the B_c cuts with the number of $B^\pm$ Monte Carlo events with the same cuts, is evaluated:

$$\epsilon_R = \frac{\epsilon_c}{\epsilon_u} = \frac{1827 \pm 45}{5211 \pm 122} = (0.35 \pm 0.01).$$

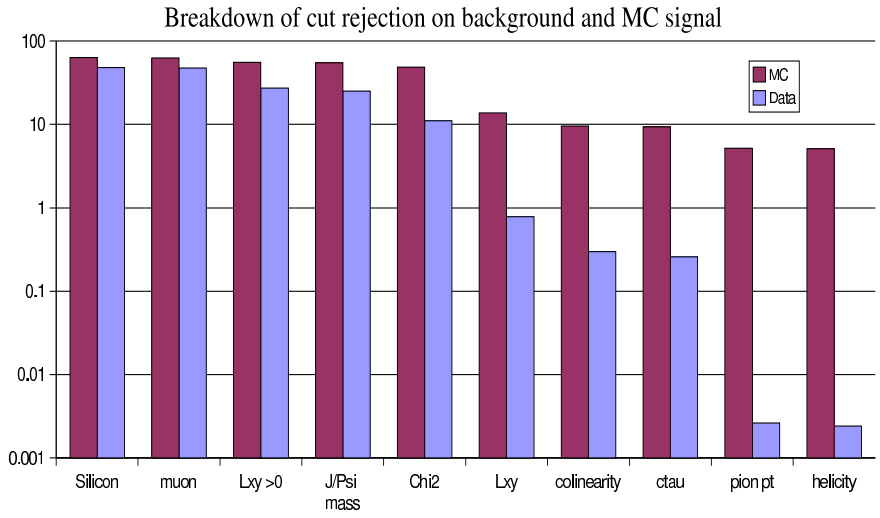

Figure 4.25: Breakdown of rejection power and signal efficiency reduction for each cut. Note the logarithmic scale.

It gives an expected number of B_c signal events $\epsilon_R N_{B^\pm} R \sim 8$. This is to be compared with the 310 candidates that survive the optimal cuts within the whole blinded region $5.6 \leq M \leq 7.2$ GeV/c^2, and give support to the assumption of a negligible signal contamination in the blind region when the data are treated as background.

Quantity cut on	Initial value of cut	Optimised value of cut
dimuon mass	± 55 MeV wrt M(J/ψ)	
χ^2 of vertex fit	< 20	
$c\tau$ (upper)	$< 800 \mu$m	$< 800\,\mu$m
p_T of muons	> 1.5 GeV/c	
$\lvert J/\psi$ helicity$\rvert$	< 0.9	< 0.9
p_T of $\pi^\pm$	> 2.6 GeV/c	> 2.0 GeV/c
L_{xy}	> 0	$> 170\,\mu$m
B_c Collin. angle	< 0.10	< 0.13

Table 4.3: Values of cuts on physical quantities. Above the double line the values are fixed; below they are initial values as a basis for the sequential optimisation procedure.

The expected sensitivity of the present analysis cuts can be calculated to measure the potential of signal observation. This depends on the model used, such as B_c meson lifetime and p_T spectrum. A measure of the sensitivity can be done in terms of Σ function for instance, where the background B corresponds to the expected background under the B_c meson mass peak. In order to determine the signal region, only the fit of a Monte Carlo signal prediction can be used. It is verified on the control sample that the Monte Carlo correctly predicts the width of the $B^{\pm}$ invariant mass with respect to the value found with the data. Therefore, it is reasonable to rely on the Monte Carlo for the predicted B_c width $\sigma_M(B_c) = 15.1 \pm 0.5$ MeV/c^2 and the definition of a $\pm 2\sigma$ signal region representing 3.77 % of the whole blinded mass window. Assuming an average value of the background events $B = 310 \times 0.0377 = 11.7$, the resulting sensitivity can be evaluated for various Monte Carlo samples with different B_c decay lifetime hypothesis, as shown in table 4.4 and in fig. 4.26.

Although this metric measurement of the sensitivity is arbitrary, there is clearly a small number of expected B_c events. There is the need to increase the signal selection power of the cuts by extracting more informations from the 3-track vertex fit, using L00 and the track–fitted primary vertex (EbE) calculation. The second set of data stream whose validation was shown in the section of the use of a $B^{\pm}$ control sample, will now be added to use the 360 pb^{-1} of data.

Monte Carlo sample	Pt Spec.	ct	Σ
m522	(C)	138	1.63 ± 0.4
m524	(B)	138	2.87 ± 0.4
m538	(C)	83	0.94 ± 0.4

Table 4.4: Score in Σ terms for three 3 Monte Carlo samples considered, using the same optimised cuts. For all three samples, the B_c mass is assumed to be $M_{B_c} = 6.4$ GeV/c^2.

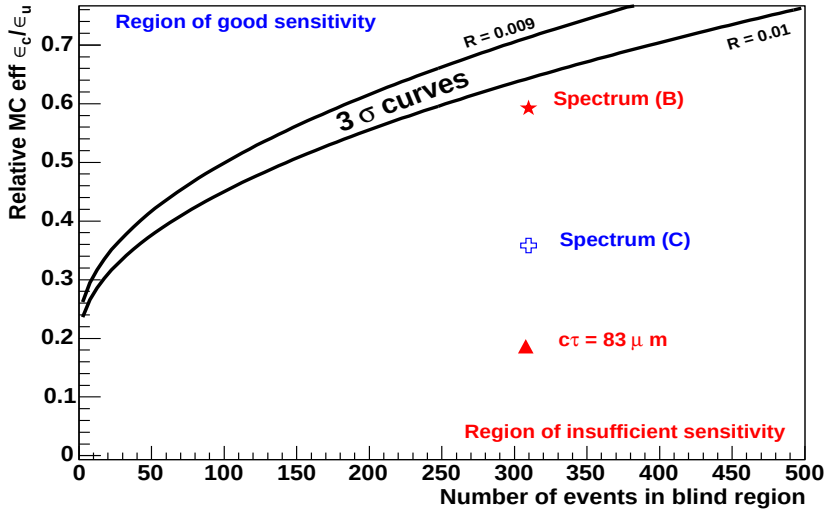

Figure 4.26: Sensitivity as a function of the relative efficiency $\frac{\epsilon_c}{\epsilon_u}$ and the total number of events in the blind region, for different models and ratio R. The standard Monte Carlo model for $p_T(B_c)$, with $M_{B_c} = 6.4 GeV/c^2$ and of lifetime 138 μm is labeled spectrum (C).

4.5.8 Significance of the Projected Decay Length

The $x-y$ component of the decay length projected along the candidate p_t (L_{xy}) is a powerful variable to select candidates with lifetime as shown in Fig. 4.25. Because the B_c decay length is not precisely known, the alternative use of the significance of the decay length $\frac{L_{xy}}{\sigma(L_{xy})}$ was introduced earlier, to take advantage of the better precision on the error $\sigma(L_{xy})$ provided by the layer L00. This error depends primarily on the accuracy of the tracks, which relates to the number of silicon hits per track. It does not depend on the quality of the 3-track vertex fit, but it depends on the error on the primary vertex, so that the track–fitted primary vertex (that is also referred to event–by–event–vertex, or EbE) could be advantageously used if its gain were to be demonstrated and quantified. The $B^{\pm}$ control sample is used for that purpose; by representing graphically the L_{xy} significance distributions for data and Monte Carlo (see Fig. 4.27), the impact of the EbE can be verified and compared to the standard determination of the vertex using the beam line data base. To analyse a dependence

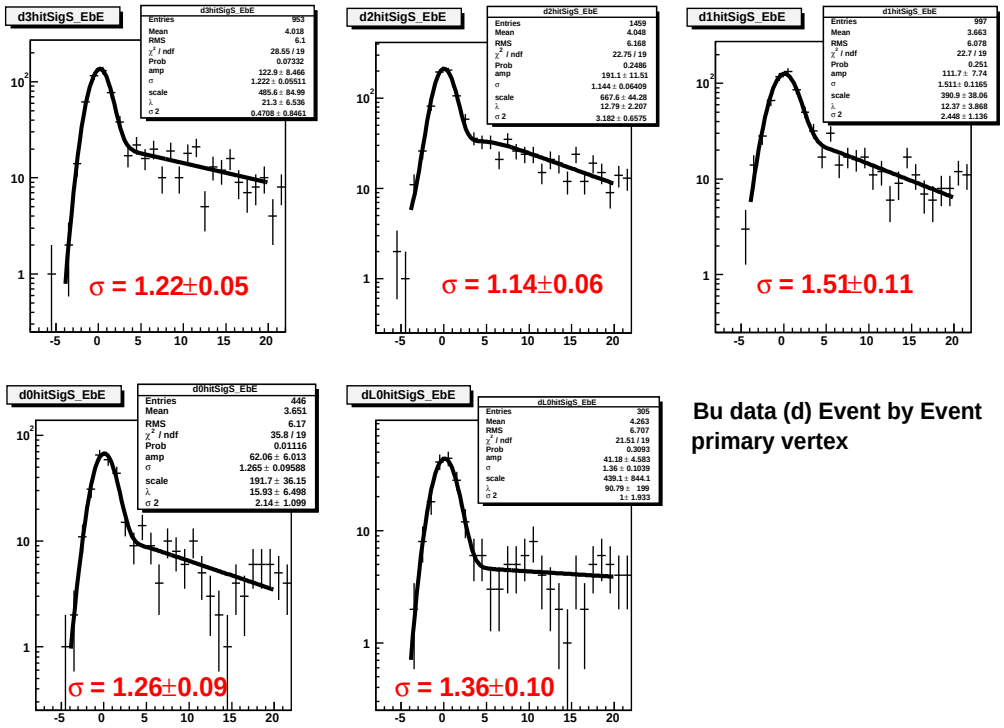

Figure 4.27: Significance of the projected decay length $L_{xy}/\sigma(L_{xy})$ for pre-COT aging data ($B^{\pm}$) in case of track–fitted primary vertex, for the 5 cases of L00 and L0 hits content. The fits are obtained with the function described in the text.

on the L00 hits, a classification based on the number of tracks that have an associated L00 hit is done before fitting the distributions. The function used for the fit has to reflect the physical properties that are responsible for these distributions. It consists of a Gaussian due to the primary vertex resolution, given by the prompt part, and a function f as an exponential convoluted with a Gaussian due to the decay of the $B^{\pm}$ meson. This second function has the following analytical form: [35]:

$$f = \int_0^{+\infty} \frac{1}{\lambda} exp(-\frac{x'}{\lambda}).\frac{1}{\sqrt{2\pi}S\sigma_x} exp(-\frac{(x-x')^2}{2S^2\sigma^2}).dx'$$

where λ is the lifetime term of the decay, and $S\sigma_x$ is the width of the second Gaussian distribution (not the main one for the resolution).

This study aims at analysing several different characteristics; the advantage of

EbE, the impact of having two data samples due to the COT history[1], and a possible optimal number of L00 hits for the decay tracks (cf. Fig. 4.28). The understanding of the L00 impact in both data and Monte Carlo samples is also investigated here, as a further Monte Carlo validation, to verify if the L00 properties are well reproduced by the CDF software. The BGENERATOR standard Monte Carlo usually employed cannot be used when the EbE technique is being studied. Because primary tracks are needed to determine the primary vertex fit, for the model of the control sample $B^{\pm} \to J/\psi K^{\pm}$, a PYTHIA Monte Carlo is substituted for the BGENERATOR Monte Carlo, which only features B meson signal events.

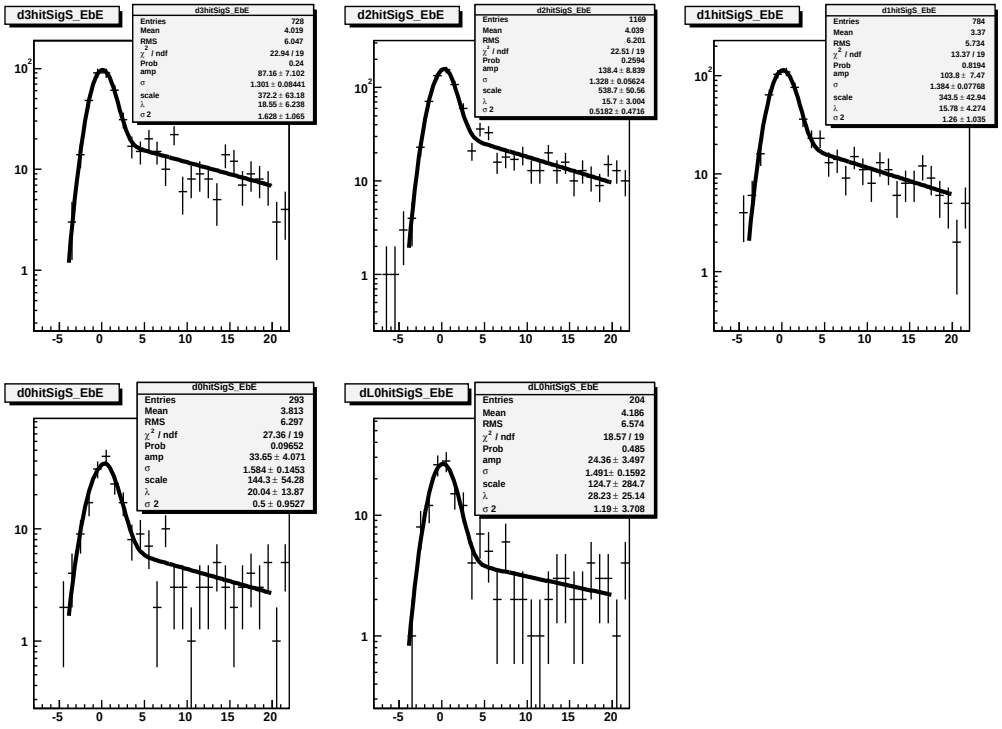

Figure 4.28: Significance of the projected decay length $L_{xy}/\sigma(L_{xy})$ for post COT recovery data ($B^{\pm}$) in case of track–fitted primary vertex. From top left to right, tracks with 3 l00 hits, 2 hits, 1 hit, no l00 hit, and no l00 hit but one L0 hit on the bottom right.

[1] The check discussed earlier only concerned the yield and resolution stabilities.

By selecting the population of events that corresponds to the $B^{\pm}$ mass peak, i.e. the ensemble of $J/\psi K$ tracks obtained after cuts that come from $B^{\pm}$ meson decays, the characteristics of these $B^{\pm}$ signal events in terms of the quantity $\frac{L_{xy}}{\sigma(L_{xy})}$ can be checked. The prompt resolution is the quantity of interest here, and a precise vertex determination is essential for this analysis, with the best resolution. Since these investigations only concern the detector properties, it is reasonable to expect the same characteristics for the background and the sought B_c signal. The correct fit of the entire distribution is important in order to obtain an accurate value of the width σ of the prompt Gaussian distribution associated to the vertex resolution.

Table 4.5 summarises the results of the fits and the obtained prompt resolutions, with comparisons between the standard method of vertex measurement (Std), the use of the EbE technique, the data sample before the COT problem (A) and after the COT recovery (B). Results for Monte Carlo are also shown with the dependence on the various silicon hits possibilities. There are no indications of a correlation with the L00 content. In order to perform a correct optimisation using the Monte Carlo signal sample, it is important that the data are well reproduced. This study shows that a scale factor needs to be applied to the Monte Carlo with the value 1.19 for cases of at least one L00 hit and a value of 1.38 for cases without L00 hit.

It is found that the analysis can be done using both data set without the exclusion of a particular configuration on the L00 hits, and that the EbE technique can be used, although it does not clearly improve the resolution. For the cut optimisation, a factor with a changing value depending on the L00 hits has to be applied to the Monte Carlo in order to scale the data.

	Std (A)	EbE (A)	Std (B)	EbE(B)
3 L00 tracks	1.13±0.06	1.22±0.05	1.26±0.08	1.30±0.08
2 L00 tracks	1.20±0.06	1.14±0.06	1.31±0.05	1.32±0.05
1 L00 track	1.52±0.07	1.51±0.11	1.34±0.08	1.38±0.07
No L00 track	1.28±0.11	1.26±0.09	1.44±0.13	1.58±0.14
No L00, 1 L0	1.30±0.11	1.36±0.10	1.38±0.16	1.49±0.16
	Monte Carlo (Std)	Monte Carlo (EbE)	-	-
3 L00 tracks	1.05±0.04	1.00±0.02	-	-
2 L00 tracks	1.17±0.03	1.14±0.03	-	-
1 L00 track	1.20±0.08	1.18±0.11	-	-
No L00 track	1.18±0.02	1.14±0.02	-	-
No L00, 1 L0	1.19±0.02	1.13±0.02	-	-

Table 4.5: Summary of the results of the fits. This table shows the value of the σ parameter for the prompt component of $L_{xy}/\sigma(L_{xy})$. If the error on L_{xy} is calculated correctly these values should be close to 1. EbE indicates track-fitted primary vertex, Std indicates "standard" beam line from the database.

4.5.9 Study of the Vertex χ^2

The vertex χ^2 is a key parameter to distinguish real 3-track (3-D) vertices from random combinations of J/ψ di–muons with nearby tracks, a potentially large source of background. The earlier study on this variable with one data set and standard vertex determination suggested a poor reliability of an optimisation using a BGENERATOR Monte Carlo sample, and concluded on a cut 3-D χ^2 <20, based on data. This is clearly not restrictive and has small background rejection power (see Fig. 4.25). The use of the EbE technique for vertex calculations with a PYTHIA Monte Carlo requires an updated verification of the agreement between Monte Carlo and data. This is done with $B_{\pm}$ the control sample. The number of degrees of freedom N_{dof} for the 3-D χ^2 is given by:

$$N_{dof} = 2N_t - 3N_v + N_p + N_m + N_c,$$

where N_t is the number of tracks, N_v is the number of vertexes, N_p is the number of point constraints, N_m is the number of mass constraints and N_c is the number of conversion constraints. The expected N_{dof} for the χ^2 here is 4. Fig. 4.29 shows for

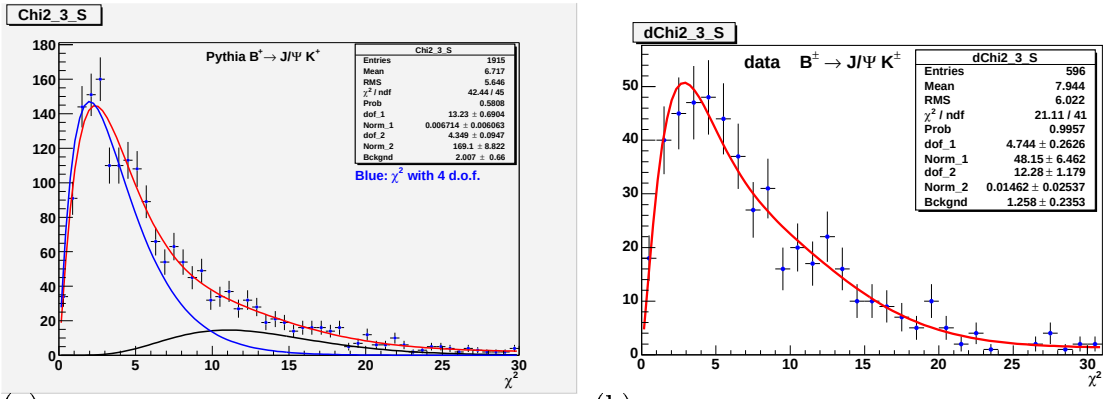

(a) (b)

Figure 4.29: (a) Distribution of the χ^2 for the PYTHIA Monte Carlo sample $B^{\pm} \to J/\psi K^{\pm}$. The blue curve underneath the fit represents the expected distribution. (b) The same for $B^{\pm}$ data. The selection requires candidates with three tracks that have all a L00 hit.

the reference decay $B^{\pm} \rightarrow J/\psi K^{\pm}$ the χ^2 distribution comparison between Monte Carlo (a) and data (b). For both cases, a χ^2 with N_{dof} =4 does not describe well the distributions, since a further empirical "artificial" component needs to be added in order to fit correctly the distributions. This indicates that there are classes of tracks for which the errors on the parameters are underestimated. However, both Monte Carlo and data need the same correction, and an optimisation on the χ^2 variable using the B_c Monte Carlo sample is possible.

4.5.10 Study of the Impact Parameter of the Candidate

As shown in Fig. 4.20, the impact parameter d_0 of the candidate is a good candidate for selecting the decay signal. It was used via the collinearity angle ($\frac{d0}{L_{xy}}$) for a preliminary sensitivity test. The impact parameter alone is possibly a more suitable cut variable however, since it does not involves L_{xy}, and the collinearity angle cut can be substituted by two independent cuts on d_0 and $\frac{L_{xy}}{\sigma(L_{xy})}$. The use of the EbE technique can also benefit to the d_0 discriminating power. A study is done on the resolution of d_0 using the $B^{\pm}$ control sample and compared with the results of a PYTHIA Monte Carlo. This includes a dependence on the L00 hits possibilities for the three tracks. The $B^{\pm}$ candidates are selected from the data and Monte Carlo samples using the cuts determined by CDF for a lifetime analysis [35] (see section on the use of a reference decay). The distribution of the d_0 for the selected signal events is then fitted with a Gaussian function and the resolution widths σ are obtained (Table. 4.6). As for all the comparisons of this analysis using a signal from the data, a technique of sideband subtraction is employed to clean the selection of possible background contamination. There is a significant improvement of the resolution by using the EbE vertex calculation as opposed to the standard beam line based technique. Although the gain is not obvious for the $\frac{L_{xy}}{\sigma(L_{xy})}$ variable, the clear improvement for the d_0 motivates the use of the EbE technique. Because the final cut optimisation is done

	Std (Data)	Std (MC)	EbE (Data)	EbE (MC)
3 tracks	35.8±1.3	28.52±0.40	30.9±1.0	26.52±0.37
2 tracks	31.8±0.9	31.15±0.59	28.7±0.8	26.64±0.49
1 track	35.2±1.4	31.43±1.14	29.9±1.1	29.88±1.07
0 track	36.6±2.6	33.22±1.28	33.9±2.3	30.52±1.14
0, all L0	38.3±3.4	30.34±1.46	30.6±2.4	29.14±1.40

Table 4.6: Resolution of the impact parameter (μm) of the reconstructed $B^{\pm}$ meson for different cases of tracks with L00 hits. The data sample corresponds to the post COT-recovery.

with a signal from a Monte Carlo sample, the agreement Monte Carlo with data is also important. It is fairly poor for the case 3 L00 hits per track, but acceptable for the other cases, also no silicon hits based discrimination is retained.

4.5.11 A Further Pointing Variable: The β Angle

Because the track–fitted primary vertex allows for a more precise measurement of the primary vertex coordinate along the beam line, an additional criterion for the search of the $B_c \longrightarrow J/\psi\pi$ decay can be applied. With this increased precision, the angle between the momentum of the reconstructed meson and the secondary vertex (cf. Fig. 4.30) can be used as another vertex pointing technique. The purpose is to select events that are coming from a precise location in space. The distribution of the β angle is predicted by a PYTHIA Monte Carlo to tend to zero, in contrast to the surrounding background (Fig. 4.31), hence revealing a potential discrimination power. The variable β is correlated to the d_0, and a cut optimisation procedure is ideally operated on orthogonal variables. A grid optimisation of the cuts on $d_0(B)$ and β is done and it is found that there are no parasitic interactions between the two quantities. Applying a cut on the β angle once an d_0 cut is done may bring an additional background rejection benefit.

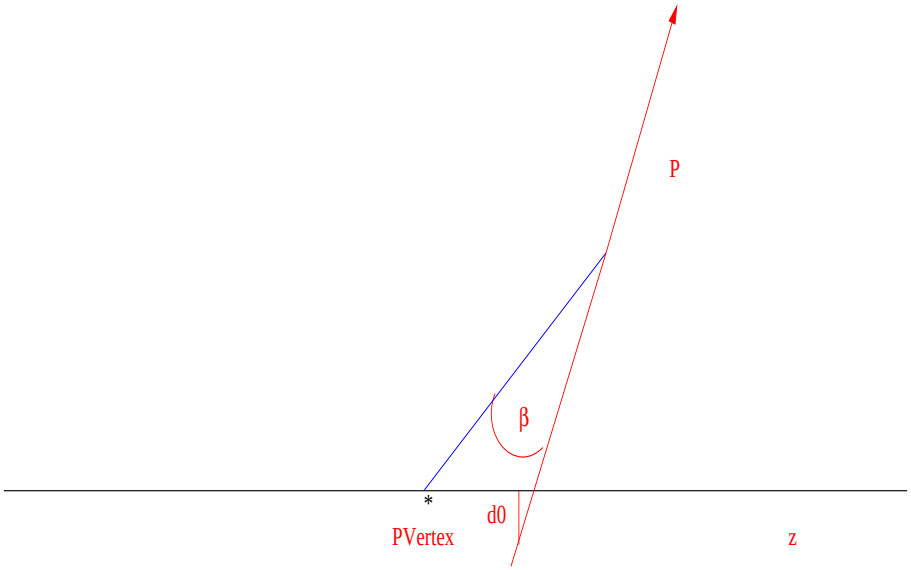

Figure 4.30: Definition of the β angle in 3-D.

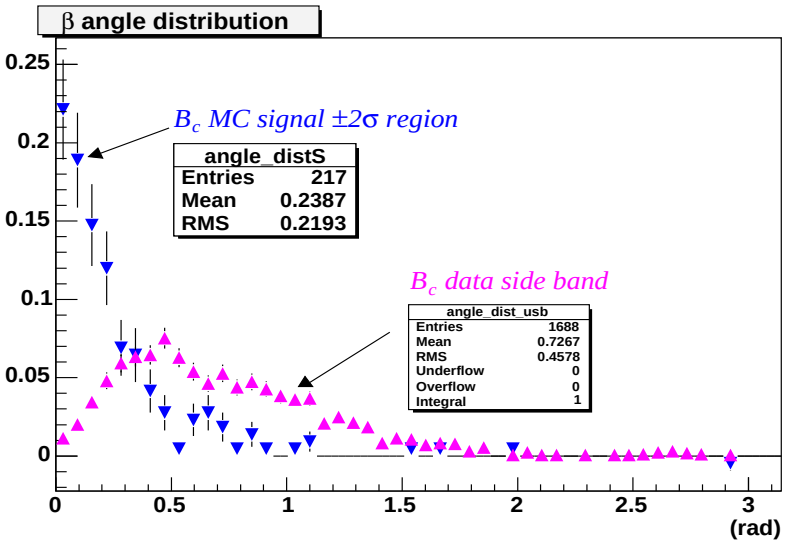

Figure 4.31: Distribution of the pointing angle for the PYTHIA Monte Carlo sample $B_c^{\pm} \to J/\psi\pi^{\pm}$ (downward blue triangles) and for data (upward magenta triangles), assuming data is mainly background. Points are normalized to unit area in histogram.

4.5.12 Cuts Optimisation

The addition of new data sample after the COT recovery, the introduction of a more suitable lifetime variable ($\frac{L_{xy}}{\sigma(L_{xy})}$), the use of the EbE technique and its gain in precision for the impact parameter, give a set of new conditions suitable for the final optimisation procedure, also using the "n-1" method. The variables retained for the optimisation are the significance of L_{xy}, the pion transverse momentum , the impact parameter of the candidate, the β angle, the χ^2 of the 3-D vertex fit and the upper limit on the proper decay length ct of the candidate (see Fig. 4.32).

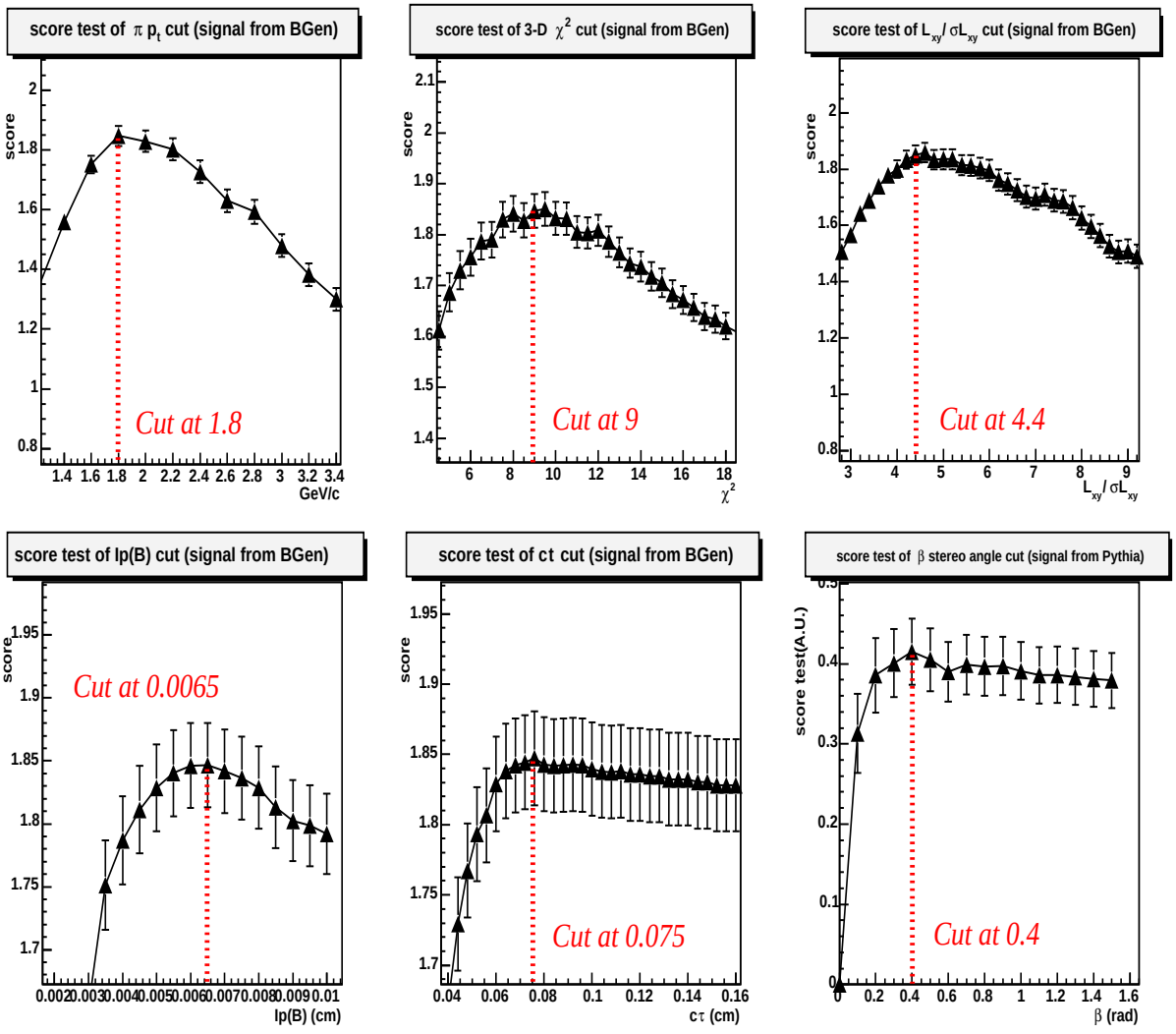

Figure 4.32: Cut optimisation of the six variables for the analysis of $B_c \to J/\psi\pi$.

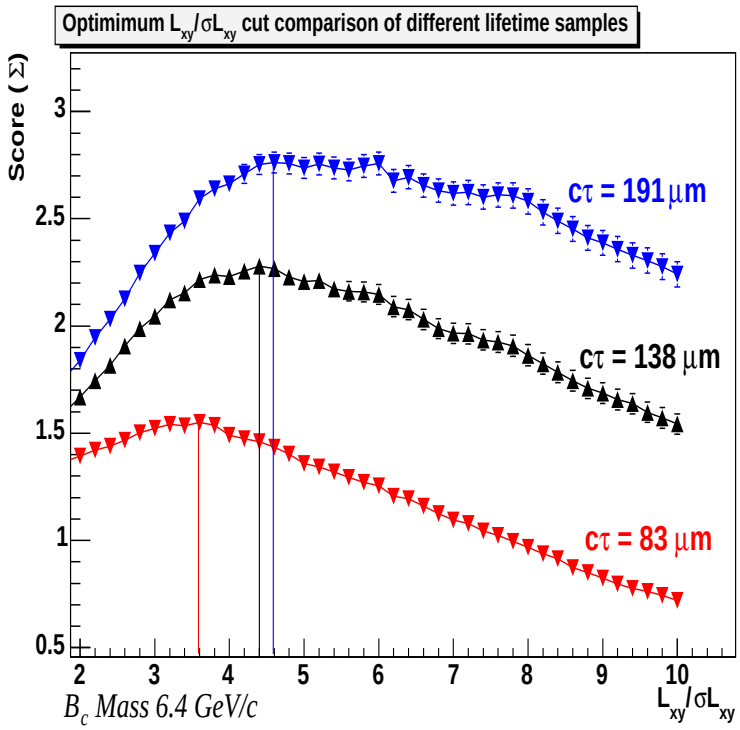

Figure 4.33: L_{xy} significance cut optimisation for 3 different B_c lifetimes.

The sensitivity is expressed in terms of the Σ function, to give the detection potential of the cuts for the $B_c \longrightarrow J/\psi\pi$ decay with respect to the $B^{\pm} \longrightarrow J/\psi K^{\pm}$ decay. This however is not an absolute criteria since several unknowns remain such as the ratio R, and the assumptions of Monte Carlo models.

The Monte Carlo used to simulate the B_c signal is BGENERATOR for all the variables except for the optimisation on the β angle that is using a PYTHIA Monte Carlo for the track–fitted primary vertex technique. The impact parameter is used as a pointing cut only in the cases where the EbE primary vertex fit fails (about 1%) in the $B^{\pm}$ data sample, otherwise the β angle is used instead. Because of the different Monte Carlo sample, the $y-$axis for the optimisation on the β angle does not indicate the same Σ sensitivity.

Each of the six quantities presents an optimal cut value that maximises the Σ function. To verify the systematic error on the cut value for the $\frac{L_{xy}}{\sigma(L_{xy})}$ variable, two

other optimisations are done using Monte Carlo samples with different assumptions on the proper decay length of B_c (83 μm and 191 μm) as shown in Fig. 4.33. The breakdown of efficiency and background rejection for each cut *alone* is shown in Table 4.7.

	MC entries	ϵ	data entries	ρ
3-D χ^2	4086	80.5%	762	48.4%
d_0	3377	97.5%	488	19.5%
$\frac{L_{xy}}{\sigma L_{xy}}$	7836	42.0%	11930	96.7%
πp_t	5288	62.3%	3043	12.9%
ct	3336	98.7%	410	4.1%
$\pi\chi^2$	3553	92.7%	565	30.4%
3-D β angle	110	85.4%	768	48.8%

Table 4.7: Monte Carlo efficiency (ϵ) for each cut and background rejection power (ρ) calculated from data. Efficiency ϵ and rejection power ρ are calculated as $\epsilon = N_f^{MC}/n_i^{MC}$, $\rho = 1 - N_f^{data}/n_i^{data}$, where N_f is the number of candidates passing all cuts and n_i is the number of candidates passing all the other cuts before applying the i^{th} cut. $N_f^{MC} = 3293$ in case of BGENERATOR MC, $N_f^{MC} = 101$ in case of PYTHIA sample and $N_f^{data} = 393$.

4.5.13 Additional Variables and Cuts List

In the vertexing procedure, the third track is treated differently from the muon tracks because it is not mass-constrained, and the vertex 3-D χ^2 has contributions from three terms, one for each track: $\chi^2 = \chi^2(\mu_1) + \chi^2(\mu_2) + \chi^2(\pi)$. A study is done using the $B^{\pm}$ control sample where it is required that the $K^{\pm}$ contribution to the χ^2 is of the same order or less compared to the μ contribution, as a quality requirement of the third track fit. With the cuts of the CDF $B^{\pm}$ lifetime analysis [35], this additional

requirement retains 2028 of the 2540 initial $B^{\pm}$ signal events in the data stream, indicating that 20% of the signal has the highest 3-D χ^2 contribution coming from the third track (see Fig. 4.34). This is confirmed in the Monte Carlo sample, and has to be compared to 50% for the background population. This difference justifies an optimisation on a cut of the π contribution to the χ^2 (Fig. 4.35).

There is a clear correlation with the total χ^2, and an optimisation on the 3-D χ^2

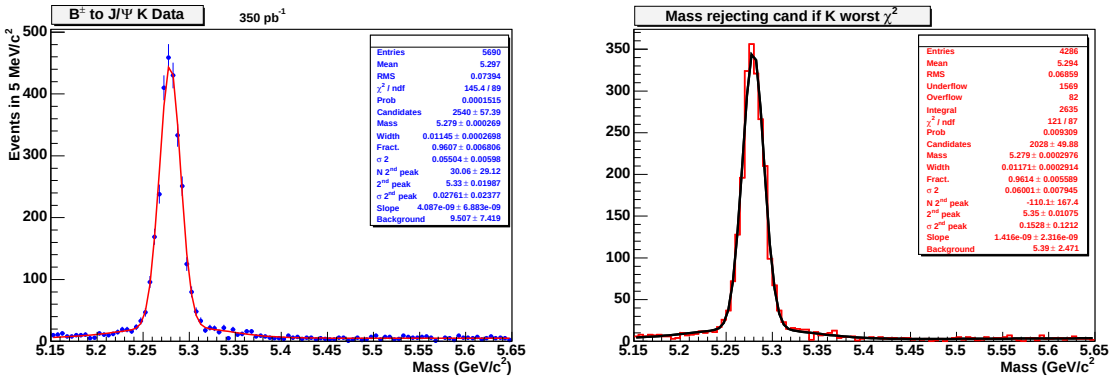

(a) (b)

Figure 4.34: Mass peak of the B_u using the standard cuts (a) and adding the selection $\chi^2_K < \chi^2_{\mu_{1,2}}$ (b). 20% of the $B^{\pm}$ signal events are removed, and 50% for the background.

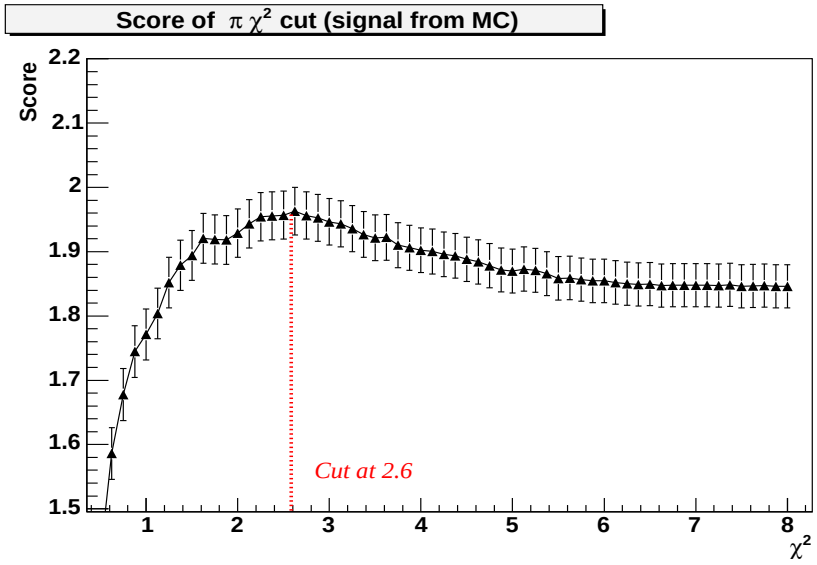

Figure 4.35: Optimisation of the contribution of the π to the 3-D χ^2 with all the other B_c optimised cuts applied.

performed retroactively while including a cut such that $\chi^2(\pi) < 2.6$ does not give an optimum value for the 3-D χ^2 anymore, because of the already discriminative power of the π term. Since an optimal value for the π χ^2 contribution is still found even with a 3-D χ^2 cut at 9 applied, there is an indication of an increased background removal capability for the π χ^2 contribution.

The final list of the quantities with their associated cut values for the search of the B_c decay is given in table 4.8.

Quantity	Optimised value of cut
dimuon mass window	3097 ± 55 MeV
χ^2 of vertex fit	< 9.0
ct (upper)	$< 750\,\mu$m
p_T of $\pi^{\pm}$	> 1.8 GeV/c
$L_{xy}/\sigma(L_{xy})$	> 4.4
$d_0(B)$	$< 65\mu m$
β angle	< 0.4
3rd track component χ^2 of vertex fit	< 2.6

Table 4.8: Values of cuts on physical quantities.

4.6 Signal Extraction

The large uncertainties existing up to now on the B_c mass and lifetime result in a range of the potential for detection given the optimised cuts. This section presents the variation of the expected sensitivity and a method for interpreting the data, once the cuts of the analysis have been applied.

4.6.1 Attained Sensitivity

The number of $B^{\pm}$ signal events for the control decay is determined by applying the analysis cuts optimised for the B_c search (Table. 4.8), on the entire data sample (360 pb^{-1}). The upper ct cut is not applied, since a restriction at 750 μm would affect the $B^{\pm}$ event selection ($ct(B^{\pm})$ around 500 μm). In principle, exactly the same cuts have to be applied, however the relatively small effect of the ct cut on the B_c sample (4.1%) allows for not using this cut (cf. Table. 4.7). The resulting mass plot is shown in Fig 4.36, with $N_{B^{\pm}} = (2378 \pm 57)$ candidates found, while the same analysis cuts applied to a $B^{\pm}$ Monte Carlo sample give 9950±210 remaining $B^{\pm}$ candidates out of

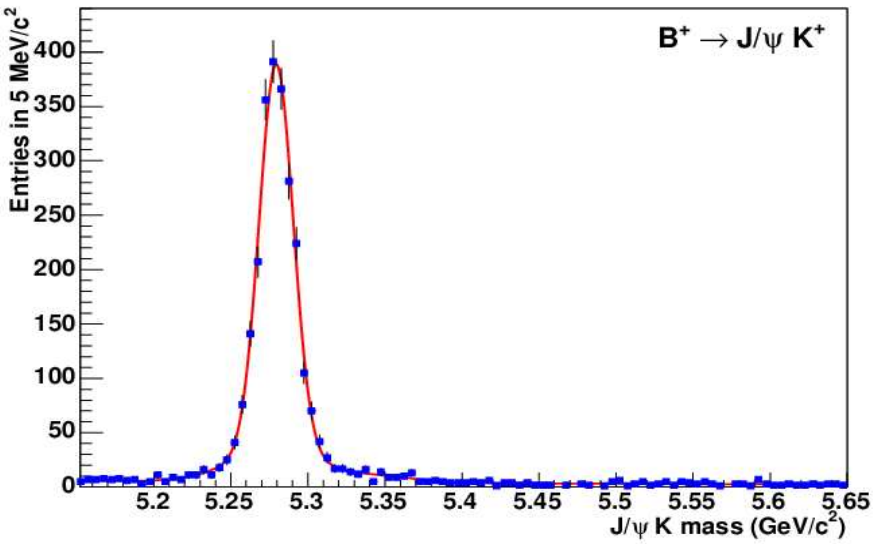

Figure 4.36: Mass distribution for $B^{\pm}$ candidates (data, 360 pb^{-1}) using the cuts for the B_c search, except the upper ct cut. 2378 candidates are found.

the 2×10^6 initially generated (see Fig. 4.37 (a)). A fit with three Gaussian functions is done to determine $N_{B^\pm}$ in (Fig 4.36), to describe the central peak, the base of the central peak and the Cabbibo suppressed decay $B^\pm \longrightarrow J\psi\pi^\pm$.

The Monte Carlo efficiency for the B_c signal is calculated by applying the same analysis cuts, leaving 2917±63 candidates out of the 10^6 generated (Fig. 4.37 (b)). This gives the relative efficiency ϵ_R between the two Monte Carlo samples:

$$\epsilon_R = \frac{\epsilon_c}{\epsilon_u} = \frac{2917 \pm 63/10^6}{9950 \pm 209/2.10^6} = (0.586 \pm 0.017)$$

and an expected number of B_c events:

$$N_{B_c} = \epsilon_R N_{B^\pm} R = 0.586 \times 2378 \times 0.008 = 11.1$$

The result of the cuts on the blind mass spectrum is shown in Fig. 4.38, where the 390 candidates are partitioned into two bins. The lower population for the bin of mass below 6.4 GeV/c^2 is consistent with the data including events arising from partially reconstructed decays, while above there is just a combinatorial background.

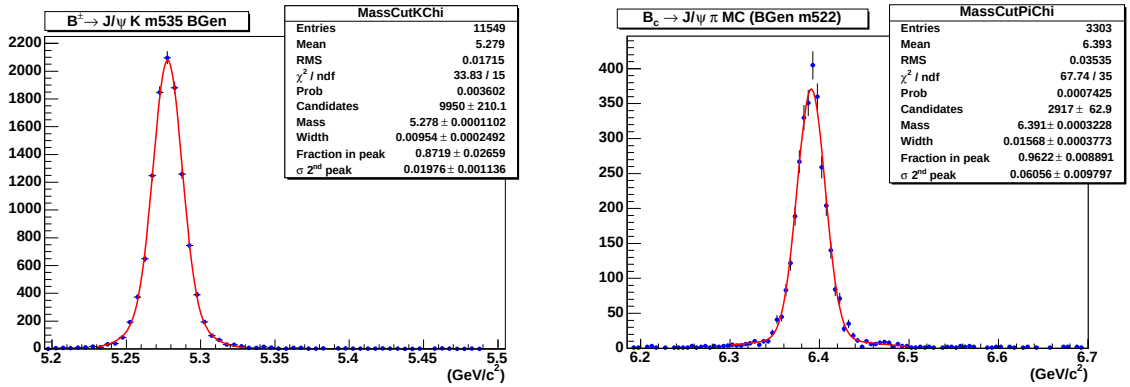

(a) (b)

Figure 4.37: Mass peaks of the $B^\pm$ (a) and the B_c (b) obtained with BGENERATOR Monte Carlo samples using the B_c optimised cuts. This gives the predicted mass resolution and the relative efficiency.

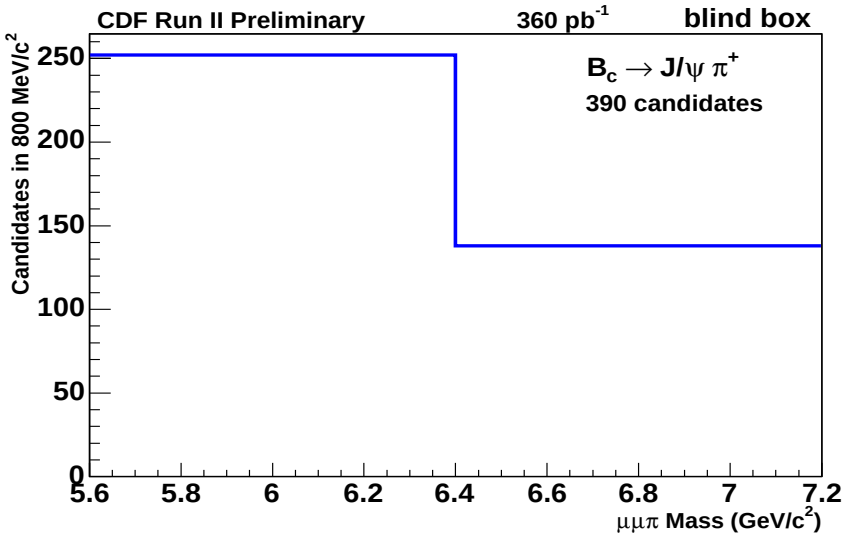

Figure 4.38: Blinded mass region with the B_c optimised cuts applied. 390 candidates are remaining from the 360 pb^{-1} data sample.

Considering all the candidates of the blind region as background, the number of background events B in a $\pm 2\sigma$ region centered around a nominal signal mass M =6.4 GeV/c^2 is:

$$B = N_B \times f_\sigma = 390 \times 3.77\%$$

where σ is the resolution of the mass measurement. This gives 15 background events for 11 predicted signal events,

4.6.2 Fitting Procedure

The procedure for the interpretation of the result is an important part of the analysis. After unblinding the [5.6-7.2] GeV/c^2 region with the analysis cuts applied, a final fit should be done on the possible signal, similarly to the case of the $B^\pm \longrightarrow J/\psi K^\pm$ decay shown in Fig. 4.36, to determine the number of B_c events and the mass of the meson, if the signal is found. The search of the signal is based on a serie of fits with a function whose nature is a matter of investigation, and dependent on the fitting

range. Based on this fitting procedure, a criterion to establish the presence of a signal has to be determined before the analysis of the data.

The method chosen to search for a signal is done by using a scan with a "sliding window" of width 300 MeV/c^2, running from the low end of the blind region (5.8 GeV/c^2) to its upper end (7.0 GeV/c^2) , in steps of 10 MeV/c^2. During a scan, at each step of the sliding window, a fit is performed *within the range of the window* using a suitable function. A decay signal is ideally described by a Breit-Wigner distribution, but the resolution is governed by the detector and the resulting distribution is a Gaussian. The fitting function thus includes a Gaussian with three parameters (σ, μ, amplitude) in order to describe the signal. This gives the number of signal events S found in the peak. The fit makes use of the total width of the sliding window to estimate the background, since the relevant information is the possible presence of an excess at a specific location with respect to the immediate surroundings. The background is modeled with a linear function extending both sides of the signal Gaussian, so that the 300 MeV/c^2 wide sliding window is divided into two parts. The linear function normalised to ± 3 σ under the Gaussian peak centered at μ provides the background B, for estimating Σ.

During a scan, for each fit performed at a step of the sliding window, a sensitivity Σ is calculated using the found parameters S and B:

$$\Sigma = \frac{S}{1.5 + \sqrt{B}}$$

This is the function determined by G. Punzi [49]. Although it is designed to optimise the cuts with a 3 σ background rejection level, the choice of this particular function for scanning purpose is somewhat arbitrary.

A statistical test to establish the presence of the signal is needed. It is based on the method described by Rolke and Lopez [50], which consists on testing the null hypothesis of a signal presence. For this present analysis, this is done by performing the scan with the sliding window on samples generated using a Monte Carlo that

models the blind region [5.6,7.2] GeV/c^2, *without the presence of the signal*, and defining a threshold on the sensitivity based on the likelihood of a chance occurance of a peak.

This method requires the description of the background in the entire blind region. Its exact shape is unknown, and the blind region can only be fitted when the data will be analysed, and so some assumptions on the background composition are needed. To model various background components, the BGENERATOR Monte Carlo is used to simulate partially reconstructed contributions. This is described with a broad Gaussian function at the low end of the mass spectrum superposed on a uniform background. Fig 4.39 shows an example of the modeling of the blind region with different background components (partially reconstructed decays, combinatorial), including also a signal decay.

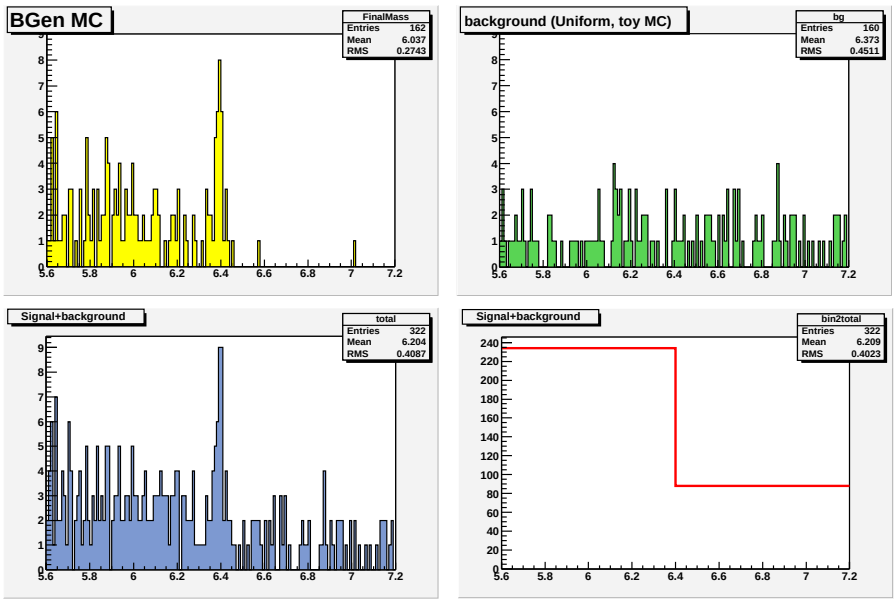

Figure 4.39: BGENERATOR Monte Carlo mass spectrum of signal and physical background (top, left); uniform background (top, right); sum of the two histograms (bottom, left) and resulting blinded histogram (bottom, right).

For the sensitivity test however, the probability distribution function consists of a pure background without the signal contribution, and 1000 Monte Carlo simulations of the blind region were made, each containing the same number of entries as the events in the data. The entries repartition is different for each simulation, with the restriction however of the distribution function shape to realistically describe the background. This provides the necessary statistics as suggested by Rolke and Lopez [50].

For each of the 1000 background simulations of the blind region, a scan is performed giving for each step of the sliding window a corresponding fit and a value of Σ. During the scan on Monte Carlo, the width σ of the signal Gaussian is proportional to the mass location (mean μ). This provides a set of 120 values of Σ per scan, and the highest Σ_{max} is recorded. The distribution of the highest Σ_{max} value for the 1000 background Monte Carlo models (labeled "No signal") is shown in Fig. 4.42.

The same test can be done when the distributions include the signal Gaussian, and 1000 scans of Monte Carlo simulations of the blind region were produced, with the background description and the signal decay. Fig. 4.40 shows a fit done at a typical step of the sliding window during a scan of a Monte Carlo model including the searched B_c signal. In this scan, the fit with maximum Σ happens when the μ of the sliding window is at the given input B_c mass of the Monte Carlo (6.4 GeV/c^2) and Fig. 4.41 shows the resulting scan in terms of Σ value, with Σ_{max} =5. The distribution of the Σ_{max} values in the presence of 30 B_c signal events is also shown in Fig. 4.42.

The criterion to establish the a priori presence of a signal when the scan is performed on the data is determined with the distribution of Σ_{max} for the 1000 Monte Carlo models *without* signal. A threshold Σ_{th} for Σ_{max} is found from Fig. 4.42 such that 999 scans on pure background satisfy:

$$\Sigma_{max} < \Sigma_{th}$$

This confidence level at 99.9% of pure background population gives Σ_{th} =3.5. This establishes the a priori threshold of detection for the decay $B_c \longrightarrow J/\psi\pi$ when the scan will be applied to the data.

The power of this test can also be determined. With a threshold set at Σ_{th} =3.5, for cases where a decay signal is included in the Monte Carlo description of the blind region, 95% of the distribution of Σ_{max} is above 3.5 when 30 signal events are present. With 20 signal events in the Monte Carlo, it was found that 40% of the distribution satisfies $\Sigma_{max} > 3.5$.

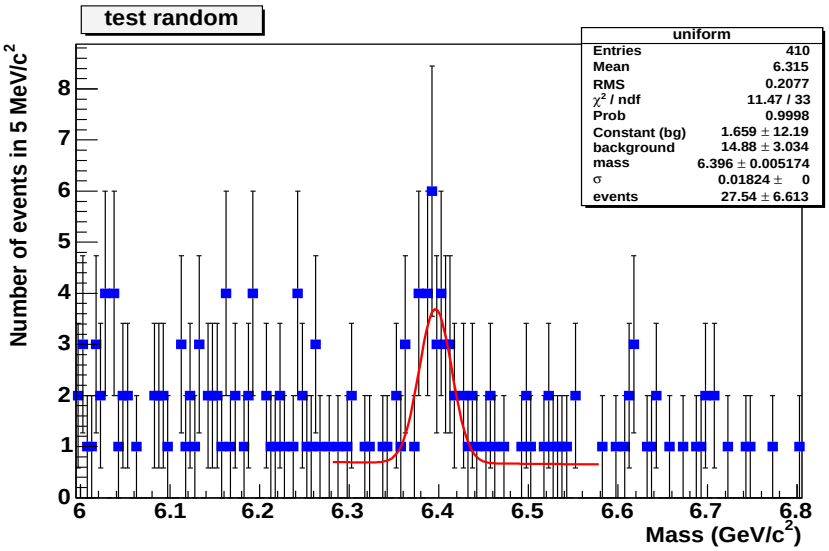

Figure 4.40: Scan of one Monte Carlo model of the blind region with a probability distribution function including background and signal. The fit with a Gaussian plus linear background is shown here when the 300 MeV/c^2 sliding window is at the location where $\mu = 6.4$ GeV/c^2.

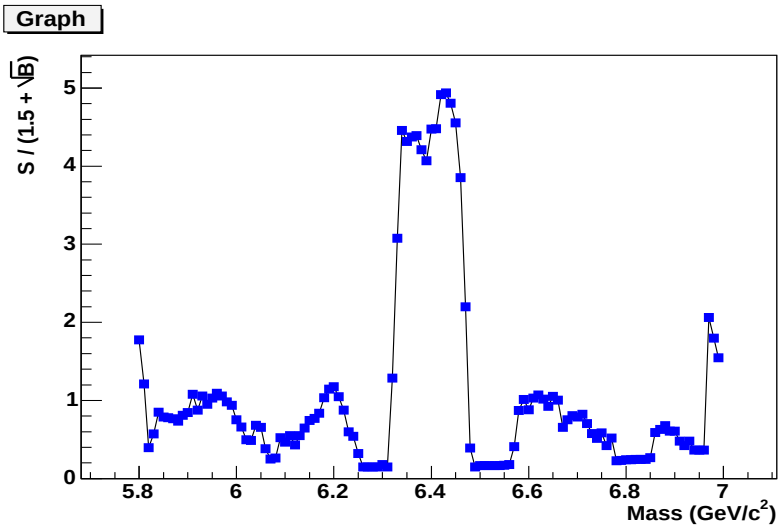

Figure 4.41: Result in terms of Σ score for the scan shown in Fig. 4.40.

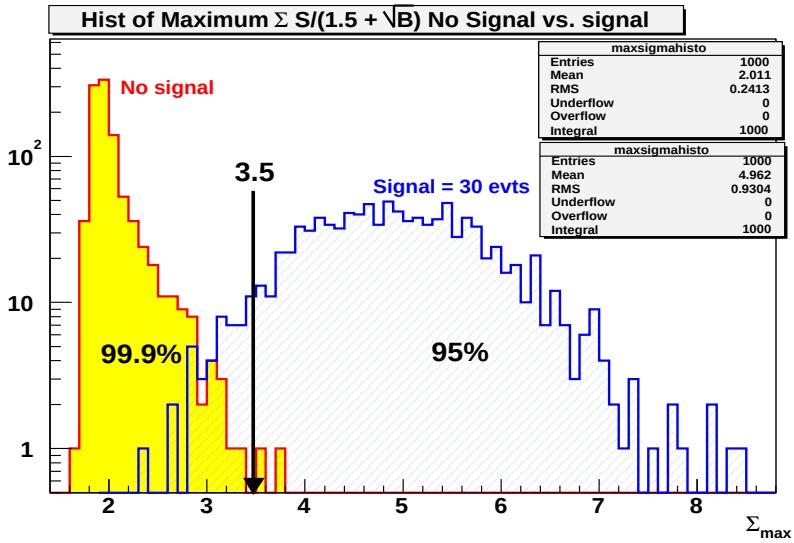

Figure 4.42: Distributions of Σ_{max} obtained from Monte Carlo for two cases; a case with 1000 scans on background only (No signal), and a case of 1000 scans with 30 signal events added. The left distribution sets the threshold value for signal detection (Σ_{th} =3.5), the right distribution defines the power of the test.

4.7 Result

4.7.1 Unblinding of the Region

With the determination of the optimised cuts and the method for the interpretation of the result, it was decided to analyse the data contained in the [5.6-7.2] MeV/c^2 blind region. Fig. 4.43 shows the mass spectrum when the cuts listed in Table 4.8 are applied. This is equivalent to the spectrum shown in Fig. 4.38 but with a bin width of 5 MeV/c^2 instead of 800 MeV/c^2.

The sensitivity test with a sliding window, as described in the previous section, is performed with one scan of 120 fits on the data to calculate $\frac{S}{1.5+\sqrt{B}}$ from the obtained S and B at each 10 MeV/c^2 step. The resulting Σ score distribution is shown in Fig. 4.44 with a maximum of $\Sigma_{max} = 3.6$ for a mass value around 6.29 GeV/c^2.

With a location on the mass spectrum where the threshold $\Sigma_{th} = 3.5$ is exceeded, the claim of the $B_c \longrightarrow J/\psi\pi$ signal detection was made.

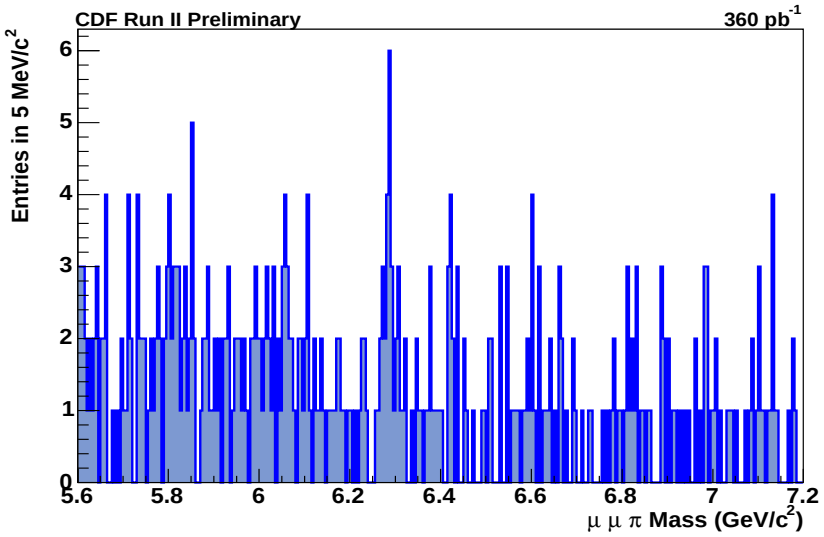

Figure 4.43: Invariant mass distribution of the candidates selected in the search region.

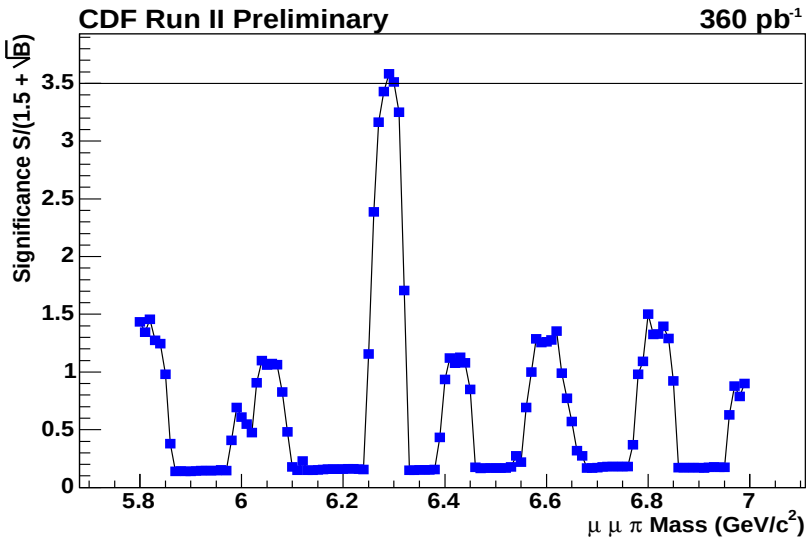

Figure 4.44: Score result of the sliding window scan for the data: Σ as a function of the invariant mass corresponding to the sliding peak position. The score threshold Σ_{th} is exceeded, allowing the claim for signal detection.

An unbinned likelihood fit of the region where Σ_{max} is reached, shown in Fig. 4.45, gives 18.9 events with 10 background events under the $\pm 3\sigma$ peak region with the mean located at 6287.0$\pm$4.8 (stat.) GeV/c^2. The resolution for the fit is fixed at 15.5 MeV/c^2 as given by Monte Carlo. During the scan on the data however, the width of the signal Gaussian was allowed to vary linearly with the mass, according to the location of the fit on the spectrum.

4.7.2 Studies Done After the Analysis

A number of studies were done after the analysis of the blind region. They have to do with the verification whether the signal events are genuine B_c decays, and the properties of the selected events.

With the identification of a peak location it becomes possible to define a lower and an upper side band of background population with respect to the found signal. A study was done [51] to investigate if the lower side band presents the characteristics

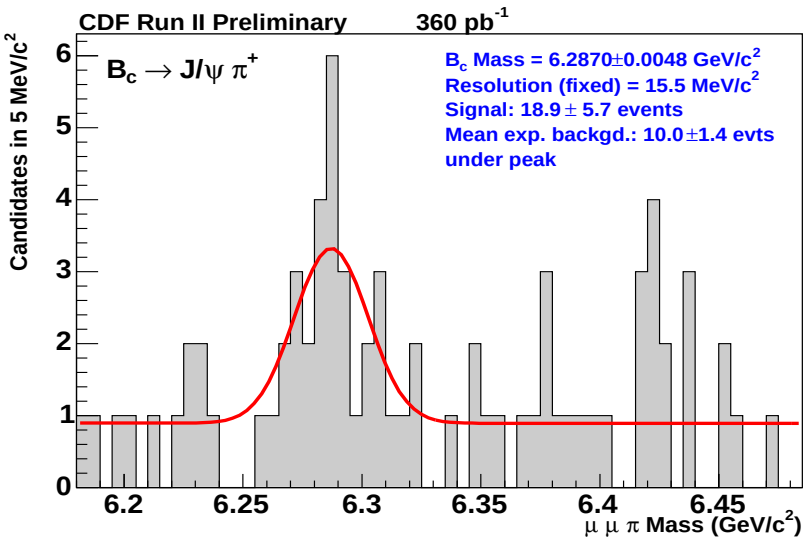

Figure 4.45: Invariant mass distribution of the candidates and results of the unbinned likelihood fit in the fit region indicated by the presence test scan.

of partially reconstructed B_c decays that would populate the mass region under the fully reconstructed decay. The study concluded that the events in the narrow peak are genuine B_c events.

It was however determined that after the analysis cuts, 81 of the remaining 390 candidates in the [5.6,7.2] GeV/c^2 region were featuring third tracks (the π) reconstructed from the SVX detector only. It was found that this accounts for 5 of the 28.9 events under the narrow peak, besides the 10 background events determined from the fit. Because these tracks use silicon only information, some of them can miss the COT and this results in a poor momentum resolution [53]. Consequently, the mass resolution they provide can reach 100 MeV/c^2 or above, an order of magnitude more than the expected B_c signal mass width. These tracks can only contribute to the peak as fluctuation and are therefore an additional source of background. The CDF collaboration decided that the proper action was the removal of these tracks based on resolution considerations, a concern that was not raised during the blind analysis procedure.

During theses investigations, it was also found that although a requirement on the precision of the vertex fit is made by the analysis cut 3-D χ^2 <9, and that the cut $\chi^2(\pi) < 2.6$ aims at insuring a π originated from the secondary vertex, some classes of tracks used as part of the data do not guarantee the possibility of random combination of a random π with the J/ψ. This is due to the fact that these classes do not include a silicon z information, and the constraint on χ^2 is applied on $R\phi$ only [52], ignoring a z information. Genuine signals are verified on the $B^{\pm}$ sample to come at 90% from tracks with SVX z hits information. Not having this requirement allows some tracks to pass the χ^2 cut without however being associated with the vertex and these classes of tracks without z information contribute mainly to background. An improved track selection consists on removing silicon only tracks and selecting those with silicon z information, leaving 220 candidates in the search region.

4.7.3 Improved Mass Measurement of the B_c Meson and Significance of the Signal

The criterion for the detection of the signal, set at Σ =3.5 derived from the ratio 1 out of 1000 [50], does not correspond to the significance. Detailed studies were performed [52], [53] for the determination of the significance of the signal. The method also uses a model of the background in the [5.6,7.2] GeV/c^2 region and testing a null hypothesis of the signal presence. As opposed to the Monte Carlo model constructed before the analysis of the data, the background shape is now known and can be decribed more precisely.

Independently of which classes of tracks are kept for the data sample, a narrow peak is still present and the found mass for the B_c never varies more than the initially quoted mass within its uncertainty. However, the significance of the signal is a function of the track selection chosen as data sample. With requirements made such that the silicon only tracks are removed, and only the tracks with silicon z information

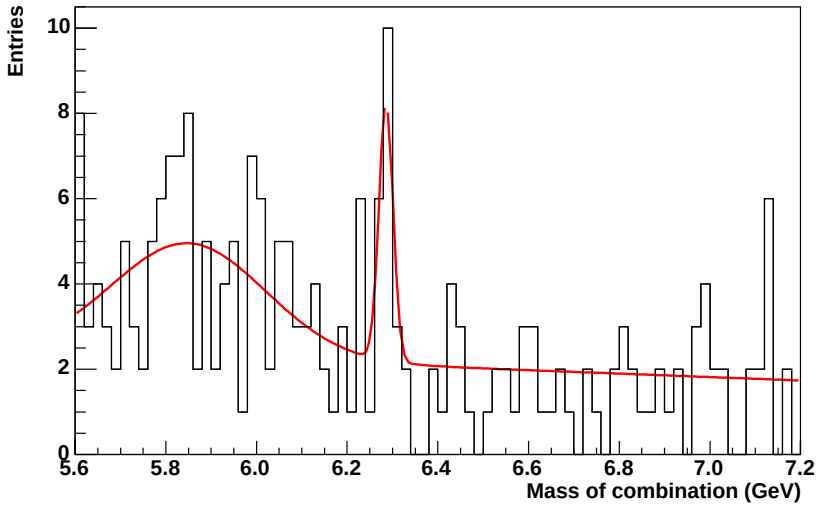

Figure 4.46: Fit on the data inside the [5.6,7.2] GeV/c^2 region with the improved track selection.

are selected for the data sample, a fit on the data is made for an improved measurement (Fig. 4.46). A narrow peak is found with 14.6 events on 4.6 of background at a location such that:

$$M(B_c) = 6285.7 \pm 5.3\ (stat.) \pm 1.2\ (syst.)\ MeV/c^2$$

The systematic errors (1.2 MeV/c^2) are due for 0.6 MeV/c^2 to the tracking systematic error, for 0.3 MeV/c^2 to the different mass of the third track, for 0.5 MeV/c^2 to the uncertainty of the $p_T(B_c)$, for 0.9 MeV/c^2 to the parametrisation of the background in the mass fit.

Using the known background distribution in the [5.6,7.2] GeV/c^2 region, a scan to search for a narrow peak on the data is made with a Gaussian and Poisson metric function.

This scan sets a maximum for the value of the chosen metric function corresponding to the peak in the data. The significance of this peak is now defined as the number of times this value is exceeded when the scan is performed on a pure background Monte Carlo modeled with accuracy, with 100 000 simulations. It was found

that for the improved track selection, the significance of the signal ranged between 0.012% and 0.02% (Fig. 4.47), depending on which metric function is used (Gaussian and Poisson, respectively) [53].

This represents the first clear identification of an exclusive decay channel of the B_c meson, giving the first precise measurement of the meson's mass [54].

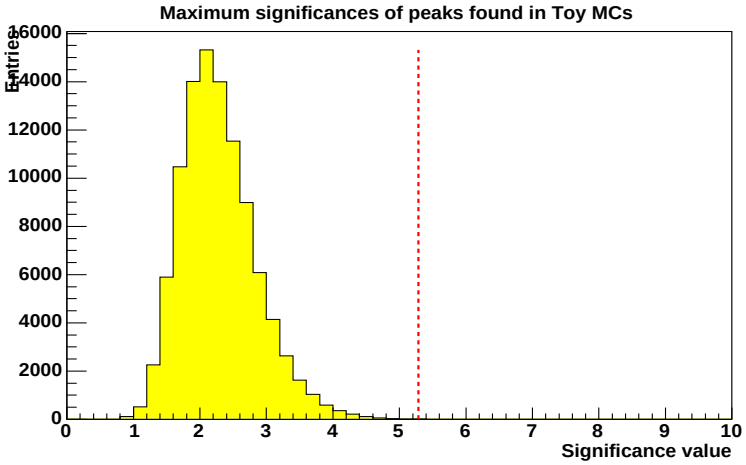

Figure 4.47: Significance test of Monte Carlo for background only, with the improved tracks requirements.

Chapter 5

Conclusions

The construction of a MARS model of the CDF colliding experiment has been presented with results of radiation production simulation for various problems.

The model helped to design the A48 collimator and to evaluate the impact of its installation in the Tevatron accelerator lattice. It was found that in this optimal shape protection, the collimator could give a reduction of the dose by a factor up to 25 for near beam sub-detectors at the level of CDF detector. The model quantified the impact on the Roman Pots detectors and helped to retain a final collimator configuration. This one, although not predicted to lead to damage in the Roman Pots, will unfortunately increase the radiation background by a factor 4. The MARS model also concluded to the exceeding of the quench stability limit of a Tevatron dipole in the event of a single abort kicker prefire.

Finally, the CDF MARS model was used to help the understanding of the radiation environment in CDF with the simulations of three machine related background channels, and the radiation originated from the beams collisions at the interaction point. It was found that the collisions are the dominant source of the radiation field in CDF, and the model will be used to continue the investigations of background due to beam loss.

Accelerator studies were conducted at the Tevatron to analyse the characteristics of the beam transverse profile. The method made the use of Tevatron collimators to reconstruct the profile of the beam. An experiment was planned to aim at the measurement of the beam diffusion speed due to residual gas present in the Tevatron beam pipe. A program was written to interpret the data and concluded to a 150 GeV/c proton only beam transverse growth of $(5.96\pm0.01)\times10^{-3}$ mm/h.

A subsequent study was performed with the aim of beam halo measurement at the Tevatron. Several possible experimental ways to achieve this goal were considered throughout the thesis duration, and the collimator scan method was chosen for time and practical considerations as a beam diagnostic easily and directly available. The potential of beam halo study with the collimator scan was investigated and it was found with a proton only experiment, that the beam transverse profile reconstruction at 150 GeV/c is possible up to 5 σ, where σ is the size assuming a Gaussian shape for the beam core. It is found however that the Gaussian description fails above 2 σ.

As a physics analysis project, the author took part in a search for a $B_c \to J\psi\pi$ decay signal using 360 pb^{-1} of CDF Run II data at $\sqrt{s}$ =1.96 TeV. Using Monte Carlo informations, data sample and a reference decay, a cut optimisation was performed using a blind technique within the relevant mass region, and the search concluded in the detection of a signal. At a later stage, some issues were raised concerning the tracks selection as part of the data sample for the analysis. After further selections, a narrow peak is still found allowing the measurement of the B_c meson:

$$M(B_c) = 6285.7 \pm 5.3\ (stat.) \pm 1.2\ (syst.)\ MeV/c^2,$$

with the significance of the signal being a function of the tracks selection. An improved measurement estimates the probability of a background fluctuation between 0.012% and 0.02% over the mass range 5.8-7.0 GeV/c^2. This represents the first detection of an exclusive decay channel of the B_c meson, allowing the precise measurement of its mass.

Bibliography

[1] N.V. Mokhov, "The MARS Code System User's Guide", Fermilab-FN-628 (1995); N.V. Mokhov, O. E. Krivosheev, "MARS Code Status", Proc. Monte Carlo 2000 Conf., p. 943, Lisbon, October 23-26, 2000; Fermilab-Conf-00/181 (2000);
N.V. Mokhov,"Status of MARS Code", Fermilab-Conf-03/053 (2003); http://www-ap.fnal.gov/MARS/.

[2] http://www-ap.fnal.gov/MARS/applications.htm

[3] I.S. Baishev, A.I. Drozhdin, N.V. Mokhov, "STRUCT Program User's Reference Manual", SSCL–MAN–0034 (1994), http://www-ap.fnal.gov/∼drozhdin/

[4] http://www-ap.fnal.gov/MARS/intro_manual.htm

[5] J. Briesmeister, "MCNP - a general Monte Carlo n-particle Transport Code", Technical Report LA-12625-M, LANL, 1993.

[6] M. A. Kostin, O .E. Krivosheev, N .V. Mokhov, I .S. Tropin, " An Improved MAD-MARS Beam Line Builder: User'S Guide", Fermilab-FN-0738 (2003)

[7] H. Grote, F. C. Iselin, "The MAD program (Methodical Accelerator Design)", CERN/SL/90-13 (1990).

[8] R. J. Tesarek, http://ncdf67.fnal.gov/∼tesarek/halo/BTeV bkgnds.pdf

[9] A. I. Drozhdin, V. A. Lebedev, N. V. Mokhov, S. I. Striganov, A. V. Tollestrup, L. Y. Nicolas, D. V. Sidorov, "Beam Loss and Backgrounds in the CDF and DØ Detectors due to Nuclear Elastic Beam-Gas Scattering", Fermilab-FN-734(2003), also FERMILAB-CONF-03-088, Particle Accelerator Conference (PAC 03), Portland, Oregon, 12-16 May 2003..

[10] M.D. Church, A.I. Drozhdin, A. Legan, N.V. Mokhov, R.E. Reilly, "Tevatron Run-II Beam Collimation System", *Proc. 1999 Particle Accelerator Conf.*, pp. 56-58, New York, March 29 - April 2, 1999; also Fermilab-Conf-99/059 (1999).

[11] A.I. Drozhdin, M. Church, R. Moore, D. Still, "Tevatron Abort Kicker Prefire Simulations", Beams-doc-648-v1, June 2003.

[12] http://rock23.rockefeller.edu/ michgall/fd/forward_detectors.html

[13] http://www-ap.fnal.gov/∼martens/fpd/photos/

[14] A. I. Drozhdin, N. V. Mokhov, D. A. Still, R. V. Samulyak, "Beam-Induced Damage to The Tevatron Collimators: Analysis and Dynamic Modeling of Beam Loss, Energy Deposition and Ablation", Fermilab-FN-0751, June 2004.

[15] http://ncdf67.fnal.gov/∼tesarek/halo/Ace_BeamMonitoring.pdf

[16] http://ncdf67.fnal.gov/∼tesarek/radiation

[17] R. J.Tesarek, S. D'Auria, A. Hocker, K. Kordas, S. McGimpsey, S. Worm, "A Measurement of the radiation environment in the CDF tracking volume", Nuclear Instruments and Methods in Physics Research A 514 (2003) 188-193.

[18] N. V. Mokhov, L. Y. Nicolas, "Impact of the A48 Collimator on the Tevatron BØ Dipoles", FERMILAB-TM-2214.

[19] J. Ranft, 'Dual Parton Model at Cosmic Ray Energies', *Phys. Rev.* **D51**, 64–85 (1995); Gran Sasso Report INFN/AE-97/45 (1997); S. Roesler, R. Engel,

J. Ranft, 'The Monte Carlo Event Generator DPMJET-III', *Proc. Monte Carlo 2000 Conf.*, p. 1033, Lisbon, October 23-26, 2000; S. Roesler, R. Engel, J. Ranft, 'The Event Generator DPMJET-III at Cosmic Ray Energies', *Proc. ICRC-2011 Conference*, 439, Copernicus Gesellschaft (2001).

[20] M. Jones. Private Communication.

[21] R. J.Tesarek, S. D'Auria, A. Hocker, K. Kordas, S. McGimpsey, L. Nicolas, S. Worm, "A Measurement of the radiation environment in the CDF tracking volume", *NIM to be submitted.*

[22] V. Shiltsev, Fermilab-Beams-doc-258-v1, june 2002.

[23] N. V. Mokhov, V. I. Babelkov, "Beam and Luminosity Lifetime", Handbook of Accelerator Physics and Engineering, Ed. by A.W.Chao and M.Tigner, p.218, World Scientific (2002).

[24] A. Jansson et al, "Collimator Scans to Measure Tevatron Emittance", Fermilab-Beams-doc-393-v2 (2003).

[25] D. A. Edwards, M. J. Syphers, An Introduction to the Physics of High Energy Accelerators, Wiley, N.Y.(1993).

[26] M. J. Syphers, "Beam-Gas Scattering Lifetimes in the Fermilab Main Ring", Fermilab-FN-484 (1988).

[27] V. A. Lebedev, S. Nagaitsev, "Particle Diffusion due to Coulomb Scattering", Fermilab-CONF-02/099-T(2002).

[28] K. Potter, "Beam Profiles", CERN Accelerator School, (1983).

[29] M. Syphers, Accelerator Discussion Group Lectures, Fermilab-beams-doc-763-v1.

[30] CDF Collaboration, Phys. Rev. D58 112004 (1998).

[31] [22] W. K. Kwong, J. L. Rosner, Phys. Rev. D44, 212 (1991); [23] E. J. Eichten, C. Quigg, Phys. Rev. D49 5845 (1994); [17] H. P. Shannahan et al., Phys. Lett. B453, 289 (1999); [24] N. Brambilla, A. Vairo, Phys. Rev. D 62 094019 (2000); [25] N. Brambilla et al., Phys. Lett. B513, 381 (2001); [26] N. Brambilla et al., Phys. Rev. D65, 034001 (2002); (6) Di Pierro et al., Nucl. Phys. Proc. Supp. 142, 340 (2004); (7) I. F. Allision et al., Nucl. Phys. Proc. Supp. 140, 440 (2005).

[32] A. V. Berezhnoy, "Color flows for the process $gg \longrightarrow B_c + c + \bar{b}$", hep-ph/0407315 v1.

[33] K. Anikeev et al., "B Physics at the Tevatron Run II and Beyond", hep-ph/0201071.

[34] V.A. Saleev, D.V. Vasin, "Production of B_c Mesons Via Fragmentation in the k_T- Factorization approach", Phys.Lett.B605:311-318, 2005.

[35] K. Anikeev, G. Bauer, C. Paus, "B meson lifetime measurements in Run-II data CDF/DOC/BOTTOM/CDFR/6266

[36] P. Bussey et al., "Search for a $B_c \to J/\psi\pi$ Signal: Cut Optimization and Final Procedures", CDF/ANAL/BOTTOM/GROUP/7282 (2005).

[37] Timothy K. Nelson, "The CDF Layer 00 Detector", FERMILAB-CONF-01/357-E.

[38] PDG, S. Eidelman et al., Physics Letters B592, 1 (2004).

[39] R. Blair et al, CDF-II Collaboration, "The CDF-II Detector: Technical Design Report", FERMILAB-PUB-96-390-E.

[40] A. Affolder et al., "Status Report of the Intermediate Silicon Layers Detector at CDFII", CDF/DOC/TRACKING/PUBLIC/5687 August 2001.

[41] M. Shapiro et al., "Update on primary vertex finding", BPAK meeting June 25 2004.

[42] P. Sphicas, "A $b\bar{b}$ Monte Carlo Generator", CDF/DOC/BOTTOM/CDFR/2655.

[43] K. Anikeev, C. Paus, P. Murat, "Description of Bgenerator II", CDF/DOC/BOTTOM/CDFR/5092.

[44] W. Bell, J. P. Fernandez, L. Flores, F. Wuerthwein, R. J. Tesarek, "User Guide For EvtGen @ CDF", CDF/DOC/BOTTOM/CDFR/5618.

[45] M. Bishai et al., "Measurement of the J/ψ Meson and b Hadron Production Cross Sections", CDF/PUB/BOTTOM/GROUP/7037.

[46] C-H. Chang, X-G. Wu, "Uncertainties in Estimating Hadronic Production of the Meson B_c and Comparisons Between Tevatron and LHC", hep-ph/0309121.

[47] A. V. Berezhnoy, Private communication; A. V. Berezhnoy, V. V. Kiselev, A. K. Likhoded, Z.Phys.A356, 79 (1996); A. V. Berezhnoy, A. K. Likhoded, M. V. Shevlyagin, Phys.Atom.Nucl.58, 672 (1995).

[48] T. Sjostrand et al., "Pythia 6.2 Physics and Manual", hep-ph/0108264.

[49] G. Punzi, "Sensitivity of Searches for New Signals and its Optimization", PHYSTAT2003 physics/0308063.

[50] W. A. Rolke, A. M. Lopez, "How to Claim A Discovery", PHYSTAT2003 physics/0312141.

[51] P. Bussey et al., "Characterization of the $B_c \rightarrow J/\psi\pi$ Candidates and Evidence for Partially Reconstructed Decays $B_c \rightarrow J/\psi + track + X$", CDF/ANAL/BOTTOM/CDFR/7434.

[52] B. Wicklund "Significance Study for $B_c \rightarrow J/\psi\pi$", CDF/DOC/BOTTOM/GROUP/7481.

[53] P. Bussey et al., "Evidence of $B_c^{\pm} \rightarrow J/\psi\pi^{\pm}$ Effects of Additional Track Type Selections and Global Fit to the Mass Spectrum", CDF/ANAL/BOTTOM/GROUP/7805.

[54] CDF Collaboration, "Evidence for the exclusive decay $B_c^{\pm} \rightarrow J/\psi\pi^{\pm}$ and measurement of the mass of the $B_c^{\pm}$ meson", hep-ex/0505076 *submitted to PRL.*